DESIGN AND IMPLEMENTATION OF A RECONFIGURABLE INTELLIGENT SURFACE

A THESIS SUBMITTED TO
THE GRADUATE SCHOOL OF NATURAL AND APPLIED SCIENCES
OF
MIDDLE EAST TECHNICAL UNIVERSITY

BY

MÜKREMIN BARIŞ ŞAHIN

IN PARTIAL FULFILLMENT OF THE REQUIREMENTS
FOR
THE DEGREE OF MASTER OF SCIENCE
IN
ELECTRICAL AND ELECTRONICS ENGINEERING

AUGUST 2024

Approval of the thesis:

DESIGN AND IMPLEMENTATION OF A RECONFIGURABLE INTELLIGENT SURFACE

submitted by **MÜKREMIN BARIŞ ŞAHIN** in partial fulfillment of the requirements for the degree of **Master of Science in Electrical and Electronics Engineering Department, Middle East Technical University** by,

Prof. Dr. Naci Emre Altun
Dean, Graduate School of **Natural and Applied Sciences**

Prof. Dr. İlkay Ulusoy
Head of Department, **Electrical and Electronics Engineering**

Prof. Dr. Özlem Aydın Çivi
Supervisor, **Electrical and Electronics Eng. Dept., METU**

Examining Committee Members:

Prof. Dr. Sencer Koç
Electrical and Electronics Eng. Dept., METU

Prof. Dr. Özlem Aydın Çivi
Electrical and Electronics Eng. Dept., METU

Prof. Dr. Gülbin Dural Ünver
Electrical and Electronics Eng. Dept., METU

Assist. Prof. Dr. Lale Alatan
Electrical and Electronics Eng. Dept., METU

Prof. Dr. Birsen Saka Tanatar
Electrical and Electronics Eng. Dept., Hacettepe University

Date: 27.08.2024

I hereby declare that all information in this document has been obtained and presented in accordance with academic rules and ethical conduct. I also declare that, as required by these rules and conduct, I have fully cited and referenced all material and results that are not original to this work.

Name, Surname: Mükremin Barış Şahin

Signature :

ABSTRACT

DESIGN AND IMPLEMENTATION OF A RECONFIGURABLE INTELLIGENT SURFACE

Şahin, Mükremin Barış
M.S., Department of Electrical and Electronics Engineering
Supervisor: Prof. Dr. Özlem Aydın Çivi

August 2024, 97 pages

The Reconfigurable Intelligent Surface (RIS) concept has gained increasing interest each year due to its potential benefits for 6G networks. The main advantages are the coverage area extension, suppression of unwanted signals, and improved channel rank condition. RIS is a planar surface consisting of several elements having highly precise phase distribution control to redirect the incident wave to required direction. In this thesis, a high-phase resolution unitcell and a RIS using this unitcell are designed. The proposed unitcell comprises a 3×3 patch-like structure with pin diodes between them. The design incorporates a high number of bits, which significantly enhances its phase resolution, allowing for fine adjustments in phase to accurately control the direction and characteristics of the reflected wave. With this unit cell, number of control bits can be reduced to even one to reduce complexity in the implementation and control while still maintaining acceptable performance. Following the design of the unitcell, a RIS is constructed. The capabilities and limitations of the RIS are discussed to highlight its strengths and address any potential challenges or drawbacks. Finally, to validate the design, a physical prototypes of the RIS are produced and measured. It is demonstrated that the designed RIS can steer the main beam to the desired direction.

Keywords: Reconfigurable Intelligent Surface, 6G, electromagnetic wave control, beam steering, programmable surface

ÖZ

YENİDEN AYARLANABİLİR AKILLI YÜZEYİN TASARIMI VE UYGULAMASI

Şahin, Mükremin Barış
Yüksek Lisans, Elektrik ve Elektronik Mühendisliği Bölümü
Tez Yöneticisi: Prof. Dr. Özlem Aydın Çivi

Ağustos 2024 , 97 sayfa

Yeniden Ayarlanabilir Akıllı Yüzey (YAAY) kavramına olan ilgi 6G ağları için potansiyel faydaları nedeniyle her yıl artmaktadır. Bu konseptin başlıca avantajları arasında kapsama alanının artırılması, istenmeyen sinyallerin bastırılması ve kanal sıralama koşulunun iyileştirmesi yer almaktadır. YAAY, gelen dalgayı istenen doğrultuya yönlendirmek için yüzey faz dağılımı üzerinde yüksek hassasiyetli kontrole sahip çeşitli elemanlardan oluşan düzlemsel bir yüzeydir. Bu tezde, yüksek faz çözünürlüğüne sahip bir birim hücre ve bu birim hücreyi kullanarak bir YAAY tasarlanmıştır. Tasarlanan birim hücre, aralarında pin diyotlar bulunan 3×3 yama benzeri bir yapıdan oluşmaktadır. Tasarım yüksek bit sayısı içermektedir, bu özellik faz çözünürlüğünü önemli ölçüde artırarak yüzey faz dağılımı hassas bir şekilde ayarlanabilmesini ve yansıtılan dalganın yönünü ve özelliklerini doğru bir şekilde kontrol edilebilmesini sağlamaktadır. Bu birim hücrede kontrol bitlerinin sayısı, kabul edilebilir bir performans sağlamaya devam ederek uygulama ve kontrol karmaşıklığını azaltmak için bir bite kadar düşürülebilir. Birim hücre tasarımının ardından, bu birim hücre ile bir YAAY tasarımı yapılmıştır. YAAY'ın yetenekleri, sınırları ve güçleri yönleri sunulmuş ardından olası zorlukları ve dezavantajları tartışılmıştır. Son olarak, tasarımı doğrulamak amacıyla fiziksel YAAY prototipleri üretilmiş ve ölçülmüştür. Tasarlanan YAAY'lerin ana hüzmeyi istenilen doğrultuya yönlendirdiği gösterilmiştir.

Anahtar Kelimeler: Yeniden ayarlanabilir akıllı yüzey, 6G, Elektromanyetik dalga kontorlü, hüzme yönlendirme, programlanabilir yüzey

ACKNOWLEDGMENTS

First and foremost, I would like to express my deepest gratitude to my advisor, Prof. Dr. Özlem Aydın Çivi, for her invaluable supervision, guidance, and patience throughout this journey. I extend my sincere thanks to ASELSAN Inc. and the METU Electrical and Electronics Engineering Department for their unwavering support during the simulations, fabrication, and measurements of the products.

I am profoundly grateful to my parents, Kadircan and Cemaliye Şahin, for their endless sacrifices in raising me to be a happy and forward-thinking individual. Everything I have achieved is because of them. I also wish to thank my sister, Sevgi Didem Şahin, for always being there as a caring and supportive sibling.

Lastly, I am deeply thankful to my girlfriend, Aysu Koç, for her emotional support and unwavering love, which has been a constant source of strength throughout this process.

TABLE OF CONTENTS

CHAPTERS

LIST OF TABLES

TABLES

LIST OF FIGURES

FIGURES

LIST OF ABBREVIATIONS

RIS	Reconfigurable Intelligent Surfaces
LoS	Line of Sight
PEC	Perfect Electric Conductor
SLL	Side Lobe Level
RCS	Radar Cross Section

CHAPTER 1

INTRODUCTION

Reconfigurable Intelligent Surfaces (RIS) constitute a groundbreaking advancement in wireless communication technology that could transform how electromagnetic waves are controlled within a communication environment. In traditional communication systems the propagation medium is considered as a random entity between the transmitter and receiver, due to the unpredictable interactions between broadcast radio waves and surrounding objects,which degrades the quality of the received signal [1]. RIS has the potential to change this random aspect of the medium by manipulating the reflected wave. By adjusting the propagation direction, some advantages can be gained, such as improving the signal quality, increasing the coverage area, and improving the channel statistics. Relaying is another technology that has similar advantages. Yet, typical relays receive signals and re-transmit the received signal; therefore, they require complex signal processing and consume more energy. However, unlike typical relays, RIS elements are passive and rely on their physical configuration to modify wave properties. This passive nature allows RIS to operate with minimal energy consumption, leading to more sustainable and cost-effective network deployments [2].The conceptual breakthrough of RIS lies in its ability to provide such precise control over the propagation environment, transforming previously passive infrastructures like building facades or indoor walls into active components of a communication network [1]. As such, RIS technology aligns closely with the emerging demands of next-generation wireless networks, which require highly flexible and efficient solutions to manage the increasing complexity and density of wireless systems [2].

Reconfigurable Intelligent Surfaces (RIS) have a crucial role in the development and deployment of 6G networks. As 6G technology aims to deliver on promises of higher data rates, near-zero latency, and extensive connectivity for emerging applications [3]. RIS can intelligently manage and optimize wireless propagation environments, significantly enhancing signal coverage, reliability, and network efficiency in complex and densely populated settings [4]. Moreover, the passive nature of RIS aligns with the 6G vision for sustainability, as it promotes energy efficiency by reducing the need for power-intensive hardware [3].

Reconfigurable Intelligent Surfaces (RIS) introduce several applications that significantly improve the efficiency, reliability, and performance of wireless networks. One key application is coverage extension, RIS can extend network coverage by acting as a smart reflector that redirects and focuses signals towards intended areas or users, effectively bypassing physical obstructions such as buildings and natural terrain features for outdoor communication, or walls and columns for indoor communication. By doing so, RIS panels can establish visual line-of-sight (LoS) conditions between transmitters and receivers that would otherwise be blocked [2]. In Figure 1.1a an illustration of coverage extension is shown. The figure depicts a blockage between the transmitter and receiver, which RIS overcomes by creating a virtual LoS between them. Another importing application is interference suppression, a critical issue in densely populated network environments where multiple devices often operate on overlapping frequencies [2],[5]. In Figure 1.1b an illustration of suppression is shown. By strategically manipulating the signal phase across its elements, RIS can generate patterns of constructive and destructive interference to enhance desired signals while suppressing unwanted interference.

1.1 Evolution of Concept

The concept of Reconfigurable Intelligent Surfaces (RIS) has evolved in parallel with advances in technologies designed to enhance electromagnetic wave manipulation, aiming to improve communication systems.

- **Fixed Beam Reflectarrays:** Reflector and array antennas both have distinct advantages, and a reflectarray antenna combines the best qualities of each. As

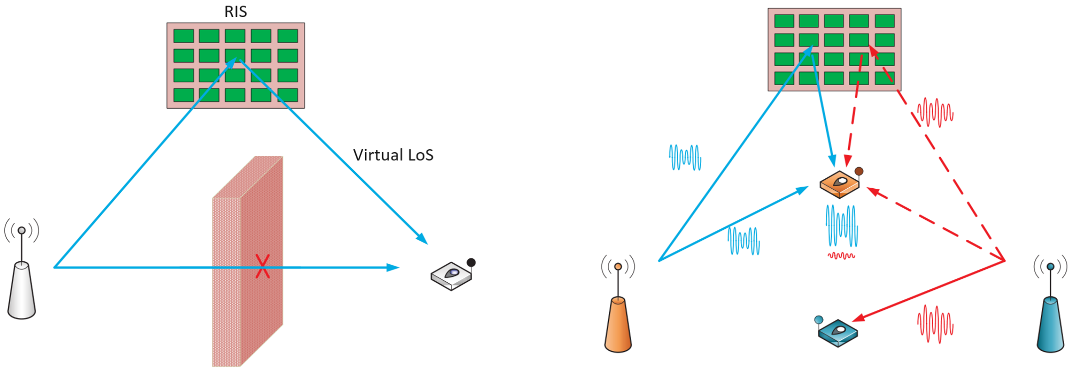

(a) Coverage extension by creating virtual LoS [2]

(b) Interference suppression of unwanted signal [2]

Figure 1.1: Two application examples of RIS

shown in Figure 1.2a, the array is illuminated by a feed antenna. Each element of the array is engineered to scatter the incident field with the specific phase required to create a phase distribution across the aperture. A reflectarray antenna and a parabolic antenna are shown In Figure 1.2b. Similarly, for parabolic antennas, the phase distribution at the reflecting surface determines the properties of the reflected wave. An imaginary line at the end of the parabolic reflector is drawn, and the phase distribution of the reflectarray can be compared to the phase distribution at this surface. If they are similar, then the pattern of reflectarray would be similar to the parabolic antenna's. Thus, a reflectarray is sometimes referred to as a flat reflector [6]. However, unlike parabolic antennas, reflectarrays can have a squinted pattern and are very lightweight. Fixed beam reflectarrays particularly valuable in applications where high gain and compactness is crucial, such as satellite communications and radar systems [7].

- **Reconfigurable Reflectarrays:** Reconfigurable reflectarrays represent a significant advancement over traditional fixed reflectarrays by incorporating elements that can dynamically change their reflective properties. This adaptability permits real-time adjustment of the direction and focus of the reflected waves. Achieving this adaptability involves the integration of electronically controllable components, such as varactor diodes or micro-electromechanical systems (MEMS) switches, embedded within each antenna element [8]. In Figure 1.3,

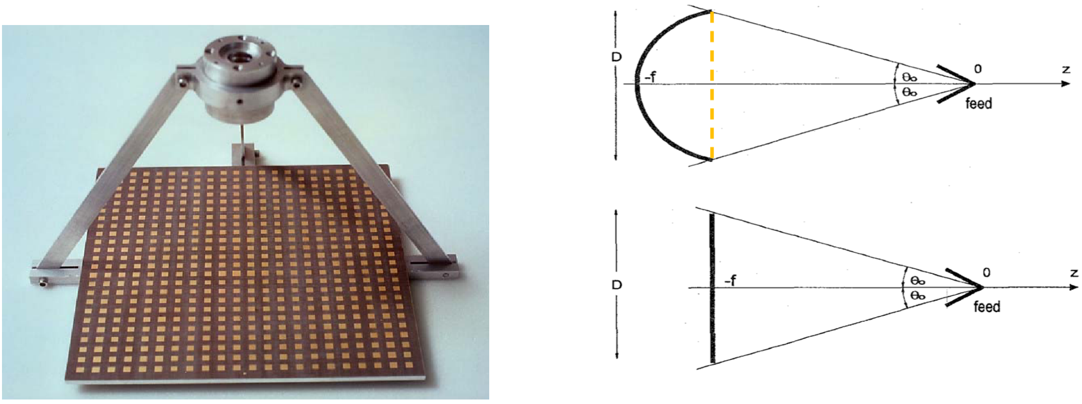

(a) Microstrip patch reflectarray [6].

(b) Feed and reflecting surface of the reflectarray and reflector antenna [6].

Figure 1.2: Fixed beam reflectarray

an example of reconfigurable reflectarrays is shown. The length of the stubs of the microstrip patches can be altered by changing the states of the diodes, thus enabling phase adjustment of each element.

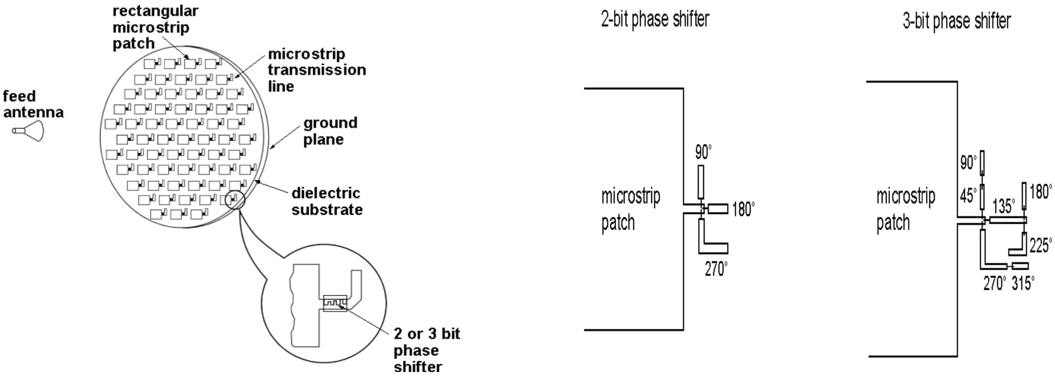

(a) Reconfigurable reflectarray using phase shifters [8].

(b) Reconfigurable element with PIN diodes attached to different length stubs[8].

Figure 1.3: Reconfigurable reflectarray

- **Fixed Intelligent Surfaces :** Fixed intelligent surfaces are closely related to fixed beam reflectarray antennas in their ability to manipulate electromagnetic waves. However, a key distinction lies in their interaction with the wave source: whereas reflectarrays typically operate with a feed in the near field, intelligent surfaces are designed to handle waves originating from the far field. Similar to reflectarrays, these surfaces are made from subwavelength-scaled structures that precisely modify the phase and amplitude of incoming waves. This manipulation makes intelligent surfaces particularly useful in improving the coverage area for both indoor and outdoor applications.

- **RIS:** The principle of both fixed intelligent surfaces and Reconfigurable Intelligent Surfaces (RIS) is to manipulate incoming electromagnetic waves. However, the critical distinction between them lies in the dynamic capabilities of RIS. Unlike fixed intelligent surfaces, which have static characteristics once fabricated, the elements of an RIS can be dynamically adjusted. This capability enables RIS to actively manipulate wavefronts in real-time, adapting to changes in the environment or requirements of the communication system. The flexibility and precision of RIS are particularly beneficial in complex urban environments or densely populated areas where they can mitigate interference, enhance signal quality, and improve the efficiency of wireless networks [2]. In Figure 1.4, an example of RIS usage is shown. In the example the main beam of the reflected wave is altered between user 1 and 2 using RIS.

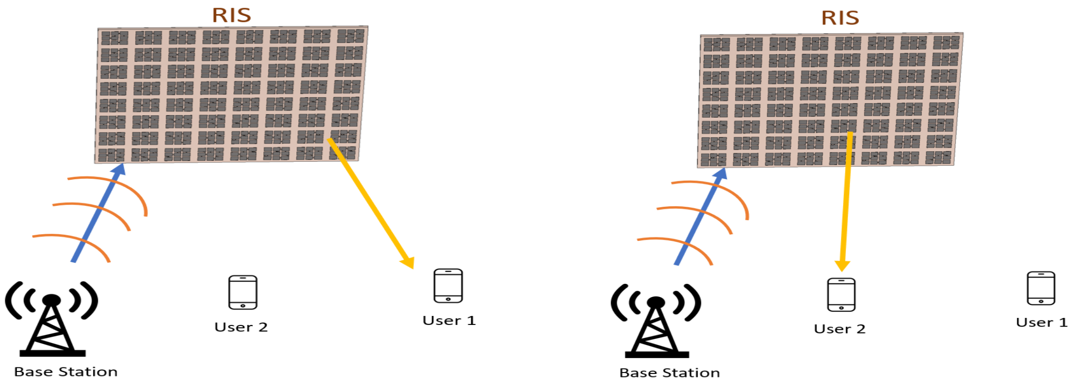

Figure 1.4: An example for an application of RIS

1.1.1 Reconfigurability Techniques

The electrical tuning of Reconfigurable Intelligent Surfaces (RIS) can be achieved through various methods.

a. Lumped Elements

The most commonly used reconfiguration elements in reconfigurable antennas are definitely lumped components. These components are positioned within the unit cell to change its electrical properties. Lumped components primarily fall into two categories: RF switches and variable capacitors. RF switches are advantageous due to their simple control circuits, though they are limited to a discrete number of states. On the other hand, variable capacitors offer continuous tunability, although this requires more complex control circuitry [9].

- **PIN diodes:** Semiconductor technology is currently the most widely utilized method for implementing switches. An RF switch can be created using a PIN diode, which operates by alternating between forward and reverse biasing. PIN diodes are widely used, especially at lower frequencies (below 10 GHz), because of their superior isolation and insertion losses, low cost, and robustness. However, their minimal power consumption, measured in milliwatts, can be a limitation in designs that require a high number of switches [9].
- **RF MEMS Switches:** Another technology for reconfigurability is RF MEMS switches. These switches consume very low power (nearly zero) and offer very high linearity and low insertion loss [10]. However, the main issue with RF MEMS switches is their high production costs. Due to these costs, they are typically used in very large-scale structures where their low power consumption can offset the disadvantage of high expenses [9].
- **Varactor Diode:** Varactor diodes provide excellent continuous tunability and low power consumption. However, they come with some disadvantages. The capacitance-voltage relationship of varactor diodes is non-linear, which can introduce distortion in high-frequency applications. Additionally, they have a limited voltage range for operation, beyond which the diode can be damaged, restricting their use in high-voltage scenarios. Moreover, their performance can vary with temperature changes, potentially necessitating additional circuitry to maintain stability in precision applications [10].

b. Tunable Materials

Materials with tunable electromagnetic properties can also provide reconfiguration features. These materials offer notable advantages such as continuous reconfigurability, which can be achieved with a simple control system. However, compared to other technologies, these materials often exhibit lower reconfiguration capabilities and tend to be more lossy [9].

- **Ferrites:** The permeability of ferrite materials, can be dynamically changed by applying an external magnetic field. This characteristic makes them highly useful for reconfigurable structures in various applications such as antennas [11], [12].
- **Graphene:** Graphene attracts significant attention because of its tunability at optical frequencies. The surface conductivity of monolayer graphene can be tuned by changing its chemical potential. Graphene can be used in the design of RIS, polarization converters, tunable antennas, etc. [13], [14].
- **Liquid Crystals:** The molecule orientation in a liquid crystal can be changed by an applied static electric field. Since its electric permittivity tensor can be adjusted, liquid crystals can serve as an effective substrate for reconfigurable surfaces [15].
- **Optically Tuned Semiconductor Materials:** This type of semiconductor changes its electrical properties when illuminated and when not. The main advantage of this reconfigurability is that it does not require control circuitry on the substrate [16].

1.2 Design Principles of RIS

Designing a Reconfigurable Intelligent Surface (RIS) involves several critical steps, each aimed at ensuring the RIS meets specific performance criteria and is suited for its intended applications. First, the design criteria, such as the operational frequency, limits of the beamforming capabilities, and power handling, should be established. After determining these criteria, the next step is to design a unit cell. Subsequently, the reconfigurability technique must be chosen, followed by the design of the surface itself and comprehensive simulations.

1.2.1 Unit Cell Design

A unit cell of a Reconfigurable Intelligent Surface (RIS) is the smallest, repetitive component. It typically comprises conductive elements such as metallic patches or dipoles. Each unit cell can individually change the phase or amplitude of the incoming electromagnetic wave.

To understand the behavior of unit cells in a RIS, Floquet analysis should be used. In Floquet analysis, the unit cell is treated as if it is part of an infinitely periodic structure [17]. In Figure 1.5a, an example of Floquet analysis of a unit cell is shown. The cell consists of a metallic patch on top and a dielectric substrate beneath it, where periodic boundaries enable the simulation of the cell as if it were part of an infinitely periodic structure. By applying Floquet analysis to unit cells, we can obtain information on phase and amplitude responses [17]. The phase response of a unit cell indicates how it modifies the phase of an incident electromagnetic wave, representing the phase difference between the incoming and reflected wave. In the analysis vertical polarized normal incident field is used as the incoming wave. The amplitude response indicates the percentage of the incoming wave that is reflected. In Figure 1.5b, the phase diagram of the unit cell is shown. The simulation was conducted at 10 GHz. The x-axis representing the width of the metallic patch and the y-axis representing the phase of the reflected field from the cell. As the width values vary, the difference in phase between the reflected wave and the incoming wave changes.

1.2.2 Surface Design

Following the design of the unit cell and the selection of the reconfigurability method, the next step is to determine the size of the RIS. The size of the RIS plays a pivotal role in its ability to manipulate the reflected wave; however, increasing the size also introduces additional complexity. Once the size has been established, the RIS will be constructed using the previously designed unit cell. The states of the unit cells will define the phase distribution across the surface, thereby adjusting the characteristics of the reflected wave. To validate its performance characteristics, such as beamforming capabilities, full-wave electromagnetic simulations will be conducted.

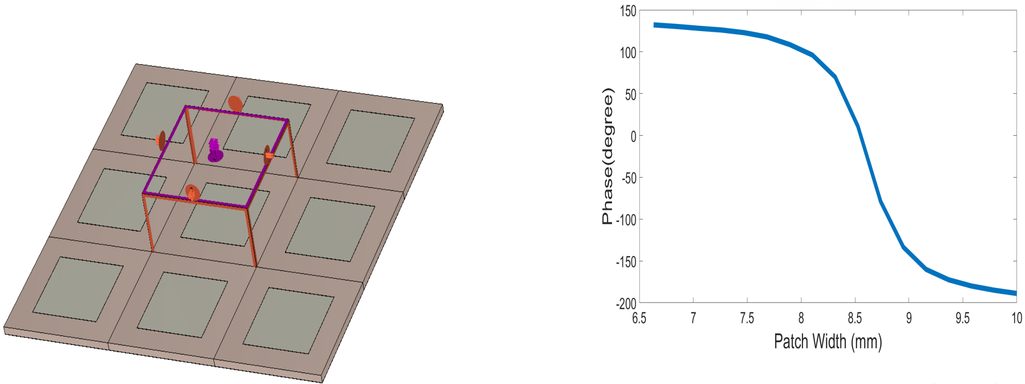

(a) Floquet simulations of a unit cell

(b) The phase diagram result of the floquet simulations

Figure 1.5: An illustration of the floquet simulation setup and its phase diagram result.

The phase distribution of a surface, dictates the properties of the outgoing wave. Figure 1.6 shows an example of a surface's phase distribution. The colors represent the phase at specific locations. This particular distribution is designed to steer the reflected beam to a 30-degree angle. To precisely manipulate the wave, the phase distribution of the surface must be adjusted accordingly.

Two main factors affect the phase distribution of the surface: spatial delay and the phase response of the elements. Spatial delay is the phase difference observed at various locations on a surface, which arises due to the angle at which an incoming wave strikes the surface. Figure 1.7, illustrates the concept of spatial delay. Since the distances between various locations on the surface and the feed vary, the phase of the incoming wave differs at different locations. The illustration is for a reflectarray antennas but the concept is the same for RIS. When the incoming wave is not normal incidence the phase of the incoming wave will differ at various locations on the surface. As discussed in Chapter 1.2.1 the phase response of an element describes how the phase of the reflected wave changes in relation to the phase of the incoming wave. These two factors, spatial delay and phase response, combine to form the phase distribution of the surface. Since the spatial delay is fixed and cannot be changed, the phase response of each element must be adjusted to manipulate the reflected wave effectively. Chapter 3 provides a detailed explanation on how the phase distribution should be adjusted by changing the phase response of elements.

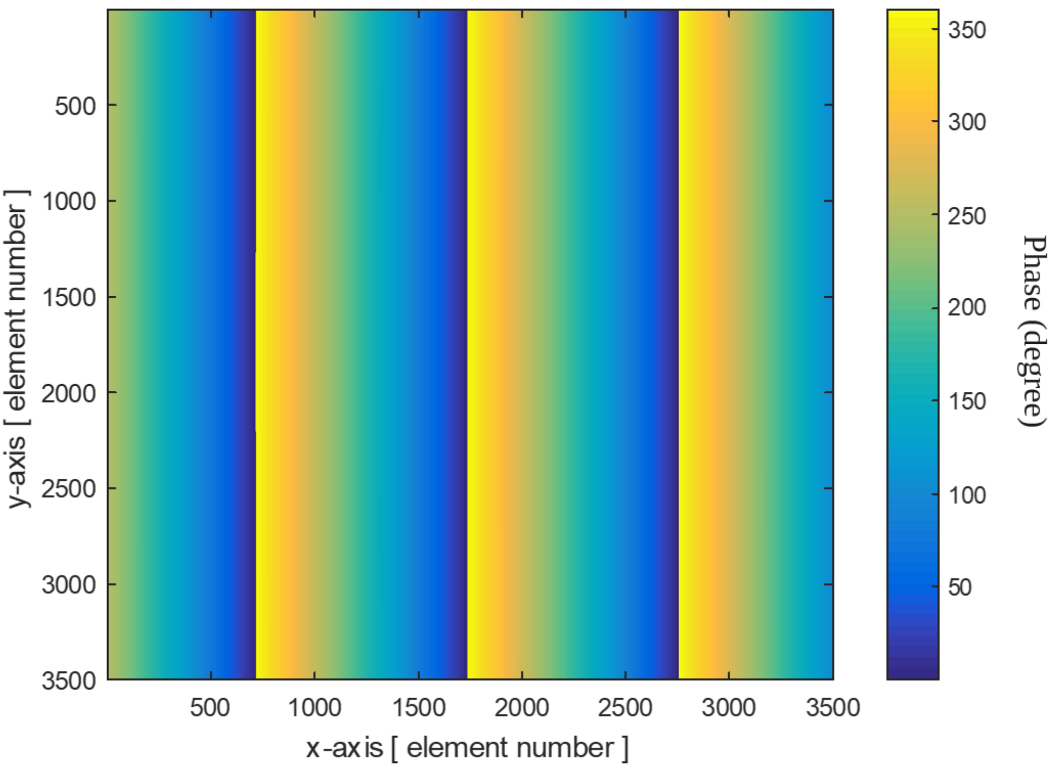

Figure 1.6: Phase Distribution Example

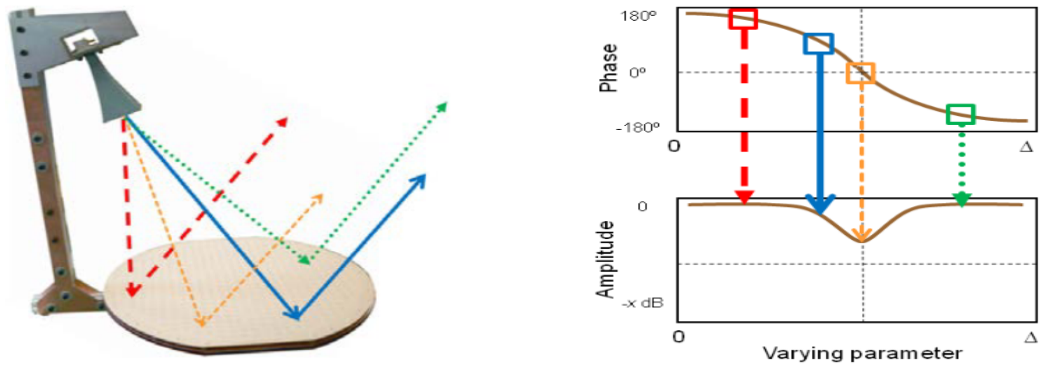

(a) Illustration of the spatial delay

(b) Effect on the phase and the amplitude of the spatial delay

Figure 1.7: Spatial delay

1.3 Literature Review

First, the idea of RIS started to be discussed in the research on its possible usage areas and advantages for the 6G communication networks [1], [2]. These studies highlight that traditional concepts are insufficient for 6G communication. While having a MIMO antenna system enhances communication capabilities, it is still inadequate. To further enhance these capabilities, the propagation environment must also be designed. One reason for this insufficiency is the need to increase the frequency to achieve higher data rates but at higher frequencies, the propagation loss would be significant [18]. RIS can help with this issue. Traditional environments reflect waves randomly; however, RIS can focus the reflected beam and increase signal quality for the user. The other problem with using high frequencies is that as the wavelength decreases, obstacles block the waves more than at lower frequencies. RIS can overcome this issue by changing the direction of the reflected beam, thereby increasing the coverage area. It is also mentioned that if the dimension of a RIS is large with respect to its wavelength, users would be in its near field. This effect could be used to increase network capabilities because, unlike far-field propagation, near-field propagation allows for more than one communication mode [19].

After the theoretical research progress reached a level, researchers started to build prototypes for different RIS structures. Although it is a relatively new subject, there are many well-designed RIS examples in the literature. For instance, in [20], a RIS was designed at 3.5 GHz. They implement varactor diodes on each unit cell to adjust the phase distribution of the surface. These diodes continuously change the phase response of the unit cell, providing precise control over the surface phase distribution. The surface is shown in Figure 1.8. The dimensions of the surface are $14\lambda \times 14\lambda$. The manufactured RIS was tested for beam steering applications, it successfully steers the beam to 15, 30, and 45 degrees. They also tested the performance of the RIS in a non-LoS scenario. The measurement setup for the non-LoS scenario is shown in Figure 1.8. In this example, there was no direct connection between the user and the transmitter, but by using a RIS, the transmitted signal was enhanced by up to 15 dB.

Another example of a RIS is provided in [21]. They designed a RIS that operates at 28 GHz and has a 1 GHz bandwidth (2.8%). A 2-bit unit cell was used, and the floquet

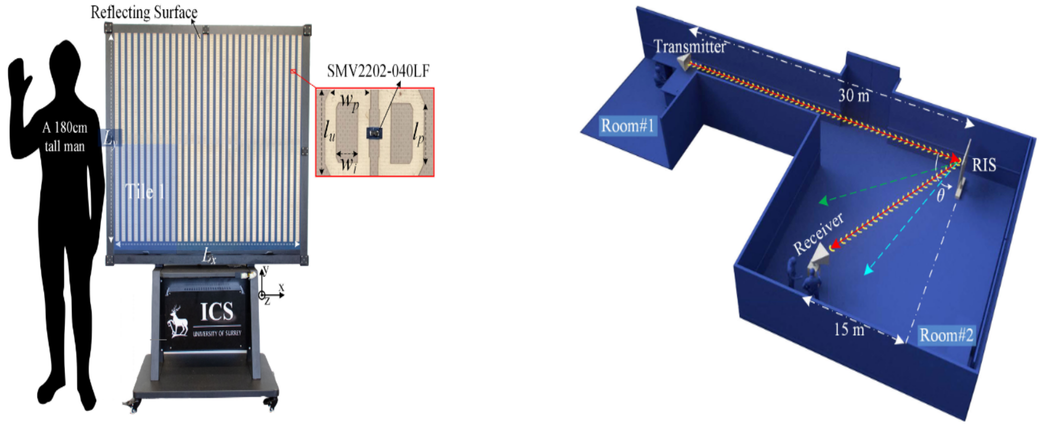

(a) The manufactured RIS example and its unit cell

(b) The measurement setup of the RIS for non LoS scenarios

Figure 1.8: RIS design example [20]

port simulations of the unit cell were verified through waveguide measurements. For this measurement, a single unit cell was placed in a waveguide, and the results were compared with the simulations. After verification, the surface was manufactured, and a setup similar to [20] was built to test its non-LoS performance. It was shown that, in the non-LoS scenario, the RIS could increase the signal power up to 25 dB. However, no further information was provided about the performance of the RIS, such as its beam-steering capabilities. An additional example of a RIS can be found in [22]. They designed a RIS at 28 GHz with a bandwidth of 27%. A 1-bit unit cell was used. The manufactured surface is shown in Figure 1.9. As shown in the figure, it is a two-layer structure; the top layer is the reflecting layer, and the bottom layer is the control layer. The conductors at the top layers are connected to stubs at the bottom layer with vias. The pin diodes are placed at these stubs, and by changing their state, the length of the stub and the phase of the reflected wave can be adjusted. The measurement setup they used is shown in Figure 1.9. It is reported that the RIS can steer up to 30 degrees, and it can increase the signal power by 25 dB. The limit for the steering angle is not as high as in [20] because with a 1-bit unit cell, precise control of the phase distribution is not possible, and this makes challenging steerings difficult.

Another RIS example can be found in [23]. A 3-bit unit cell was used at three dif-

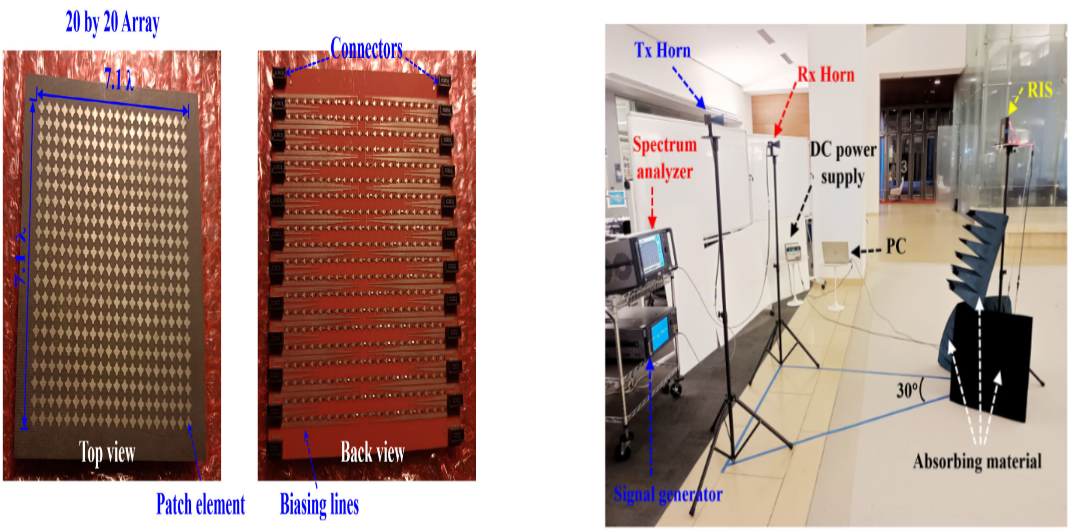

(a) The top and back view of the manufactured RIS example

(b) The measurement setup of the RIS

Figure 1.9: RIS design example [22]

ferent frequencies: 3.3, 3.8, and 4.3 GHz. The bandwidth for each band is around 100 MHz, corresponding to 3%, 2.6%, and 2.3% bandwidths, respectively. The RIS was tested for indoor non-LoS scenarios and was measured to enhance the transmitted signal by up to 40 dB; however, no further information about other capabilities is provided. Another RIS design is given in [24]. This structure has a 2% bandwidth and unlike the other linearly polarized examples, this design is dual-polarized. For reconfigurability, integrated chips that can change their R and C values were used. This concept is similar to varactor diodes; however, the chip is discrete rather than continuous. Despite this, the number of load variations is high (the exact number is not provided), allowing it to act like a continuous phase resolution.In addition to its beam steering capabilities, a novel aspect of this work is that this RIS can also absorb incoming waves up to 30 dB. Examples up to now have used lumped elements for reconfigurability. A RIS design that uses graphene for reconfigurability is given in [13]. This RIS has a very high bandwidth, ranging from 0.1 to 4 THz. It is insensitive to polarization and incoming angles. The RIS can be tuned by adjusting the chemical potential. They showed that the structure can steer the beam and absorb the incoming wave via simulations. As a final example, a RIS design using dielectric resonators is presented in [25]. As mentioned, if the surface is too large compared to its wavelength, users might fall within its near field. This RIS design can adjust its phase distribution to focus the reflected wave to a near-field focal point. The surface and unit cell are shown in Figure 1.10. They demonstrated that using the RIS increases the transmitted signal by up to 17 dB. For the reconfigurability technique, they proposed using liquid crystals. However, they did not produce a reconfigurable prototype and instead validated their design using a frozen surface.

In conclusion, the investigated RIS designs are summarized in Table 1.1. Various methods can be employed to design a RIS, from tunable lumped elements to tunable substrates, and it is also possible to incorporate different phase resolutions and bandwidths. Each design approach involves trade-offs; higher phase resolution enhances the precision of phase distribution adjustment and improves RIS performance, but it also increases surface complexity. Continuous phase resolution, such as with varactor diodes, theoretically offers the most precise phase distribution. However, variations in the tolerances of the varactor diodes on the surface introduce phase errors, thus continuous phase resolutions do not provide ultimate precision. In the literature, beam steering capabilities have been investigated, with the maximum angle mentioned being 45 degrees. Signal enhancement in non-LoS scenarios has also been studied, with maximum enhancements of 40 dB in the far field and 24.7 dB in the near field.

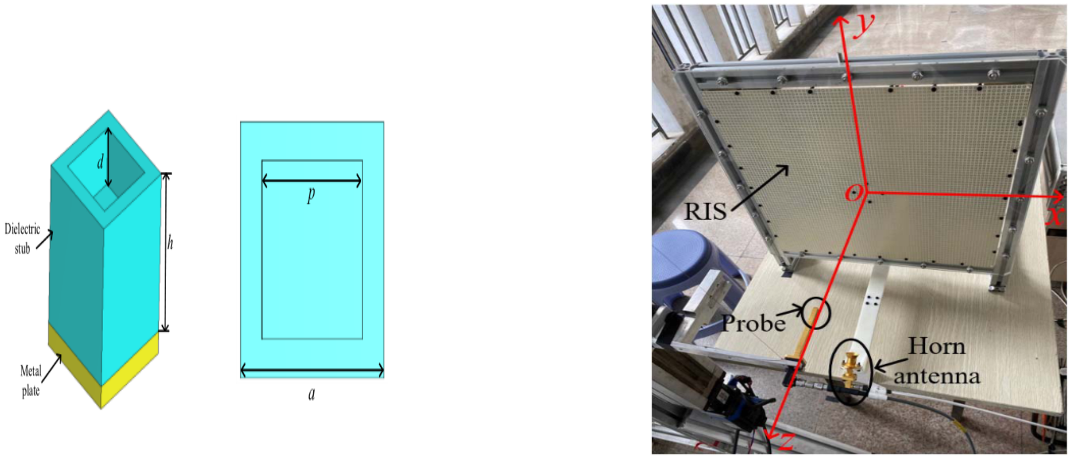

(a) The unit cell for the nearfield focusing RIS example

(b) The nearfield measurement setup of the RIS

Figure 1.10: RIS design example [25]

Table 1.1: Performance Comparison of RIS Designs

Ref.	**Phase Resolution**	**Tuning**	**Frequency**	**Bandwidth**	**Signal Enhancement**	
					Near field	**Far field**
[20]	Continuous	Tunable Load	3.5 GHz	-	-	15 dB
[21]	2-bit	PIN Diode	28 GHz	1 GHz (3.5%)	-	25 dB
[22]	1-bit	PIN Diode	28 GHz	7.56 GHz (27%)	24.7 dB	18.9 dB
[23]	3-bit	PIN Diode	3.3 - 3.8 - 4.3 GHz	100 MHz (3% - 2.6% -2.3%)	-	40 dB
[24]	Continuous	Tunable Load	5 GHz	100 MHz (2%)	-	-
[25]	Continuous	Liquid crystal	26 GHz	-	17 dB	-
[13]	Continuous	Graphene	0.1 - 4 THz	2.9 THz (141%)	-	-

1.4 Overview of Research Work and Thesis Structure

In this thesis first a novel unit cell with high range of phase response is designed. The unit cell consists of nine patches with connections between them, and by altering the states of these connections, the phase response characteristics of the unit cell can be modified. In unit cell PIN diodes are used for reconfigurability. The main advantage of the unit cell from the designs from the literature is that it has high range of phase and the number of bit on the unit cell can be reduced up to 1-bit for cost effective reasons. By reducing the number of bits the phase response range reduced but the cost is reduced also. The Floquet analysis of the unit cell, bit-reducing strategies, and unit cell simulations using PIN diodes are detailed in Chapter 2, where the design of the unit cell is also thoroughly explained.

After designing the unit cell, a passive intelligent surfaces utilizing different states of the unit cell was developed. With these passive surfaces, we demonstrated that the beam can be manipulated using the unit cell. Following the passive intelligent surfaces, we conducted simulations of RIS with PIN diodes. Subsequently, we developed an array synthesis tool that enhances beam manipulation with fewer bits. The detailed design procedure for RIS is provided in Chapter 3.

Finally we produced a RIS and measured it. The measurement setup and results are given in Chapter 3.6.

CHAPTER 2

UNIT CELL DESIGN

As discussed in Chapter 1.2, the design of an RIS primarily involves two key steps: the unit cell design and the surface design. This section outlines the detailed process of designing a unit cell, encompassing critical stages from the initial concept to simulations incorporating PIN diodes. Initially, examples from the literature are presented. Following this overview, we introduce our unit cell design, which features 12-bit reconfigurability, highlighting its unique advantages and distinctions compared to other unit cells described in the literature. Subsequently, we present the phase response results obtained from our simulations. This presentation is followed by a discussion of these results, focusing on their implications and relevance to the design of RIS. Next, the bit reduction method that we used to adjust the number of bits on the unit cell is presented. Then, simulation results to evaluate the performance of the unit cell at different angles of incidence, recognizing the practical scenario where incident waves are not always at normal incidence are given. Finally, the unit cell using a PIN diode model is simulated to enhance the accuracy of our simulations.

The analytical works on RIS emphasize the importance of high phase resolution [19], [26]. This parameter is identified as a fundamental aspect for effective RIS functionality, enabling precise control over the phase of reflected signals and significantly impacting the performance of the system. A high degree of resolution allows for more accurate beam steering and beam shaping capabilities, which are crucial for optimizing communication systems [27]. Recent research has thoroughly investigated the required phase resolutions for RIS [28]–[30]. One of the most significant findings from these studies is that the necessary resolution for effective performance varies according to specific application requirements. For applications where there are no size constraints for the RIS and it is primarily used in the far field, research indicates that even a 1-bit configuration may be sufficient to meet operational demands [29], [30]. This simplicity can lead to significant cost reductions and simplifications in design and deployment. On the other hand, scenarios that involve size constraints or require precise near-field focusing demand higher resolutions. In such cases, the ability to control the phase with greater precision becomes crucial for achieving desired performance outcomes [19], [26], [28].

In the literature, varactor diodes or tunable loads are commonly used to achieve high phase resolution [31], [32]. The phase difference between the incident and reflected wave depends on the current induced on the surface of the unit cell. By changing this current, the phase difference can be controlled. Varactor diodes and variable loads have different characteristics for each biasing voltage. By adjusting the biasing voltage, the phase response of the unit cell can be continuously adjusted. This capability allows for precise control over the phase distribution, enabling effective manipulation of the reflected wave.

An example of a unit cell that uses a variable load is shown in Figure 2.1 [20]. In this design, the capacitance of the capacitor changes with the applied bias voltage, and for different bias voltages, the phase difference between the incident and reflected fields vary. This makes the unit cell very useful for RIS surface design, as it allows for precise phase control. The RIS that is designed using this unit cell has beam steering capabilities up to 45 degrees, and it can increase the received signal power up to 15 dB. Additionally, in Figure 2.2, an example of a unit cell design that uses varactor diodes is shown [32]. In this design, two varactor diodes are used for the unit cell. For different values of biasing voltages, these diodes exhibit different phase curves, allowing for continuous phase control. This capability is crucial for achieving high-resolution phase adjustments, enabling effective manipulation of the reflected wave to meet specific design requirements for RIS surfaces. The RIS prototype using this unit cell achieves low side lobe levels up to -12 dB and increases the received signal power by 26 dB for indoor and 27 dB for outdoor applications. The RIS prototype using this unit cell achieves low side lobe levels up to -12 dB and increases the received signal power by 26 dB for indoor applications and 27 dB for outdoor applications.

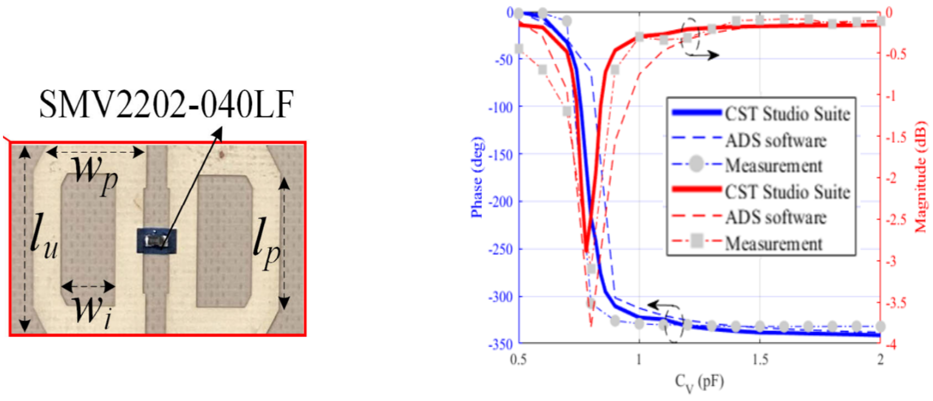

(a) A unit cell example using a variable capacitor for reconfigurability

(b) The simulation and the measurement result of the phase response of the unit cell

Figure 2.1: A RIS unit cell example using a variable load and its phase response curves [20]

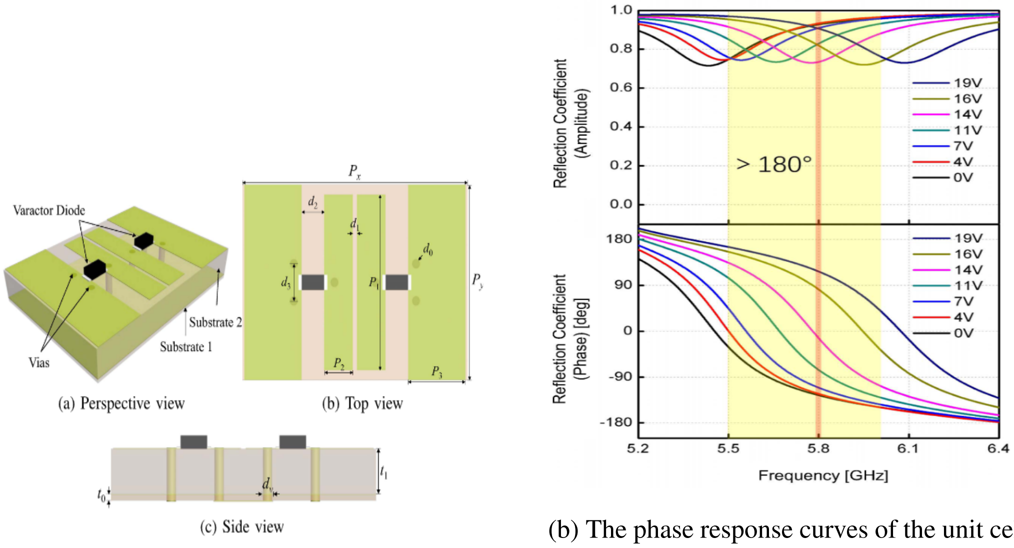

(a) A unit cell example using a varactor diode for reconfigurability

(b) The phase response curves of the unit cell for different biasing voltages applied to the varactor diodes

Figure 2.2: A RIS unit cell example using varactor diodes and its phase response curves [32]

Variable loads and varactor diodes are very useful for achieving high phase resolution, but they are highly sensitive to temperature variations and require precise manufacturing and biasing processes. Small differences between the varactor diodes or in the bias voltages can significantly affect the performance of the design. Therefore, PIN diode-based reconfigurability is also widely used in many designs [23], [33], [34]. PIN diodes can change the phase response of the surface discretely, and they are much less sensitive to environmental factors and more robust compared to varactor diodes and tunable loads. In the OFF mode, PIN diodes block the surface current, while in the ON mode, they allow it. This switching capability changes the surface current and, consequently, the reflected field. This makes PIN diodes a reliable alternative for RIS designs, offering robustness and simplicity in controlling the phase response of the unit cells. A 1-bit example of a unit cell that uses a PIN diode is shown in Figure 2.3 [33]. This design employs a multilayer approach, where the biasing circuit is located at the bottom, and the reflective unit cell is situated at the top. The phase response of the unit cell is illustrated in the figure, demonstrating that the phase difference between the ON and OFF modes of the PIN diode is approximately 180 degrees within the desired bandwidth. A 180-degree phase difference between states is ideal because it effectively discretizes the total 360-degree phase range. To achieve optimal performance with two states, the phase difference should be approximately 180 degrees. Another example is given in Figure 2.4 [34]. This unit cell utilizes two PIN diodes for reconfigurability, allowing for four different states. As shown in the figure, the phase difference between these states is approximately 90 degrees, which is ideal for achieving good discretization and effective phase control. The last example is presented in Figure 2.5 [23]. This unit cell incorporates three PIN diodes for reconfigurability and a capacitor to ease the biasing of the PIN diodes. Ideally, the phase difference between the states should be 45 degrees. However, the design does not achieve a constant 45-degree difference between the states. Despite this, the unit cell still offers more phase states than the 1-bit and 2-bit designs, enhancing its capability to manipulate the reflected wave more precisely.

The comparison table of the unit cell examples is provided in Table 2.1. In this table, the designs are compared in terms of their range of phases, meaning the range of phases that the unit cell can realize, and their bandwidths. Since all designs provide their phase ranges, it allows for an efficient comparison in this aspect. However, only two designs provide their bandwidth results, so only these two designs can be compared in terms of bandwidth.

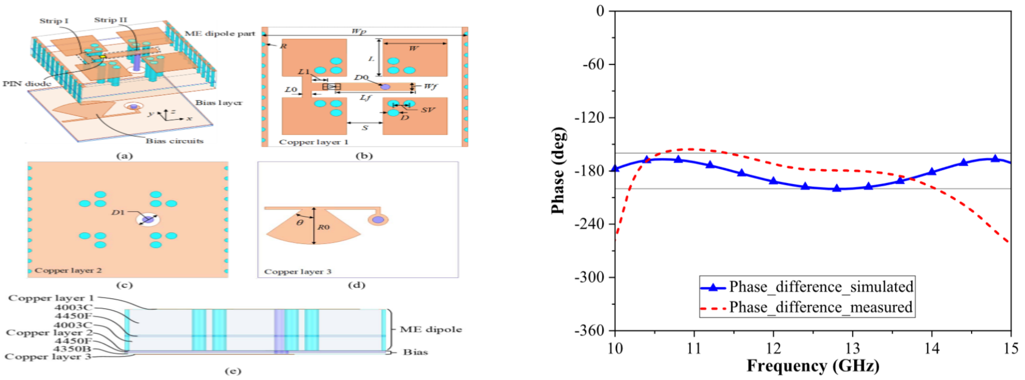

(a) 1 bit unit cell example using pin diode for reconfigurability

(b) The phase difference between the phase responses of the two states of the unit cell

Figure 2.3: A 1 bit RIS unit cell example with its simulated and measurement results [33]

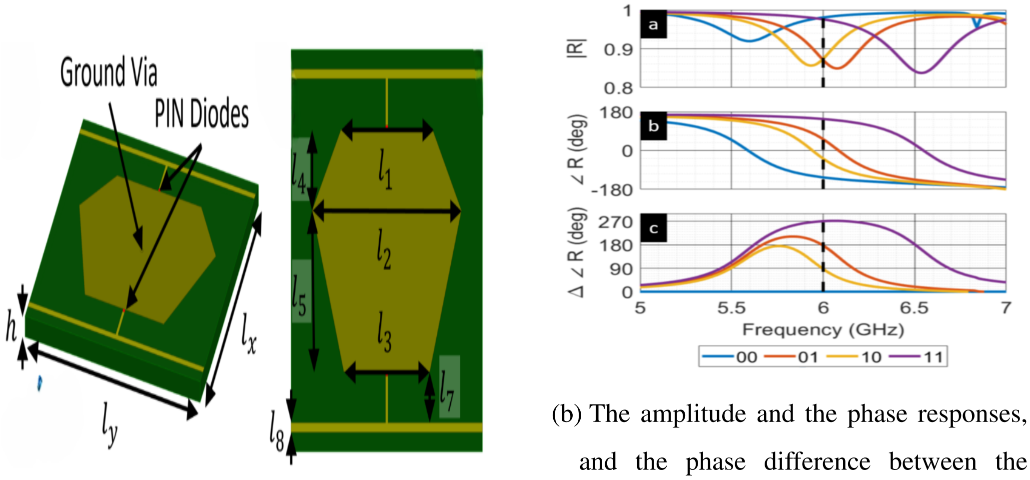

(a) 2 bit unit cell example using pin diode for reconfigurability

(b) The amplitude and the phase responses, and the phase difference between the phase responses of the four states of the unit cell

Figure 2.4: A 2 bit RIS unit cell example with floquet analysis results [34]

2.1 Proposed Unit Cell

After discussing the designs found in the literature, our unit cell design will now be introduced. The proposed unit cell design is shown in Figure 2.6. It features

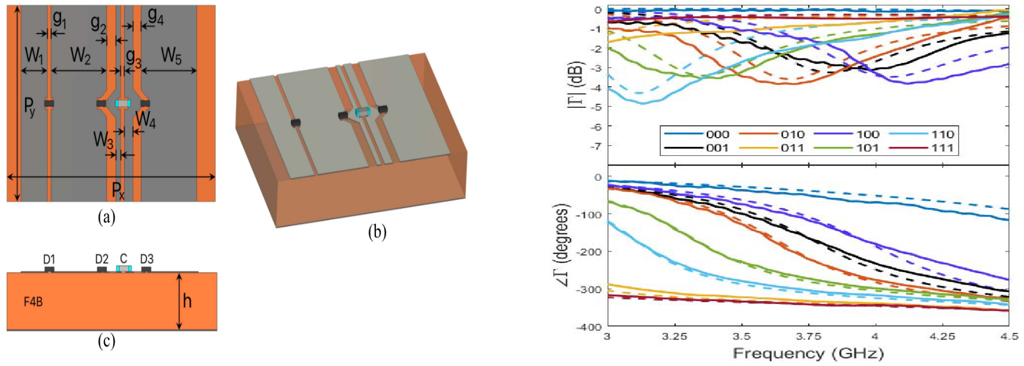

(a) 3 bit unit cell example using pin diode for reconfigurability

(b) The amplitude and the phase response of the unit cell

Figure 2.5: A 3 bit RIS unit cell example with its floquet analysis results [23]

Table 2.1: Comparison of the unit cell designs

Unit Cell	Reconfigurability Method	Bandwidth	Polarization	Range of phase
[20]	Tunable Load	-	Linear	340 degrees
[32]	Varactor Diode	-	Linear	270 degrees
[33]	1 bit PIN Diode	38.4 %	Linear	180 degrees
[34]	2-bit PIN Diode	-	Linear	270 degrees
[23]	3-bit PIN Diode	3 %	Linear	315 degrees

nine small metallic patches interconnected by bridges that represent PIN diodes. The unit cell is similar to pixel antennas [35], which also feature numerous PIN diodes between their patches, enabling high reconfigurability. Our unit cell incorporates 12 connections between the patches, which is important because it allows for a wide phase response. The dimensions are: Ws = 15.04 mm, Wp = 3.52 mm, Wa = 0.32 mm, Wc = 0.64 mm, Hs= 1.528 mm. It is compact, with its size being less than half a wavelength ($\lambda/2$) at the operating frequency 10 GHz. For the substrate, Rogers 4003 is used due to its high-frequency performance characteristics. This material offers a stable dielectric constant and a low loss tangent. In the simulation's initial stages, bridges between the patches exist in the ON state of the diodes and are removed in the OFF state. To enhance the realism of the simulations, these bridges are subsequently replaced with actual PIN diodes.

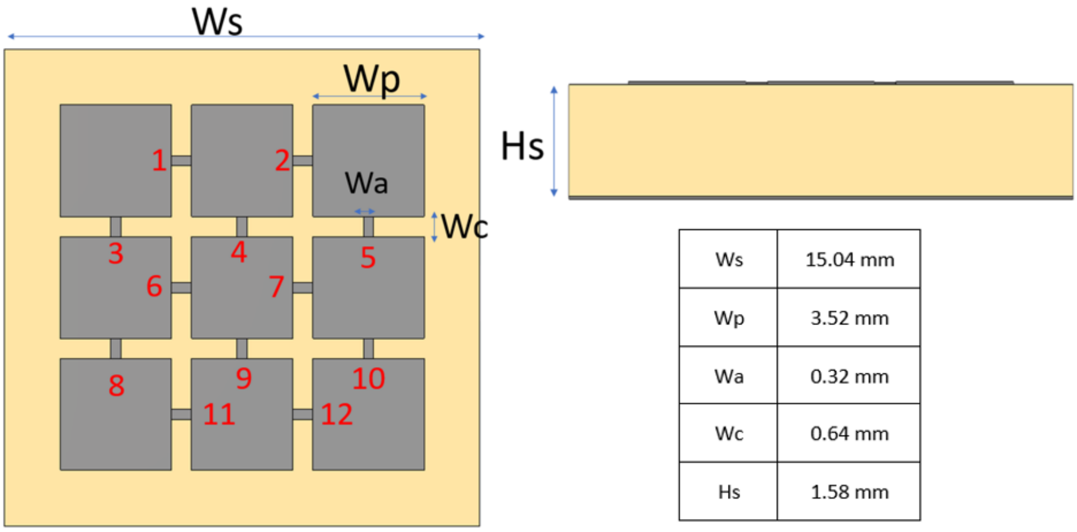

Ws	15.04 mm
Wp	3.52 mm
Wa	0.32 mm
Wc	0.64 mm
Hs	1.58 mm

Figure 2.6: Top and side view of the proposed unit cell design

First, the Floquet analysis for the unit cell was performed, and simulations were conducted using CST Studio. As discussed in Chapter 1.2.1, Floquet analysis can be used to calculate the characteristics of periodic structures. This method assumes that the entire plane is periodically covered with the unit cell.The simulation setup is illustrated in Figure 2.7. The incident field is normal to the surface, with periodic boundary conditions applied. The polarization of the incident wave is vertical. A single port is placed at the top, as the bottom layer is a Perfect electric conductor (PEC).

From the simulations, we used the S_{11} results, which provide information about the reflected field. The amplitude of the S_{11} parameter indicates how much of the incident wave is reflected, while the phase of the S_{11} parameter illustrates the phase difference between the incident and reflected waves. To calculate this phase difference, the phase difference should be measured on the surface of the unit cell. This phase difference, also known as the phase response of the unit cell, is crucial for RIS design. Using these responses, we can design a surface to successfully manipulate the reflected wave. Floquet port simulations were performed for every possible state of the unit cell. Given that there are 12 connections, there are 4096 different states for

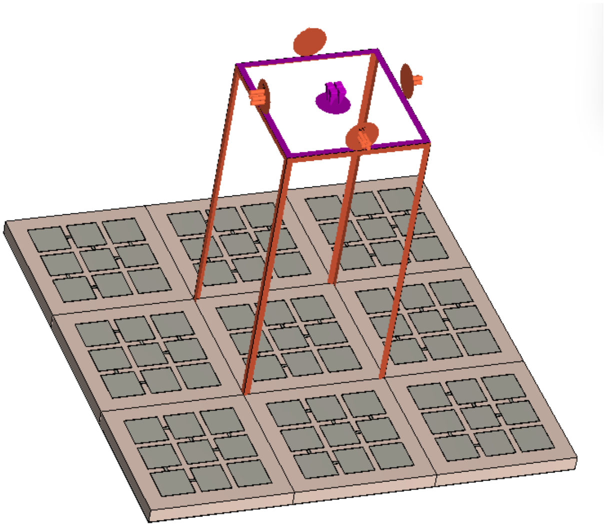

Figure 2.7: Simulation setup for the proposed unit cell

the unit cell. Each state corresponds to a different combination of connections. For example, two different combinations are shown in Figure 2.8. The phase responses for these states are also shown beneath them. The phase response curves show the phase difference between incident and reflected waves for different frequencies. In the first state the phase difference is between -120 and -200 degrees, and in the second state, it is between 105 and 125 degrees. The phase responses differ because different connections modify the surface currents induced by the incident wave, resulting in different reflected waves.

Figure 2.9 displays the phase response results of all states at 10 GHz to simplify presentation and analysis. Figure 2.9a presents a histogram of the phase responses, indicating the number of states that achieve phase values within specified bins. The Figure 2.9b provides a more direct visualization by sorting and plotting the phases of every state from lowest to highest. As illustrated, this unit cell configuration is capable of realizing almost all possible phase responses, demonstrating its extensive reconfigurability. However, most of the phases accumulated near 180 and -180 degrees, causing some states to have very similar phase responses. Phase differences around 0 degrees are much less common than at other degrees.

Additionally, Figure 2.9c and 2.9d provide the phase responses of 4096 states at different frequencies. This plot demonstrates that the phase responses around 180 and

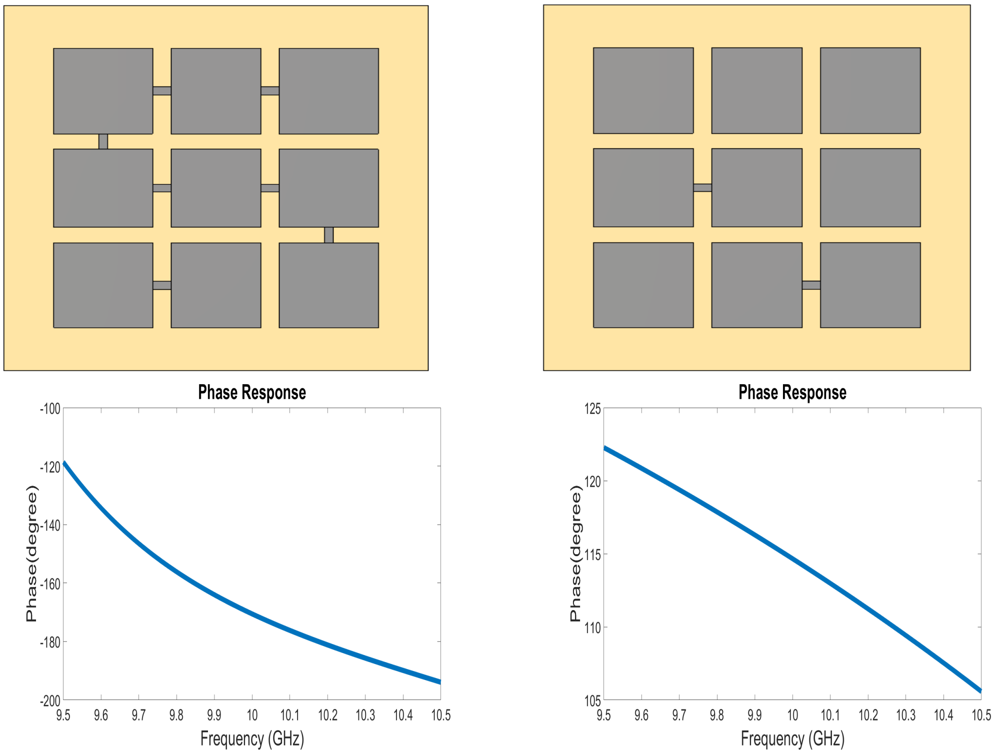

(a) State 1

(b) State 2

Figure 2.8: The unit cell configurations and phase response results for 2 different states

-180 degrees change less across different frequencies compared to other phase responses, particularly those between -100 and 100 degrees. The unit cell is a resonant-type element, and when an element begins to resonate, the phase difference between the incoming and reflected waves shifts from 180 to -180 degrees, so at resonance, the phase responses of the elements have a value of between 180 and -180 degrees. The shift occurs more rapidly as the Q factor of the element increases. As shown in the figure, the phase responses of most elements at resonance deviate significantly across different frequencies. Therefore, phase design curves of the unit cell at different frequencies are not following each other, which means the unit cell has a narrowband characteristic.

As will be discussed in the bit reduction section to efficiently manipulate the surface phase distribution the phase response of the states should be evenly distributed between -180 and 180 degrees. For 12-bit version it is not evenly distributed but since there are 4096 cases it doesn't lead to a performance degration. In contrast, for the 1-bit or 2-bit versions, if the phase responses are not evenly distributed, performance degradation cannot be compensated. Therefore, the states that have phase responses near 0 degrees become crucial in bit reduction. Additionally, since these elements have fewer alternatives, they are very important for surface design. However, they also become the bottleneck for the design due to their narrow bandwidths, as they degrade the SLL of the surface, which will be discussed in Chapter 3.

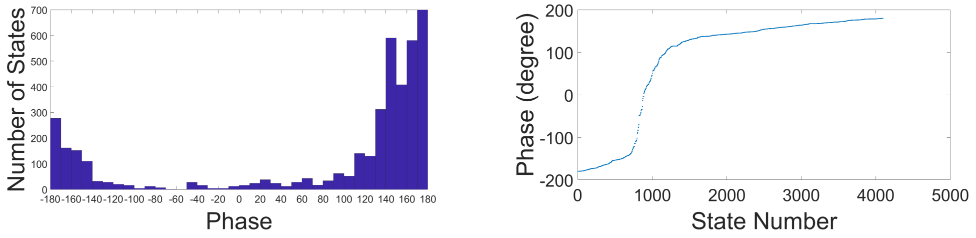

(a) The histogram of the phase responses at 10 GHz

(b) The phase responses of 4096 states at 10 GHz

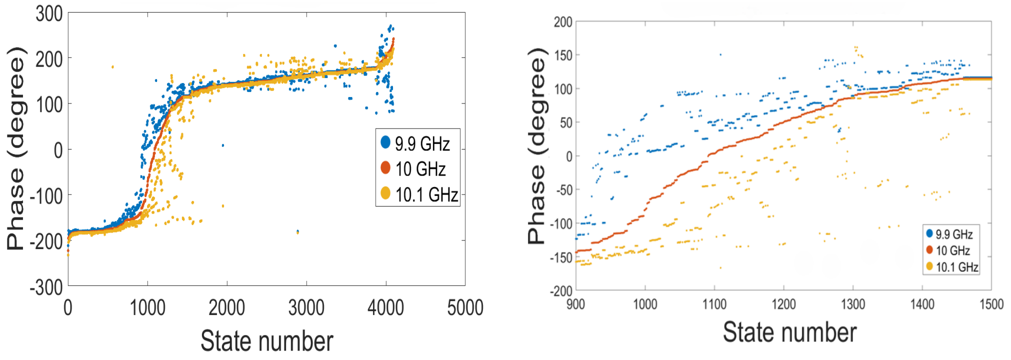

(c) The phase responses of 4096 states at different frequencies

(d) The phase responses of 4096 states at different frequencies

Figure 2.9: The phase response results of 4096 states

The phase response curves demonstrate that this unit cell can realize most phases in the range of -180 to 180 degrees. However, achieving a 12-bit configuration is particularly challenging due to the increasing complexity and cost, especially with larger RIS configurations. Research indicated in [29], [30] suggests that as the size of the RIS grows, the necessity for high-resolution bit control decreases. Therefore, for larger RIS, the number of bits can be reduced. To make this unit cell more versatile for RIS design, we propose an additional feature: the ability to adjust the number of bits based on different complexity needs. For example, to save costs and reduce complexity, the number of bits might be reduced to just 1-bit or 2-bits. The next section discusses this bit reduction in detail.

2.2 Reduction in Number of States

In order to reduce the bit number, we must first determine the desired bit number, N, meaning N connection that can change its states (active bits) and 12-N connection that remains static (static bits). For example, if the desired bit number is 1, just one connection should be selected to change its state while the remaining connections remain static. After deciding the desired number of bits, we should examine the possible N bit variations to determine which variation has the best phase response curve. The best phase response curve is determined by investigating whether its phases are distributed evenly between -180 and 180 degrees. All possible N bit variations are calculated like following: There are $\binom{12}{N}$ different bit combinations possible, each capable of producing $2^{(12-N)}$ distinct stable bit statuses. There are 2^N different states for an N bit unit cell; therefore, from these $\binom{12}{N} * 2^{(12-N)}$ different 2^N phase responses, we should select the set whose consecutive phase differences are closest to $\frac{360}{2^N}$. The algorithm for the bit reduction is shown in Figure 2.10. First, the initial values are defined, and then the possible variations are investigated to determine which one has the best phase response.

To clarify the bit reduction process, two examples are provided in Figures 2.11 and 2.12. In Figure 2.11, the number of bits is reduced to one, and the corresponding unit cell model is shown in Figure 2.11a. The red bridge (10th bridge) represents the active bit, and it exists for the ON state of the diode and is removed for the OFF state. The remaining bridges are fixed (static bits). In Figure 2.11b, the phase responses of the two states of this unit cell are shown. For State 1, the phase response is -170 degrees, and for State 2, it is -178 degrees. This exemplifies improper bit reduction, as the phase difference between the two states is 8 degrees. However, to achieve evenly distributed phase responses, a difference of $\frac{360}{2^1} = 180$ degrees is required.

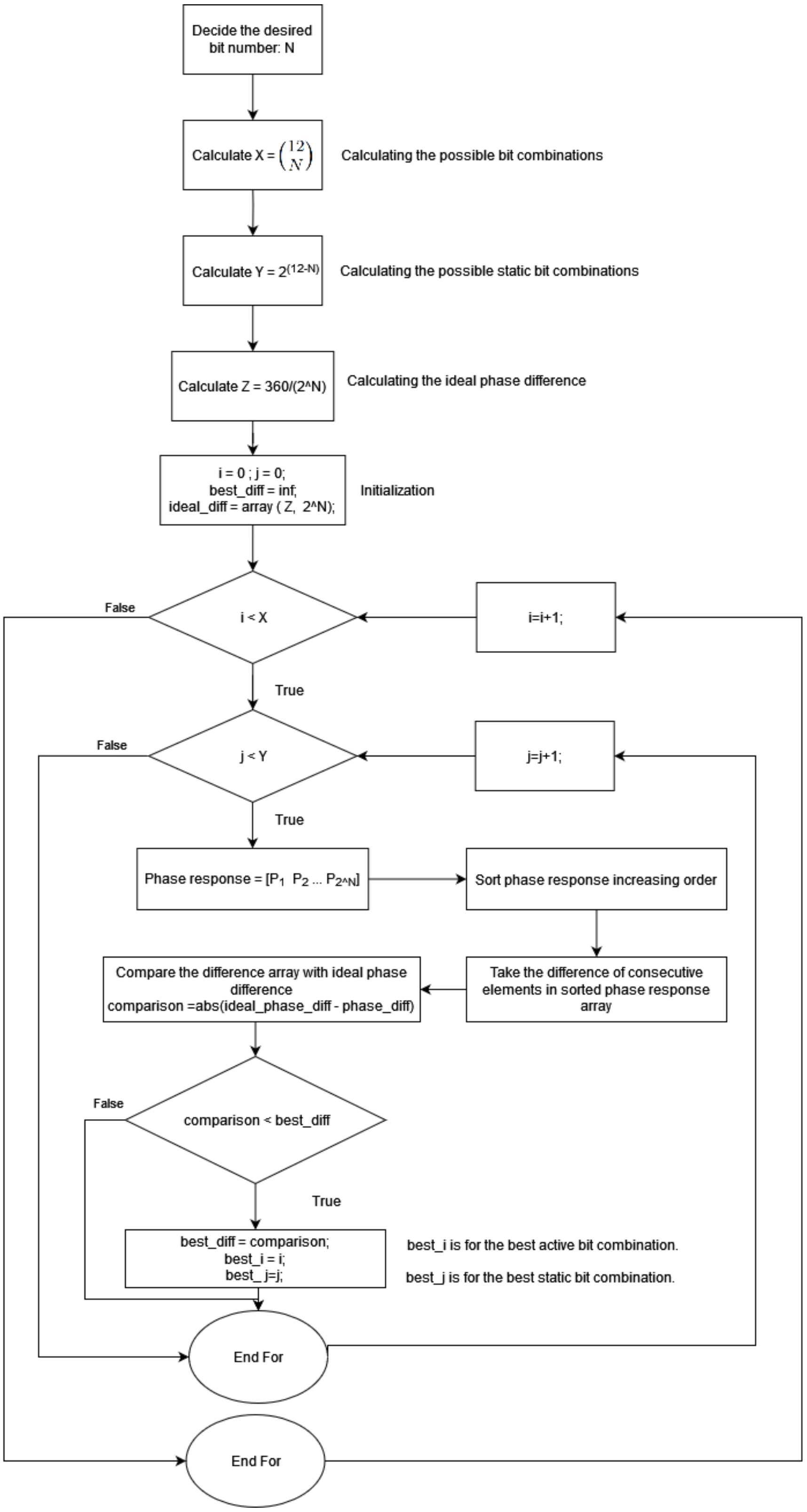

Figure 2.10: The flowchart of the bit reduction algorithm

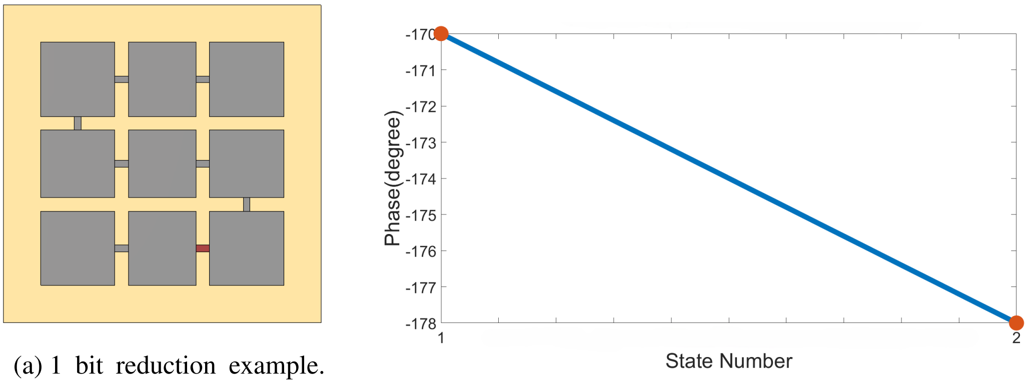

(a) 1 bit reduction example. 7 static 1 active connection between the patches.

(b) 1 bit reduction phase response. Phase difference between states is 8 degrees.

Figure 2.11: Improper bit reduction example. The phase difference between the states is close to each other.

In Figure 2.12, another example of bit reduction is illustrated, where the number of bits is again reduced to one. The corresponding unit cell configuration is shown in Figure 2.12a. In this configuration, the red bridge is identified as the active bit, while the remaining bridges are static bits. The phase response results of the different states of the unit cell are presented in Figure 2.12b. For the first state, the phase response is -43 degrees, and for the other state, it is 143 degrees. The phase difference between the two states is 186 degrees, which is slightly above the ideal 180 degrees expected from a system reduced to a 1-bit representation. This demonstrates that this configuration has better phase responses than the previous example. The phase responses of two states at different frequencies are also shown in the figure. As expected, the state with a phase response of 143 degrees deviates less with frequency changes compared to the state with a phase response of -43 degrees. The bandwidth of the unit cell is defined as the frequency range within which the phase difference remains within ±20 degrees of the desired 180-degree difference [33]. Based on this definition, the 1-bit unit cell has a bandwidth of 90 MHz, which is very narrow. This demonstrates that the bit-reduced unit cell operates properly at the desired frequency but has a very narrow bandwidth.

In Figures 2.13 and 2.14, examples of bit reduction to two and four bits are displayed. In these examples, the red bridges represent the active bits whose states can be ad-

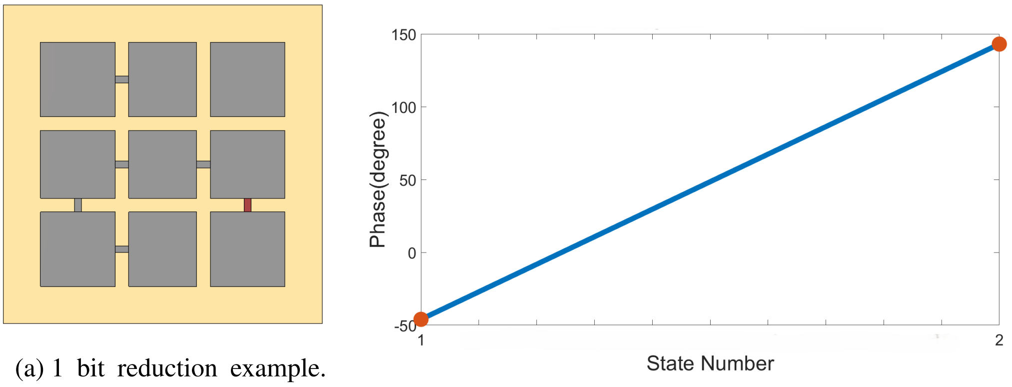

(a) 1 bit reduction example. 5 static 1 active connection between the patches.

(b) 1 bit reduction phase responses. The phase difference between the states is 186 degrees.

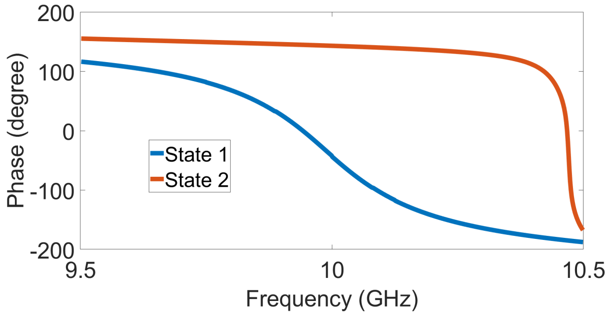

(c) 1 bit reduction phase responses at different frequencies.

Figure 2.12: Proper bit reduction example. The phase difference between the states is close to 180 degree which is ideal for 1 bit unit cell.

justed, while the remaining bridges remain static. The phase responses of the 2-bit unit cell are presented in Table 2.2. For reduction to two bits, the phase responses for the states are recorded as -166, -83, 23, and 114 degrees, leading to phase differences of 83, 106, 91, and 80 degrees, respectively. These observed phase differences slightly deviate from the ideal 90 degrees expected for a two-bit unit cell configuration. The phase responses of the states at different frequencies are also illustrated in the figure. As expected, states 2 and 3 exhibit greater deviations with frequency changes, thereby limiting the bandwidth. Applying the same ±20 degrees criterion, the bandwidth is determined to be 85 MHz, which is notably narrow.

The phase responses of the 4-bit unit cell are presented in Table 2.3. The ideal phase difference is 22.5 degrees. Although the phase difference reaches up to 39 degrees,

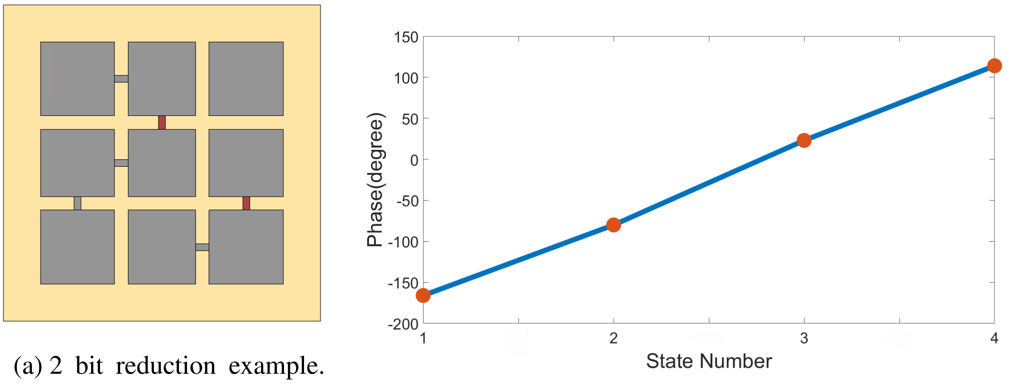

(a) 2 bit reduction example. 4 static 2 active connection between the metallic patches.

(b) 2 bit reduction phase responses. The phase responses are evenly distributed and the difference between the consecutive phases is close to 90 degree.

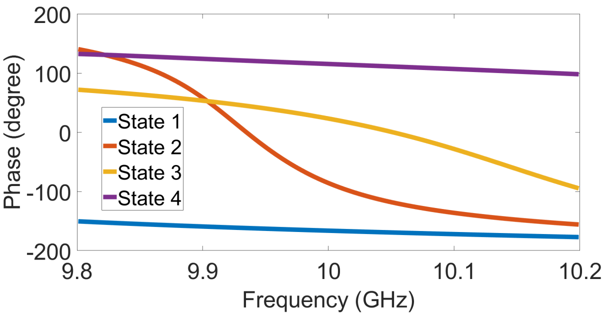

(c) 2 bit reduction phase responses at different frequencies.

Figure 2.13: Bit reduction example to 2 bit

Table 2.2: 2 Bit Unit cell phase responses

State Number	Phase Response (Degree)	Phase Difference between Previous State(Degree)
1	-166	80 (between 4th state)
2	-83	83
3	23	106
4	114	91

overall, the phase differences approximate the ideal value.

The bit reduction capability of this unit cell is a critical aspect due to the inherent challenges associated with employing high bit resolutions in larger arrays. The necessity

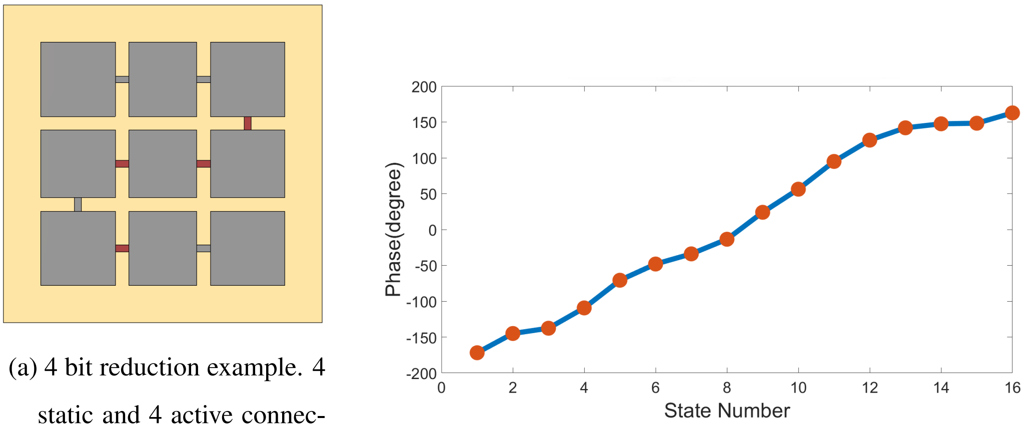

(a) 4 bit reduction example. 4 static and 4 active connections.

(b) 4 bit reduction phase responses.

Figure 2.14: Bit reduction example to 4 bit

of reducing the number of bits becomes unavoidable under such circumstances. The examples provided, demonstrating 1-bit, 2-bit, and 4-bit unit cell configurations can efficiently manage bit reduction while preserving the integrity of phase distributions. Notably, the phase distributions observed in these examples closely approximate ideal distributions.

2.3 Performance at Different Incidence Angles

The simulations conducted thus far have been for normal incidence; however, the performance of the unit cell at various angles of incidence is also crucial, as the direction of incident signals is not always perpendicular in practical applications. To investigate the performance of the unit cell at different incidence angles, we have chosen to use a 2-bit variation of the unit cell. This choice is due to the challenge of presenting results for all 4096 states within the confines of this thesis.

In Figure 2.15, the performance of the unit cell at various angles of incidence is illustrated. It is observed that the phase difference between the states remains relatively consistent up to an angle of 20 degrees. However, beyond this threshold, the phase deviation begins to increase.

Performance analysis reveals that control over the phase distribution begins to de-

Table 2.3: 4 bit unit cell phase responses

State Number	Phase Response (Degree)	Phase Difference Between Previous State(Degree)
1	-172	20 (between 16th state)
2	-145	27
3	-137	8
4	-110	27
5	-71	39
6	-48	23
7	-34	15
8	-14	20
9	24	30
10	56	32
11	94	38
12	124	30
13	141	17
14	147	6
15	150	3
16	168	18

grade when the incidence angle exceeds 20 degrees. The extent and impact of this degradation on the phase distribution will be thoroughly investigated in the surface design chapter. This analysis will provide deeper insights into the operational limitations under oblique incidence conditions.

2.4 Simulations of Unit Cell with PIN Diode

In RIS manufacturing, we have chosen to utilize PIN diodes due to their low cost and ease of deployment. Therefore, following the initial unit cell simulations that incorporated metal bridges, it is essential to conduct further simulations using PIN diodes. This step will enhance the realism of our simulations, making the results

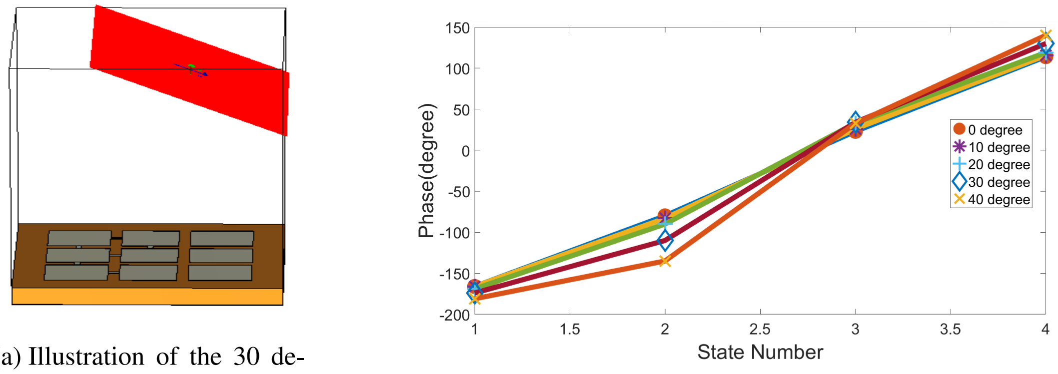

(a) Illustration of the 30 degrees incidence angle

(b) Phase response results at different incidence angles

Figure 2.15: Floquet simulation results of the proposed unit cell at different incidence angles

more representative of real-world conditions.

A PIN diode is a semiconductor device that includes a heavily doped P-type layer, an undoped intrinsic layer, and a heavily doped N-type layer. At RF frequencies, the PIN diode acts similarly to a current-controlled resistor. Due to its intrinsic layer, when forward biased, it allows current to flow in one direction, and when reverse biased, it blocks the flow. This capability makes PIN diodes useful for RF switches [36].

PIN diodes play a critical role in the development and functionality of reconfigurable antennas, where they are frequently used to dynamically change the radiation pattern, as seen in pixel antennas [35], or to modify their operational bandwidth [37]. In addition to their application in reconfigurable antennas, PIN diodes are extensively utilized in the field of RIS technology. Their ability to switch states rapidly makes them highly effective in RIS configurations [38], [39].

For the simulation stages of RIS incorporating PIN diodes, it is standard practice to employ the RLC equivalent circuit model of the PIN diode. This model aids in accurately predicting the behavior of the diodes under various electrical conditions, thereby ensuring that the simulations are as close to real-world performance as possible. The circuit equivalent model is shown in Figure 2.16. The equivalent model consists of a series RL circuit for the ON state and an RLC circuit for the OFF state. The values for these elements are taken from the datasheet of MACOM's AlGaAs

Flip Chip PIN Diode MA4AGP07. This particular PIN diode is well-suited for the unit cell due to its compact size and ability to operate at higher frequencies, up to 40 GHz. The specified values are: L = 0.05 nH, R_{on} = 4.2 Ω, R_{off} = 300 $k\Omega$ and C_{off} = 0.042 pF.

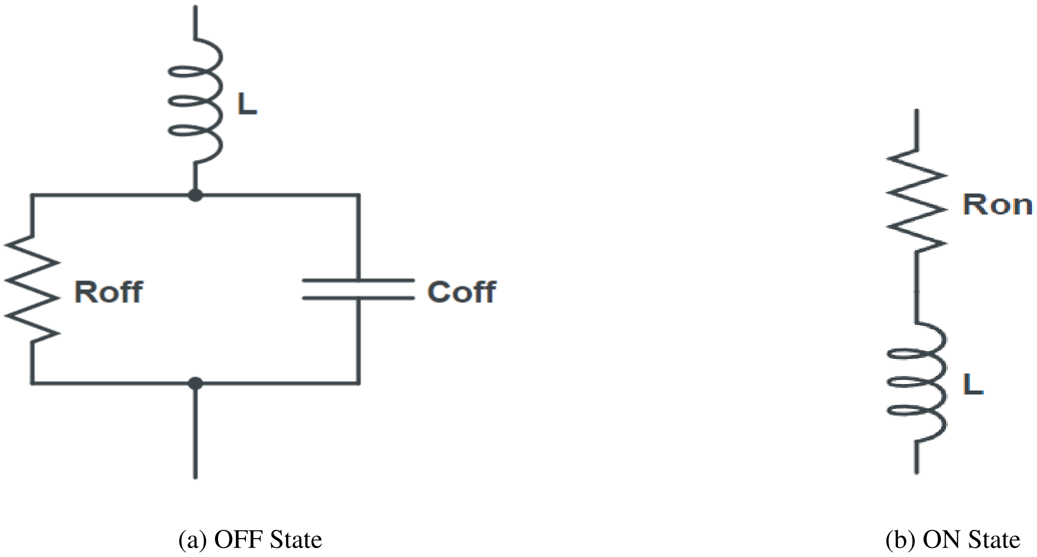

(a) OFF State (b) ON State

Figure 2.16: Equivalent Circuit Model for PIN Diode

To incorporate this model into the simulations, lumped element models are used within the CST software environment. In CST, a lumped element can be defined between two edges, allowing for detailed component modeling. At the unit cell simulations, lumped element models of the PIN diodes are defined between the edges of the active metal bridges as shown in Figure 2.17. Two distinct lumped elements are defined in the simulations for the ON and OFF states of the PIN diode. Depending on the state of the PIN diode, the lumped element model can be switched between these two options.

For the simulations, the reduced 1-bit unit cell is used. Figure 2.18 shows a 1-bit unit cell with a PIN diode, while Figure 2.18b presents the phase response results of the unit cell with both the metal bridge and the PIN diode. For the phase response results, a slight difference was expected because the metal bridges act as perfect electric conductors (PEC), but for the ON mode of the PIN diode, there is minor resistance and an inductor which slightly changes the current flow. Furthermore, in the OFF

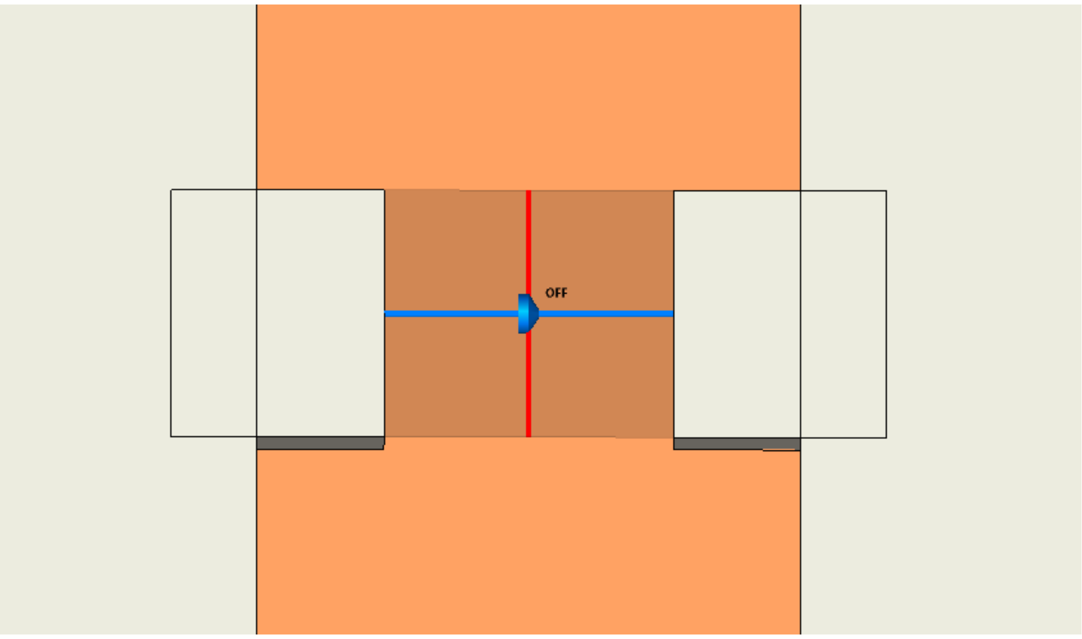

Figure 2.17: Lumped Element in CST

mode, the metal bridge is completely open, whereas the PIN diode presents a very high resistance, suggesting that a slight current may still flow even in the OFF mode. The phase response results of the simulations with PIN diodes are shown in Table 2.4. Phase responses are -45 and 138 degrees, resulting in a phase difference of 183 degrees, which agrees well with the metal bridge case.

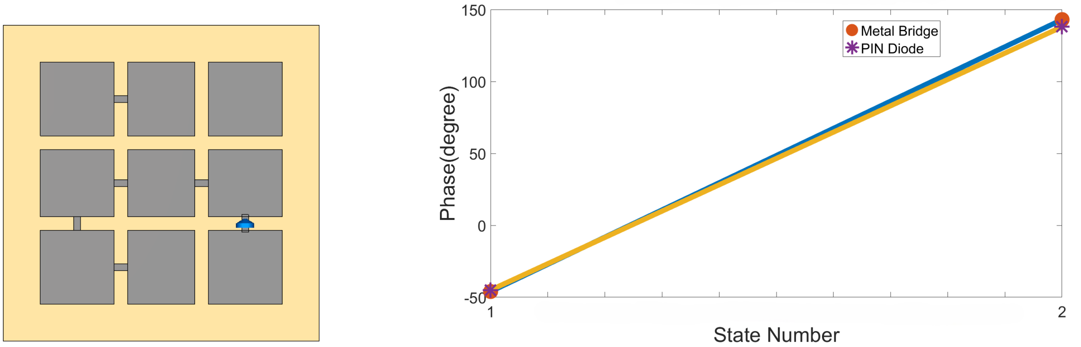

(a) 1-bit unit cell with PIN diode model

(b) Phase response results of the unit cell with PIN diode and metal bridge

Figure 2.18: CST model and simulation results of unit cell with PIN diode

Table 2.4: Comparison of 1-bit unit cell with PIN diode and metal bridge

State Number	Phase Response (Degree)	
	PIN Diode	Metal Bridge
1	-46	-46
2	138	143

Simulations of unit cell with PIN diodes are important for estimation of performance in practical usage. Initially, metal bridge configurations on unit cells are employed to quickly obtain preliminary results. However, conducting comprehensive PIN diode simulations is vital before moving forward to next phases. This step is crucial not only for verifying the initial findings but also for providing robust justification for the design choices made. The same method will be applied in the surface design phase. Each step will be discussed in detail in Chapter 3. Initially, full-wave simulations using unit cells with metal bridges are conducted to quickly obtain preliminary results. Following the metal bridge simulations, PIN diode simulations will be performed. Bias lines of PIN diodes will also be included in the simulations.

CHAPTER 3

REFLECTING SURFACE DESIGN

The second phase of the RIS design process, which is the focus of this chapter, is the design of reflecting surface. Fundamental principles related to the adjustment of phase distribution on the surface were introduced in Section 1.2. In this chapter, a thorough exploration of these principles is conducted to provide a deeper understanding. It begins with an explanation of phase distribution, illustrating how it can be arranged to manipulate the reflected wave. Following this, the phenomenon of spatial delay is examined in detail. The impact of spatial delays on phase distributions is explored through theoretical discussions and practical examples, demonstrating how these delays affect the phase at different points on the surface. Then the importance of the unit cell in the overall functionality of the RIS will be emphasized, illustrating its critical role in manipulating phase distribution. For this illustration, the previously designed unit cell, which is detailed in the preceding chapter, is utilized. Following this, the next step involves the design of a passive surface, constructed using unit cells integrated with metal bridges. These simulations are essential as they provide critical verification of the concept by demonstrating that these unit cells can effectively manipulate the reflected wave. Furthermore, a detailed discussion on the capabilities and limitations of the RIS will be included to provide a comprehensive understanding of its operational scope and potential constraints. This discussion is crucial for recognizing the practical aspects of RIS technology in real-world applications. Finally, to further ensure the operation in practical application, additional surface simulations incorporating a PIN diode will be conducted.

3.1 Phase Distribution of Reflected Wave Over the Surface

The phase distribution of reflected field on the surface is a critical factor in determining the characteristics of the outgoing wave, as this distribution directly influences the wave's behavior. To calculate the properties of the outgoing wave, array factor calculations are employed. The array factor is a function determined by the elements' amplitude, phase, spacing, and geometric arrangement [40]. Figure 3.1 displays 1D linear array and 2D planar array structures. The equations below illustrate the derivation of the array factor. Equations 3.1 and 3.2 demonstrate the calculation of the total electric field. In the equations, A_i represents the amplitude and β_i the relevant phase of the element. $\mathbf{f}(\theta, \phi)$ is the radiation pattern of a single element. The variable r denotes the distance to the farfield point, $\mathbf{a}_r$ is the unit vector from the origin in the direction of the farfield point, and $\mathbf{r}_i$ is the vector between the origin and the i-th element. R_i=r- $\mathbf{r}_i$.$\mathbf{a}_r$ measures the distance between the i-th element and the farfield point. Then, in equation 3.3, the definition of the array factor is given. It is the function that determines the total electric field when multiplied with the electric field of an element of an array. Subsequently, the array factor is illustrated in 3.4. In the derivations, $\mathbf{f}_i(\theta, \phi)$ is assumed identical for all elements, which is not entirely accurate because, although all elements' radiation patterns are the same, mutual coupling occurs when they are assembled. However, for initial steps, this is a very good assumption to simplify the process. At later stages, mutual couplings will be included in full-wave simulations.

$$\mathbf{E}_{TOTAL} = \sum_{i=1}^{N} \mathbf{E}_i \tag{3.1}$$

$$\mathbf{E}_i = A_i e^{j\beta_i} \mathbf{f}_i(\theta, \phi) \frac{e^{-jk_0(r - \mathbf{r}_i . \mathbf{a}_r)}}{4\pi r} \tag{3.2}$$

$$\mathbf{E}_{TOTAL} = (ArrayFactor)\mathbf{E}_{element} \tag{3.3}$$

$$AF = \sum_{i=1}^{N} A_i e^{j\beta_i} e^{-jk_0 \mathbf{r}_i . \mathbf{a}_r} \tag{3.4}$$

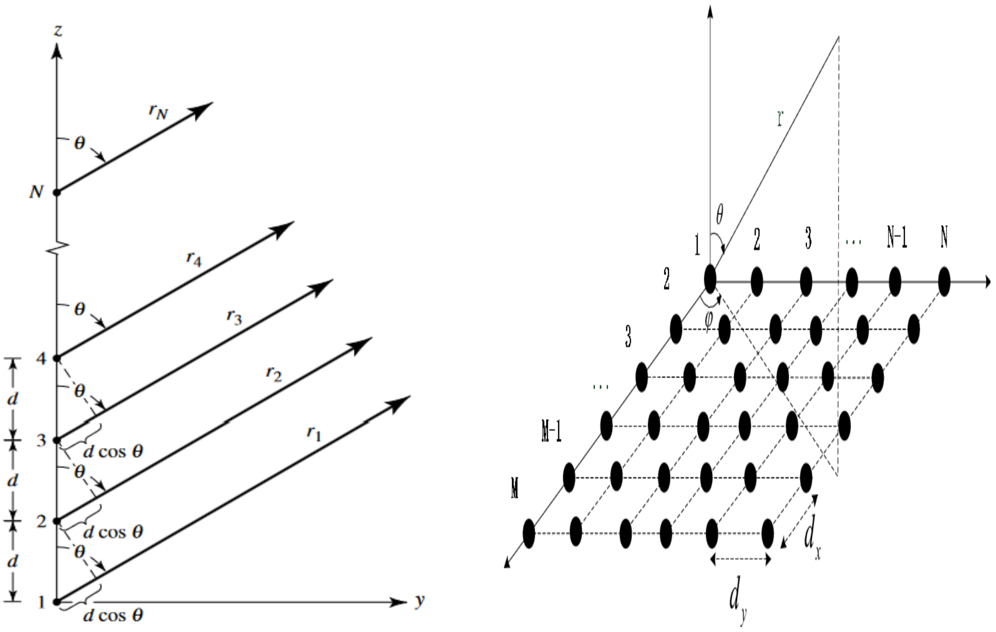

(a) 1D Linear Array [41]

(b) 2D Planar Array [42]

Figure 3.1: Two Array Topologies

As demonstrated by the equations, by adjusting the phase of the elements, both the array factor and the radiation pattern can be modified. Subsequently, examples of the desired phase distribution necessary to steer the outgoing wave to a specific angle are provided. For instance, in Figure 3.2, two examples of such desired phase distributions are illustrated. The first figure demonstrates a phase distribution designed to tilt the outgoing wave by 10 degrees, while the second aims for a 30-degrees tilt. Both designs are implemented over a surface of size $5\lambda \times 5\lambda$. As observed from the figure, the phase change in the 30-degrees phase distribution is more rapid than in the 10-degrees distribution because achieving a greater tilt angle necessitates a more significant phase adjustment over the same surface area, resulting in a steeper phase gradient. Although the ideal phase distributions would be continuous to allow precise control over the wave's direction, the physical design constraints imposed by using a $\lambda/2$-sized unit cell limit this capability. Since each unit cell spans a $\lambda/2$ segment of the surface, phase adjustments are confined to these discrete intervals, allowing modifications only in $\lambda/2$ increments.

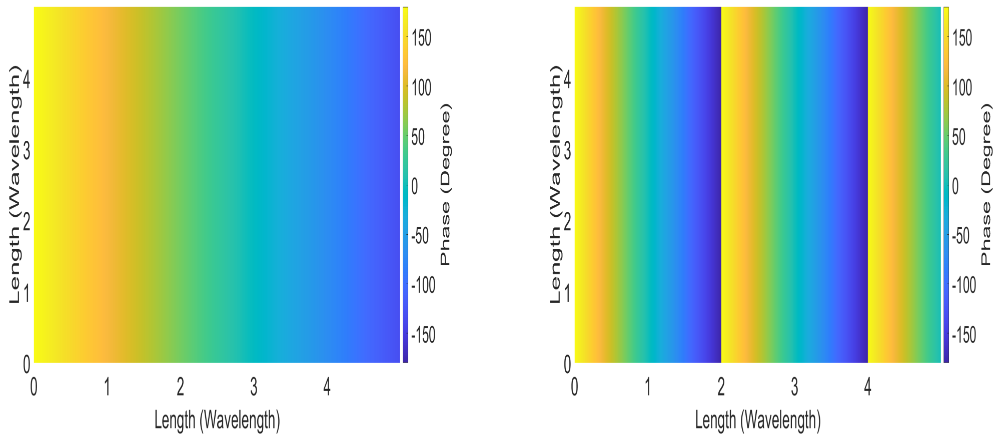

(a) The Desired Phase Distribution to Steer the Beam to 10 Degree

(b) The Desired Phase Distribution to Steer the Beam to 30 Degree

Figure 3.2: Two Phase Distribution Example

The calculation of desired phase distributions that used to manipulate the outgoing wave, is explained. Steering is presented as just one example of the manipulations that can be achieved by changing phase distributions. Additional manipulations will be discussed in Chapter 3.2. Following the calculation of the phase distribution, its realization will be discussed. Spatial delay is identified as the first factor to be considered when adjusting the phase distribution of the surface and the phase response is the second. As in Equation 3.4, the β_i is the relevant phase of the element in RIS this phase consist of the spatial delay and the phase response. The combination of these two creates the relevant phase of the element and combination of these phases creates the phase distribution of the surface. Therefore array factor equation can be written as:

$$AF = \sum_{i=1}^{N} A_i e^{j(\beta_{pr_i} + \beta_{sd_i})} e^{-jk_0 \mathbf{r}_i . \mathbf{a}_r} \tag{3.5}$$

$$\beta_i = \beta_{pr_i} + \beta_{sd_i} \tag{3.6}$$

$$\beta_{pr_i} = \beta_{sd_i} - \beta_i \tag{3.7}$$

Where β_{pr_i} is the phase response of the element and β_{sd_i} is the spatial delay at the element's position.

Spatial delay is identified as the phase difference between various positions on the surface, caused by the delay of the incoming signal. An illustration of this is provided in Figure 3.3. Examples of spatial delay in reflectarrays are presented in Chapter 1.2.2. In the case of the RIS, the spatial delay may exhibit a slight difference, as most of the incident wave are assumed as a planewave. For instance, if the feed is placed at the center of the surface at a distance in a reflectarray, phase differences will be observed at various positions. However, if the incident wave is assume as a planewave arriving at normal incidence from the far field, no spatial delay will be observed on the surface.

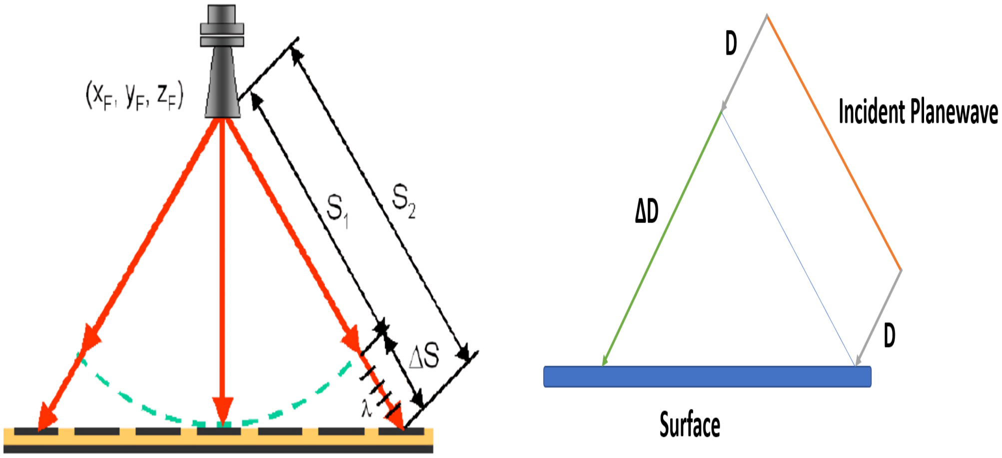

(a) The spatial delay illustration for reflectarray

(b) The spatial delay illustration for planewave incidence

Figure 3.3: Two spatial delay illustration

In Figure 3.4, two different examples of spatial delay distribution are presented. The first example shows the spatial delay of an incident wave arriving at a 10-degree angle on the surface. The size of the surface is 5λ x 5λ. Given the -10 degree incident angle, the wave first encounters the surface at the left edge, which is used as the reference point for plotting the spatial delay at other positions on the surface. The reference phase is set to -180 degrees. As depicted in the figure, the spatial delay increases from left to right due to the incident wave's delay. The second example shows the spatial delay for an incident angle of -30 degrees. Similarly, the left edge is used as the reference point with a reference phase of -180 degrees. In this case, the spatial delay also increases from left to right; however, due to the larger incident angle of -30 degree, the rate of change in spatial delay is significantly faster compared to the -10 degree case. The plot exhibits two sudden changes in spatial delay, which occur because the delay is plotted within the -180 to 180 degree range. When the spatial delay exceeds 180 degrees, it wraps around to -180 degrees, creating an apparent discontinuity in the plot, although there is no actual discontinuity.

It is important to note that there is a 180 degrees phase difference between the spatial delay at the surface when incident angle is a specific angle and the required phase distribution of the surface that steer the outgoing wave to the corresponding angles. To clarify this effect, consider an ordinary PEC surface. When a wave arrives at an angle θ, the reflected wave departs at a $-\theta$ angle. This occurs because, according to the law of reflection, the incident and reflected waves form the same angle with the normal to the surface, as demonstrated in Figure 3.5. Consequently, an incident wave arriving at an angle θ induces phase distributions similar to those required when the desired outgoing direction is $-\theta$. Therefore, the spatial delay for a wave with a θ degree incident angle and the desired phase distributions for a θ degree outgoing wave have the same pace phase differences but opposite direction which results a 180 degree phase differences.

The second factor to consider when adjusting the phase distribution on an RIS is the phase response of the individual elements composing the surface. As discussed in the previous chapter, the phase response of an element is defined by the phase difference between the incident and reflected waves. By using this phase difference, the phase distributions on the surface can be adjusted, thereby altering the direction of the reflected wave. The calculation of the required phase response is given in equation 3.7.

The required phase distributions for a 30-degree tilt are shown in Figure 3.6a. In this example, a normal incident planewave illuminates the surfaces, therefore there

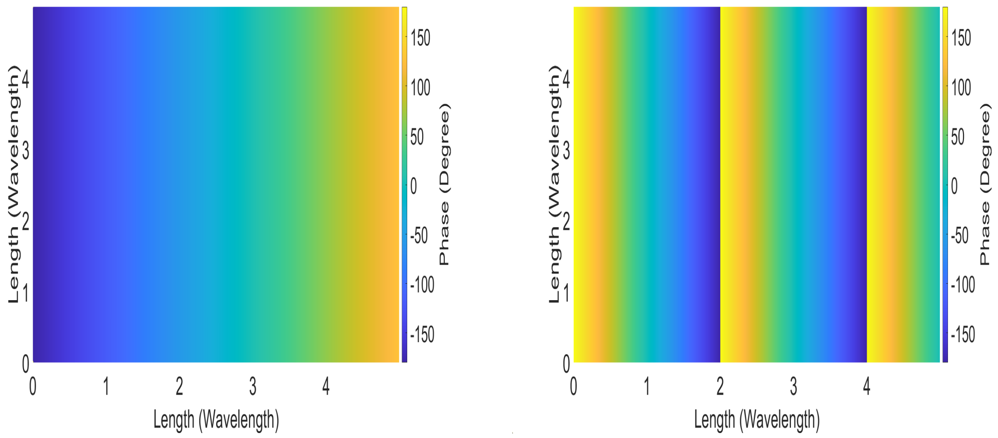

(a) The spatial delay when the incident angle is 10 Degree

(b) The spatial delay when the incident angle is -30 Degree

Figure 3.4: Two spatial delay example

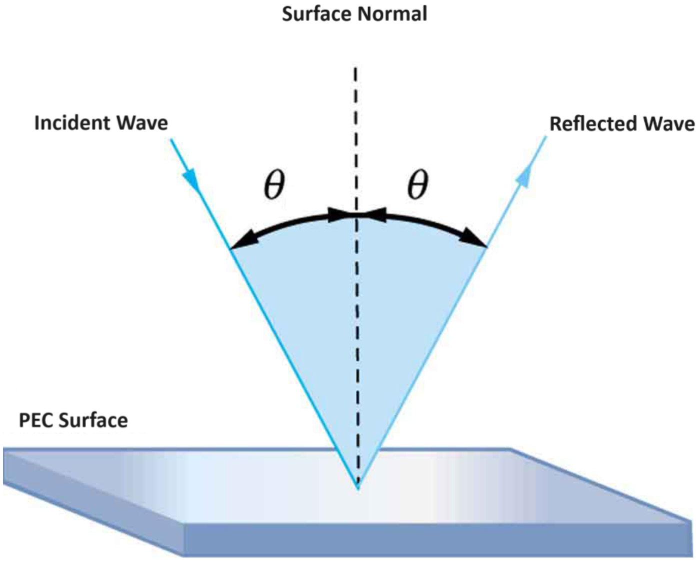

Figure 3.5: The Law of Reflection [43]

is no spatial delay at the surface. Since there is no spatial delay, the required phase response and the desired phase distribution are identical.

To realize the required phase distributions, the continuous phase distributions must first be converted into discrete ones with a size of $\lambda/2$, matching the unit cell size. The discrete required phase distributions are shown in Figure 3.6b. In this figure, for example, the required phase for the first column is 0 degrees. The corresponding unit cell that exhibits a phase response of 0 degrees is used to achieve this. Since the goal is to tilt the wave in the x-direction, there is no need to alter the phase in the y-direction. The required phase for the second column is -90 degrees, and the corresponding unit cell that has a -90-degree phase response must be identified for this column. This process must be repeated for each column to obtain the required phase distributions necessary to steer the reflected wave to 30 degrees.

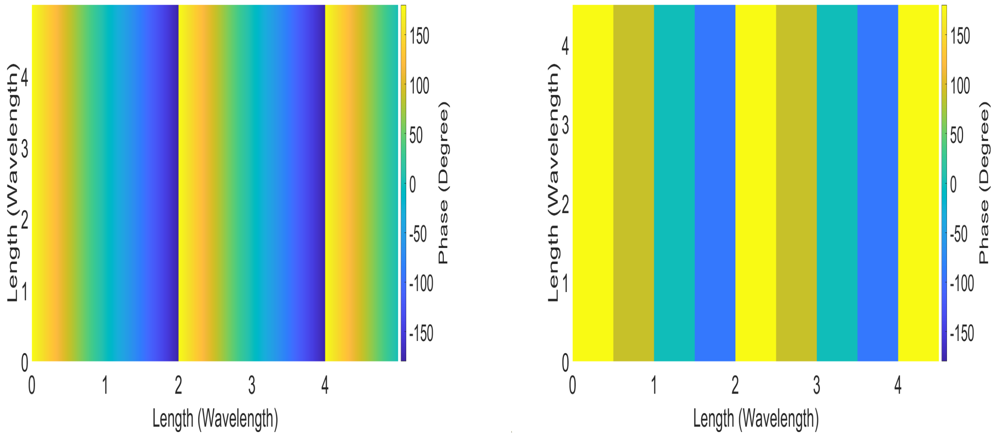

(a) The continuous required phase response to steer the beam to 30 degree when incident angle is 0 degree

(b) The discrete required phase response to steer the beam to 30 degree when incident angle is 0 Degree

Figure 3.6: Required phase response example

Another example is given in Figure 3.7. In this scenario, the incident wave arrives at a 10-degree angle, and the desired reflected wave position is 30 degrees. To determine which unit cell to use, the spatial delay is subtracted from the required phase distributions. The result of this subtraction indicates the required phase difference at every location. According to this figure, for the first column, the required phase difference is -180 degrees; therefore, the corresponding unit cell exhibiting a similar phase response value for that column must be used. This same process must be applied to every other column. Thus, using this method, surfaces are designed to manipulate the wave and conduct 3D EM simulations.

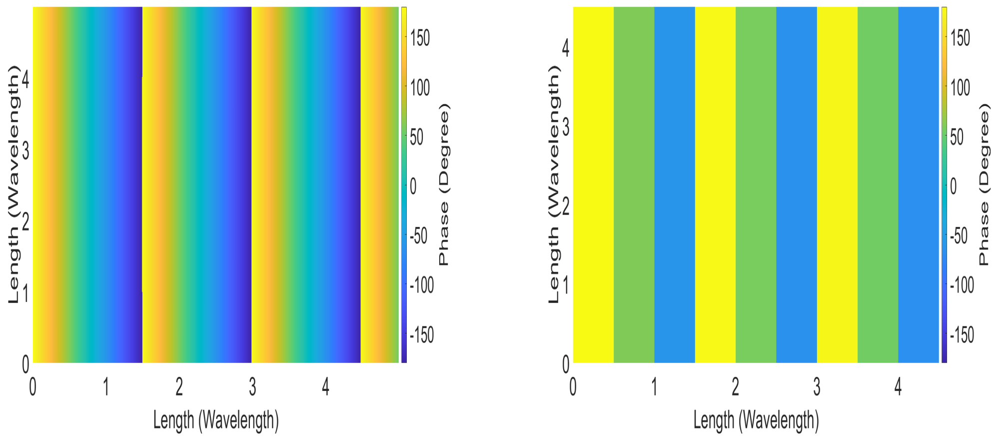

(a) The continuous required phase response to steer the beam to 30 degree when incident angle is 10 degree

(b) The discrete required phase response to steer the beam to 30 degree when incident angle is 10 degree

Figure 3.7: Required phase response example

3.2 Capabilities of the RIS

The capabilities of intelligent surfaces have been presented in detail in the literature [27], [38], [44]. As discussed in [27] the main capabilities are beam steering, beam scattering, multiple beam generation, beam focusing, and vortex beam generation. In addition to these capabilities, we will also show that using our proposed unit cell absorption is also possible. Making absorbing surfaces is a very well investigated area [45], [46]. However, having a unit cell that have both absorbing and reflecting modes and for reflecting modes it has a capabilities to adjust the phase distribution is relatively new area and has a few research on this area. Since vortex beam generation is not a focus in the context of RIS, it is not detailed in this chapter. However, other capabilities, starting with beam steering, are explained in detail.

- **Beam Steering:** One of the most researched capabilities of RIS technology is beam steering. This capability enables RIS to steer the wave to non-line-of-sight (non-LoS) directions to further improve the coverage area. This capability can also improve signal quality by directing the beam to a particular user when choosing from multiple users. To steer the beam to the desired direction, there

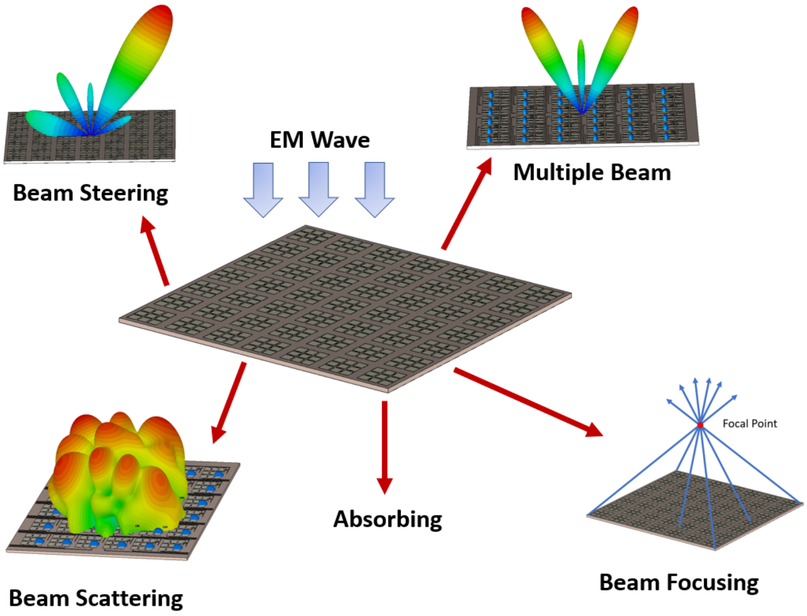

Figure 3.8: The Capabilities of RIS

must be a progressive phase shift between elements. The examples in Section 3.1 explains how the progressive phase shifts on the surface steer the beam to desired directions. Additionally, that section explains how to adjust the phase distribution for different scenarios, such as different angles of incident waves.

- **Multi beam Generation:** Multiple beam generation has a usage similar to beam steering. It can be used to create multiple LoS paths to overcome blockages or to steer the beam towards multiple users. The required phase distribution varies depending on the request. For example, to generate two beams at symmetrical directions, two different symmetrical phase distributions should be created. From the left end to the middle, the phase distribution is adjusted to steer the beam in the desired direction; from the middle to the right end, symmetrical phases are generated. These symmetrical phases create a beam in a symmetrical direction. In Figure 3.9, the phase distribution for generating two beams directed at 30 and -30 degrees is shown. A 1-bit configuration is used for this generation because the surface incorporates a PIN diode. The RIS with a PIN diode will be further explained in Section 3.4.

  Another example for multiple beam generation is creating four different beams.

To create four different beams that are symmetrical to each other from the origin, a similar symmetrical phase distribution should be generated on the surface. This is achieved by mirroring the phase distributions symmetrically from left to middle and from middle to right, as well as from bottom to middle and from middle to top. This phase distribution is also known as checkerboard [47]. Figure 3.10 illustrates the generation of four beams directed to the coordinates (θ, ϕ) = (30°,30°),(-30°,30°),(30°,-30°),(-30°,-30°).

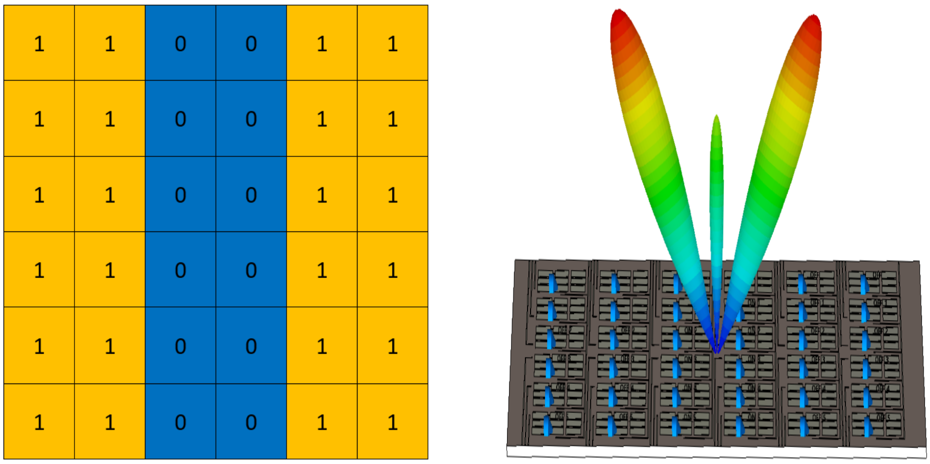

1	1	0	0	1	1
1	1	0	0	1	1
1	1	0	0	1	1
1	1	0	0	1	1
1	1	0	0	1	1
1	1	0	0	1	1

(a) Phase distribution for 2 beam generation

(b) 3D simulations of 2 beam phase distribution

Figure 3.9: 2 Beam Generation

- **Beam Scattering:** Beam scattering is reflecting the incident wave to various directions. This capability is beneficial when there are numerous users and the computational cost to track these users and create multiple beams that focus on each of them is high [44]. An illustrative example of beam scattering is shown in Figure 3.11. The phase of the surface must be randomly distributed to achieve good beam scattering. Every cell in the example is 2λ, and the phase distribution on the surface alternates between 1 and 0 in both the x and y directions, causing the incident wave to be scattered [48].

- **Nearfield Beam Focusing:** Beam focusing is another significant capability of RIS. It is well-known that as the size of the surface increases, the nearfield region also expands proportionally to the square of its size. Therefore, when a

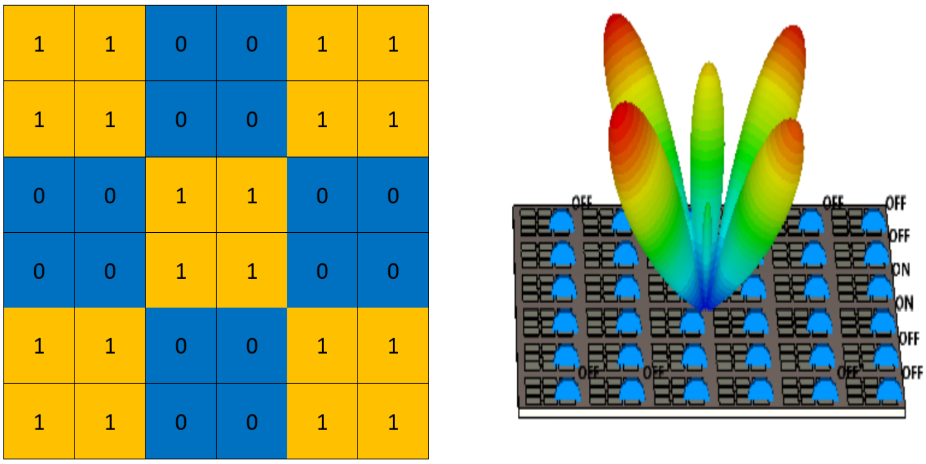

1	1	0	0	1	1
1	1	0	0	1	1
0	0	1	1	0	0
0	0	1	1	0	0
1	1	0	0	1	1
1	1	0	0	1	1

(a) Phase distribution for 4 beam generation

(b) 3D simulations of 4 beam phase distribution

Figure 3.10: 4 Beam Generation

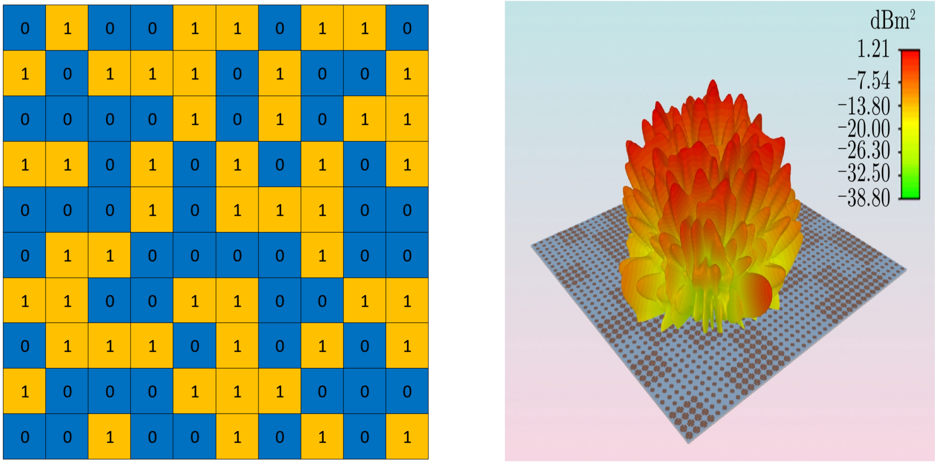

0	1	0	0	1	1	0	1	1	0
1	0	1	1	1	0	1	0	0	1
0	0	0	0	1	0	1	0	1	1
1	1	0	1	0	1	0	1	0	1
0	0	0	1	0	1	1	1	0	0
0	1	1	0	0	0	0	1	0	0
1	1	0	0	1	1	0	0	1	1
0	1	1	1	0	1	0	1	0	1
1	0	0	0	1	1	1	0	0	0
0	0	1	0	0	1	0	1	0	1

(a) Phase distribution for scattering

(b) 3D simulations of scatter phase distribution

Figure 3.11: Scattering [48]

large RIS is used, nearfield beam focusing should be employed. This property would be particularly beneficial, for example, if an RIS is mounted on a building, as its nearfield region would extend far enough that users would be located within this nearfield region.

A parabolic antenna focuses the incoming beam at its focal point. Reflectarrays mimic this property by adjusting the phase distribution so that the phase distribution of the reflectarray matches the phase of the parabolic antenna at the virtual flat surface. This relation between reflectarray and parabolic antennas was discussed in Chapter 1 and an illustration for that is shown in Figure 1.2b To achieve beam focusing, the same principle used in reflectarrays should be applied. By doing so, users in the nearfield can be effectively focused. In Figure 3.12 an example of required phase distribution to focus the beam to focal point is given. In the example the height of the local point is 50 mm and it is at the middle of the surface. The size of the surface is 5λ x 5λ which is 150 mm to 150 mm.

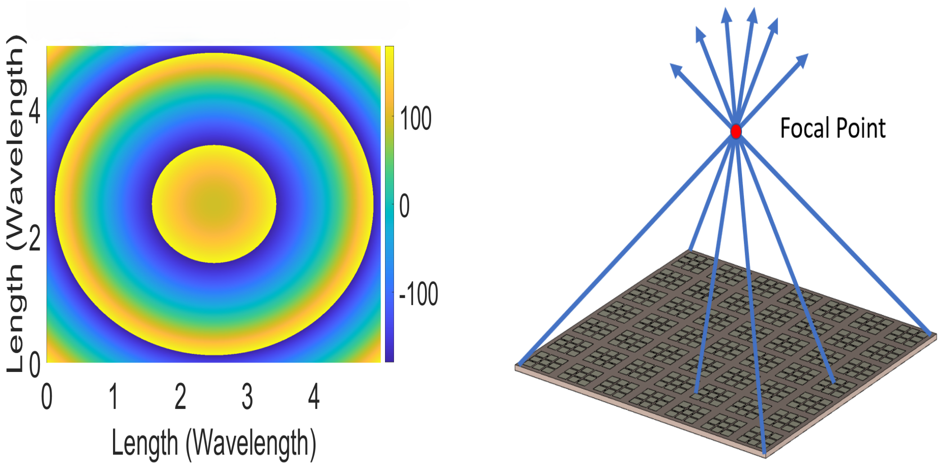

(a) Required phase distribution for beam focusing

(b) Beam focusing illustration

Figure 3.12: Beam Focusing

- **Absorbing:** The last capability is absorbing. In unit cell analysis, some cell variations have a very low reflection coefficient. The reflection coefficient decreases up to -22 dB at 10 GHz. A unit cell analysis of the cell that has a -22 dB reflection coefficient is shown in Figure 3.13. This result means that some variation of the unit cell can be used as an absorber. The absorption capability can be useful for spectral coexistence of radar and communication systems, spectrum sharing in device-to-device communications and for adding extra physical layer security for jammer attacks [49].

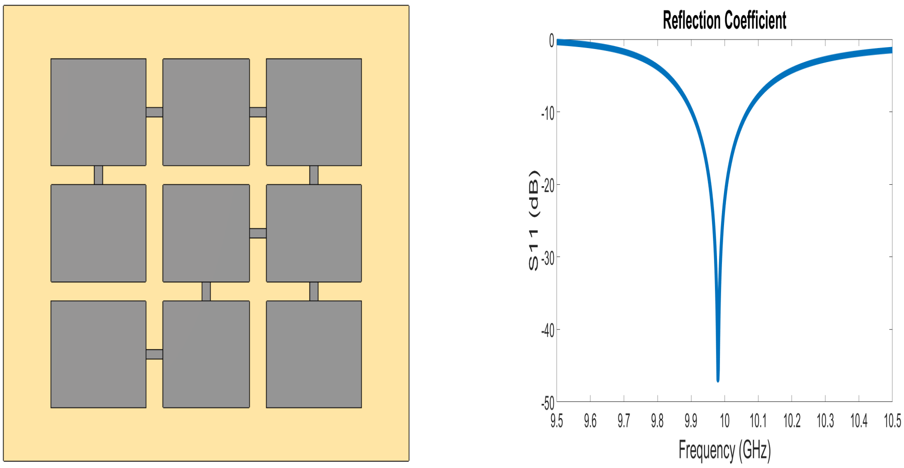

(a) Absorbing unit cell

(b) Reflection Coefficient

Figure 3.13: Reflection coefficient and the model of the absorbing unit cell

In the following section, the beam steering capability of the RIS will be demonstrated. Initially, simulations of an RIS using a 12-bit unit cell will be presented, illustrating the performance of the RIS with high-resolution phase control. After these simulations, an RIS with a 2-bit unit cell will be simulated, and then the results will be discussed, highlighting the performance with lower-resolution phase control. Finally, a comparison between the two configurations will be provided, examining the differences in beam steering and SLL performances.

For the simulations steering angle ranges up to 60 degrees. After 60 degrees, the side lobe level will be higher than the beam in the desired direction. Therefore, it can be concluded that the beam steering limit is 60 degrees for the RIS with a 12-bit unit cell.

3.3 Passive Surface Design

A detailed explanation on how to adjust the phase distributions of the surface was given. In this section we are going to design several examples that manipulate the reflected wave using the unit cell that we designed and promoted in Chapter 2. After the simulations using passive unit cell in Section 3.4 simulations of the surface using pin diode will be conducted.

3.3.1 Beam Steering Using 12 Bit Elements

In this section, the beam steering capability of the RIS with 12-bit unit cell is demonstrated. To simplify the process the unit cell with metal bridges is used in simulations.

To steer the beam, the surface phase distribution is adjusted using the 12-bit unit cell as explained in Chapter 3.1. For the simulations, 10x10 element RIS surfaces are designed with dimensions of $5\lambda \times 5\lambda$. The simulations are conducted using FDTD method in CST. The incident wave is a normal incidence plane wave therefore there will be no spatial delay on the surface. For the boundaries, Perfectly Matched Layer (PML) boundaries are used, and the spacing between the surface and the boundaries is set to 15 mm. The simulation results are presented as bistatic radar cross section (RCS) . Two examples of the RCS results for surfaces that steer the beam to 30 and 60 degrees are shown in Figure 3.14. These 3D RCS results indicate that the surfaces steer the beam, although the specific direction cannot be precisely determined. The maximum RCS value for the 30-degree surface is higher than that for the 60-degree surface, which is expected. As the steering angle increases, the maximum RCS value decreases because the array factor will have a larger beamwidth at larger angles, resulting in decreased directivity. After investigating the 3D RCS results of two different surfaces, further information about the performance of the surfaces can be obtained by examining the RCS results on the ϕ = 0 degree plane. These results are shown in Figure 3.15 and Figure 3.16. The RCS results of the surfaces that steer the beam from 10 to 70 degrees are presented in the figure. Compared to the 3D RCS results, the information about the side lobe level (SLL) and main lobe direction is much clearer in this figure. It was observed that for steering angles up to 60 degrees, the main lobe direction consistently aligns with the desired angle. However, as highlighted earlier, the RCS values at the main lobe decrease as the steering angle increases. Additionally, at a 70-degree steering angle, the RCS value at 0 degrees is higher than at 70 degrees, indicating that the surface was unable to properly steer the beam to 70 degrees.

Following the presentation of the simulation results, observations are summarized in Tables 3.1 and 3.2. This table details the SLL values and the directions of the main beam at various frequencies.

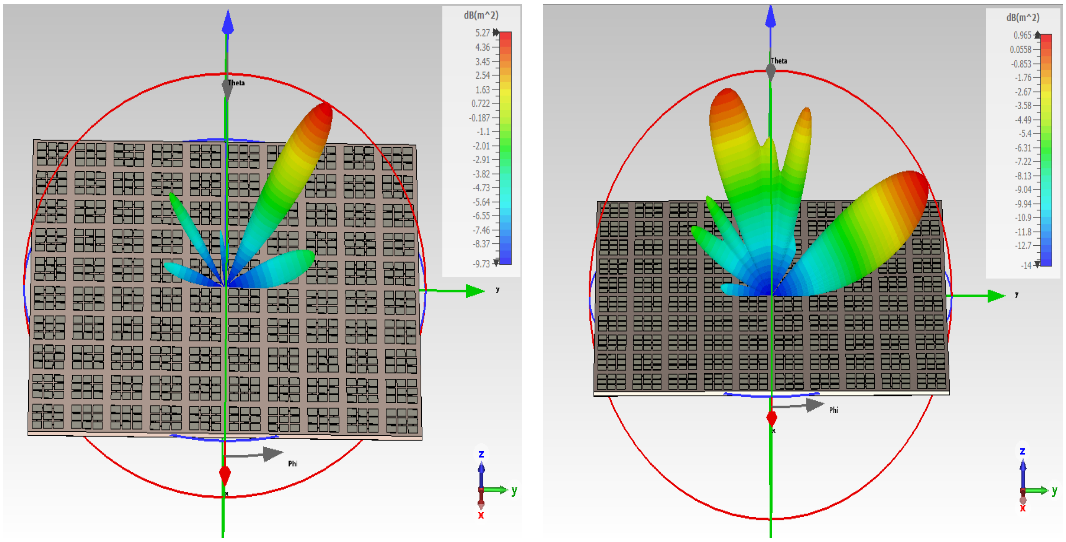

(a) Main Lobe 30 Degree

(b) Main Lobe 60 Degree

Figure 3.14: 3D RCS results of the beam steering surfaces using 12 bit unit cell

The frequencies analyzed include:

- $f_{min(mainbeam)}$**:** The minimum frequency at which the RCS value is highest within a 2-degree error of the desired direction.
- $f_{max(mainbeam)}$**:** The maximum frequency at which the RCS value is highest within a 2-degree error of the desired direction.
- f_{best}**:** The frequency at which the SLL is at its lowest.
- $f_{min(SLL)}$**:** The minimum frequency at which the SLL is greater than -3 dB below the best SLL.
- $f_{max(SLL)}$**:** The maximum frequency at which the SLL is greater than -3 dB below the best SLL.
- *10 GHz:* The target frequency.

This table is very useful for comparing the performance of the RIS at different frequencies and for understanding the operational limits of the RIS. The first observation

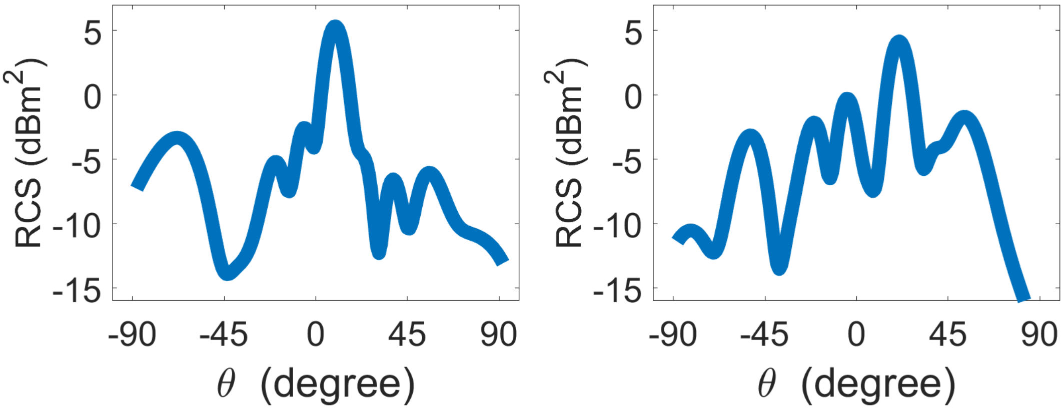

(a) Steering to 10 Degree (b) Steering to 20 Degree

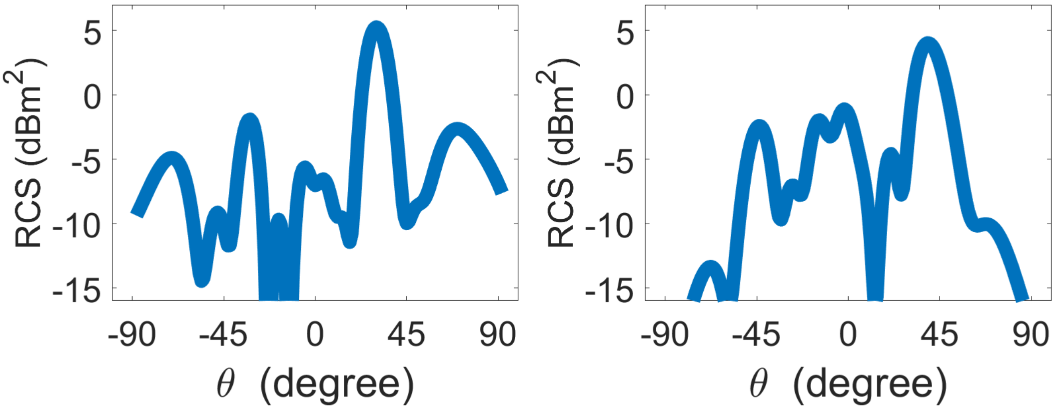

(c) Steering to 30 Degree (d) Steering to 40 Degree

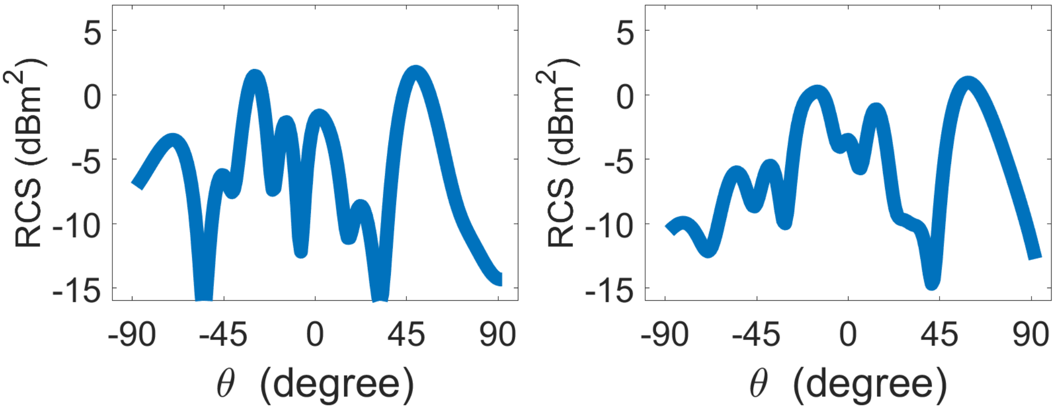

(e) Steering to 50 Degree (f) Steering to 60 Degree

Figure 3.15: RCS results of the surfaces designed using 12 bit unit cell

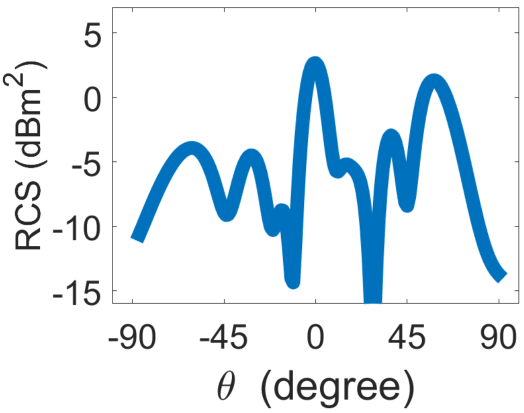

Figure 3.16: Beam steering simulation of the surface that steers the beam to 70 degree using 12 bit unit cell

that can be made from this table is that the SLL is the most volatile parameter with frequency changes. In contrast, the main lobe direction is more stable across the frequency range. For example, for the 20-degree steering surfaces, the SLL varies from -7.2 to -0.2 dB between 9.9 and 10.15 GHz, and from -7.2 to -0.1 dB between 9.9 and 9.6 GHz, while the main lobe direction remains within the 20-22 degree range. This volatility in SLL can be attributed to the fact that some unit cell states have narrower bandwidths than others. As discussed in Chapter 2, phase responses between -100 and 100 degrees change more rapidly with frequency than those close to 180 or -180 degrees. As the frequency varies, the phase error of the narrow-bandwidth unit cells increases. However, when considering the overall array, the beam is still steered to the desired angle. Despite this, the increased phase error in some cells reduces the power directed towards the desired angle, leading to a rise in SLL levels.

For the surfaces 2 different bandwidth definition can be used for the performance of the surfaces, the first one is to use the main beam direction. In this approach a range of 2 degrees for main beam direction is determined and the bandwidth calculated using this value and the second approach is to use SLL levels. In this approach the frequency which has the minimum SLL value will be determined and the frequencies that the SLL values drop by 3 dB. This 3 dB frequency band can be determined as a bandwidth.

In this study the lower bandwidth will be used because for some surfaces the bottleneck is the SLL and for some it is the maintaining a main lobe direction. For 10,50 and 60 degree steering surfaces the main lobe direction is the bottleneck and their bandwidths are 4%, 3% and 4.5%. For 20-30-40 degree surfaces the bottleneck is SLL and their bandwidths are 2.5%, 3.5% and 3%.

Table 3.1: Simulation results of the surfaces using 12-bit elements

Desired Steering Angle		Frequency (GHz)	Main Beam Direction	SLL (dB)
10°	$f_{min(mainbeam)}$	9.7	8°	-9
	$f_{min(SLL)}$	-	-	-
	$f_{max(mainbeam)}$	10.1	11°	-7.5
	$f_{max(SLL)}$	-	-	-
	f_{best}	9.75	9°	-10
		10	10°	-8
20°	$f_{min(mainbeam)}$	9.6	20°	-0.1
	$f_{min(SLL)}$	9.75	20°	-4.3
	$f_{max(mainbeam)}$	10.15	22°	-0.2
	$f_{max(SLL)}$	10	21°	-5
	f_{best}	9.9	20°	-7.2
		10	21°	-5
30°	$f_{min(mainbeam)}$	9.65	32°	-0.1
	$f_{min(SLL)}$	9.8	31°	-4.3
	$f_{max(mainbeam)}$	10.2	30°	-1
	$f_{max(SLL)}$	10.15	30°	-5.2
	f_{best}	9.9	30°	-7.5
		10	30°	-7

3.3.2 Beam Steering Using 2 Bit Elements

Following the design of the passive surface using a 12-bit unit cell, a surface utilizing a 2-bit unit cell will be designed to demonstrate the effectiveness of the bit reduction

Table 3.2: Simulation results of the surfaces using 12-bit elements

Desired Steering Angle		Frequency (GHz)	Main Beam Direction	SLL (dB)
40°	$f_{min(mainbeam)}$	9.6	40°	-0.1
	$f_{min(SLL)}$	9.7	10°	-5.6
	$f_{max(mainbeam)}$	10	38°	-5
	$f_{max(SLL)}$	10.1	10°	-0.2
	f_{best}	9.8	39°	-7.2
		10	39°	-5
50°	$f_{min(mainbeam)}$	9.75	51°	-2.5
	$f_{min(SLL)}$	-	-	-
	$f_{max(mainbeam)}$	10.05	50°	-0.1
	$f_{max(SLL)}$	-	-	-
	f_{best}	9.8	50°	-2.8
		10	50°	-0.5
60°	$f_{min(mainbeam)}$	9.65	58°	-0.2
	$f_{min(SLL)}$	-	-	-
	$f_{max(mainbeam)}$	10.1	58°	-0.1
	$f_{max(SLL)}$	-	-	-
	f_{best}	9.8	59°	-2.5
		10	58°	-0.7

method for this unit cell. The same element described in Chapter 2.2 is used for the 2-bit configuration, as illustrated in Figure 3.17. The active elements are shown in red, while the stable bridges are depicted in gray. By altering only the red connections, the required phase shifts can be achieved. The phases of different states are presented in Figure 3.18. Using these states, surfaces that steer the beam in various directions will be designed.

For this design, 10×10 elements surface is considered to allow comparison with 12-bit case. This comparison will help to show the differences in performance and validate the feasibility of using a reduced bit configuration while maintaining acceptable

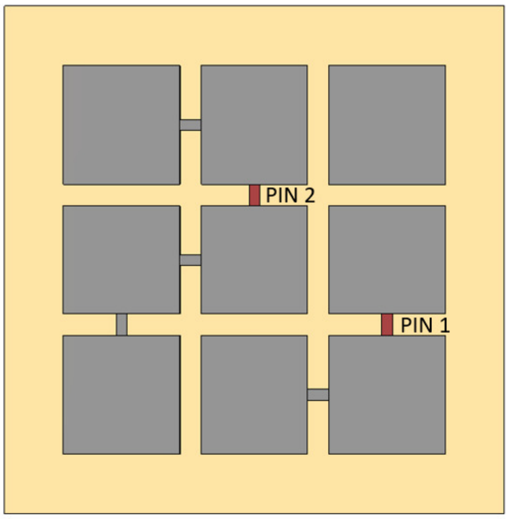

Figure 3.17: Proposed 2 bit unit cell

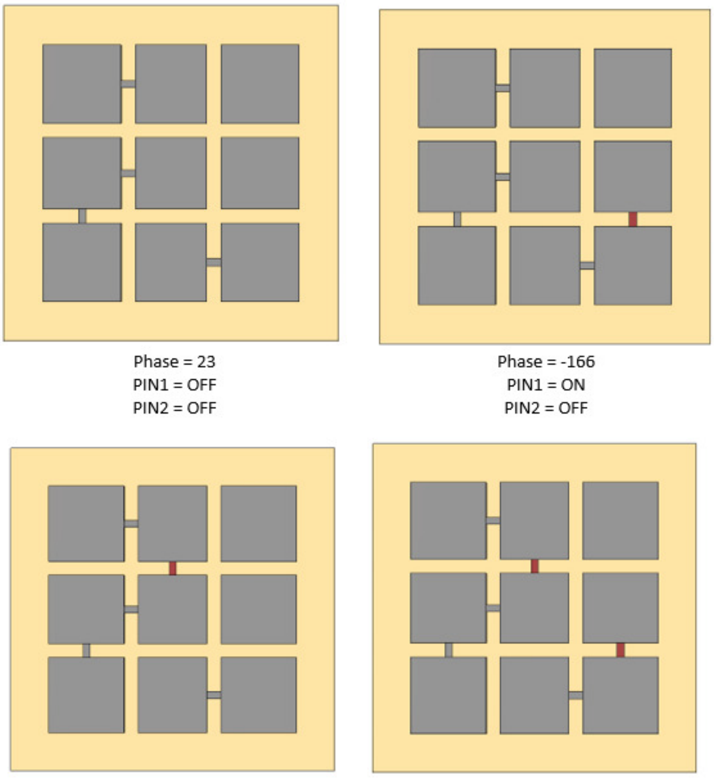

Phase = 23
PIN1 = OFF
PIN2 = OFF

Phase = -166
PIN1 = ON
PIN2 = OFF

Phase = -83
PIN1 = OFF
PIN2 = ON

Phase = 114
PIN1 = ON
PIN2 = ON

Figure 3.18: Phases responses at 10 GHz of different states of the 2 bit unit cell.

beam steering capabilities. In the simulations, surfaces designed to steer the beam from 10 to 60 degrees in 10-degree increments were created using the four states of the 2-bit unit cell. The required states for the unit cells on each surface are detailed in Table 3.3. Calculations were performed for normal incidence, and it is observed that as the steering angle increases, the phase shift between consecutive elements also increases. Following the design of the surfaces using the 2-bit element, simulations were conducted. The 3D RCS results of two different surfaces are shown in Figure 3.19 while the 2D RCS results of all surfaces are presented in Figure 3.20. The 3D results are shown for 20 and 40-degree steering angles, with better SLL performance observed at the 20-degree steering angle. While the 3D RCS results confirm successful beam steering, a more detailed analysis necessitates examining the 2D RCS results. Initial observations from the 2D results indicate that the SLL performance is worse than the 12-bit unit cell cases, primarily due to the greater phase quantization error associated with the 2-bit unit cell.

Table 3.3: Required states of the unit cells at the surfaces that steers the beam to different directions

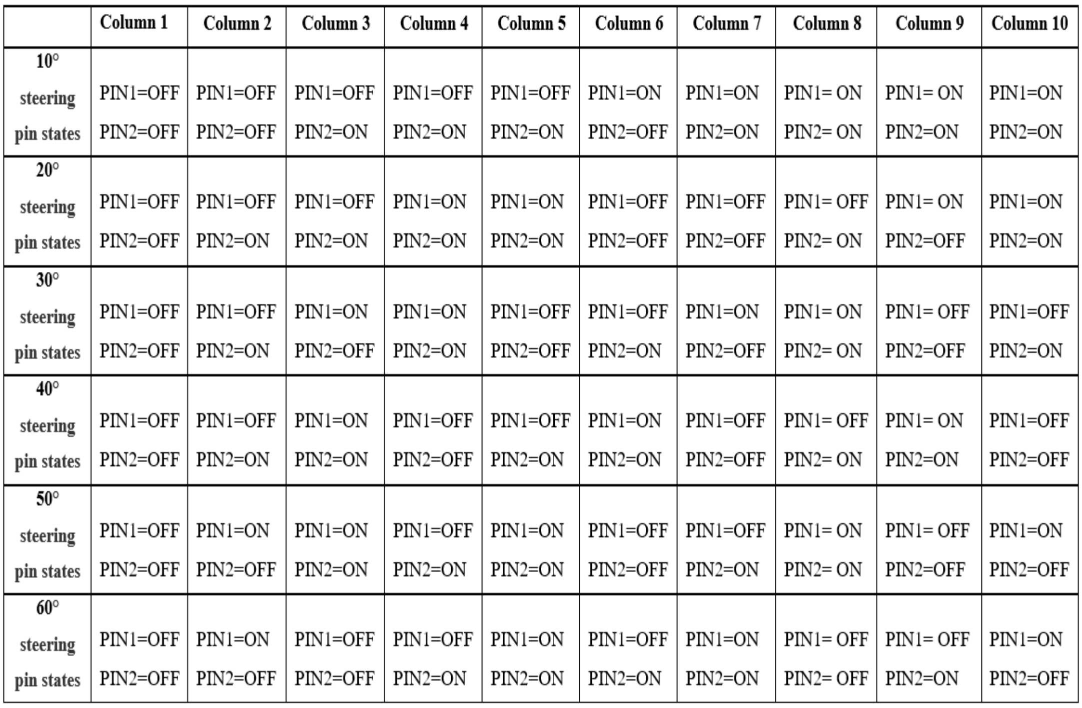

	Column 1	**Column 2**	**Column 3**	**Column 4**	**Column 5**	**Column 6**	**Column 7**	**Column 8**	**Column 9**	**Column 10**
10° steering pin states	PIN1=OFF PIN2=OFF	PIN1=OFF PIN2=OFF	PIN1=OFF PIN2=ON	PIN1=OFF PIN2=ON	PIN1=OFF PIN2=ON	PIN1=ON PIN2=OFF	PIN1=ON PIN2=ON	PIN1= ON PIN2= ON	PIN1= ON PIN2=ON	PIN1=ON PIN2=ON
20° steering pin states	PIN1=OFF PIN2=OFF	PIN1=OFF PIN2=ON	PIN1=OFF PIN2=ON	PIN1=ON PIN2=ON	PIN1=ON PIN2=ON	PIN1=OFF PIN2=OFF	PIN1=OFF PIN2=OFF	PIN1= OFF PIN2= ON	PIN1= ON PIN2=OFF	PIN1=ON PIN2=ON
30° steering pin states	PIN1=OFF PIN2=OFF	PIN1=OFF PIN2=ON	PIN1=ON PIN2=OFF	PIN1=ON PIN2=ON	PIN1=OFF PIN2=OFF	PIN1=OFF PIN2=ON	PIN1=ON PIN2=OFF	PIN1= ON PIN2= ON	PIN1= OFF PIN2=OFF	PIN1=OFF PIN2=ON
40° steering pin states	PIN1=OFF PIN2=OFF	PIN1=OFF PIN2=ON	PIN1=ON PIN2=ON	PIN1=OFF PIN2=OFF	PIN1=OFF PIN2=ON	PIN1=ON PIN2=ON	PIN1=OFF PIN2=OFF	PIN1= OFF PIN2= ON	PIN1= ON PIN2=ON	PIN1=OFF PIN2=OFF
50° steering pin states	PIN1=OFF PIN2=OFF	PIN1=ON PIN2=OFF	PIN1=ON PIN2=ON	PIN1=OFF PIN2=ON	PIN1=ON PIN2=ON	PIN1=OFF PIN2=OFF	PIN1=OFF PIN2=ON	PIN1= ON PIN2= ON	PIN1= OFF PIN2=OFF	PIN1=ON PIN2=OFF
60° steering pin states	PIN1=OFF PIN2=OFF	PIN1=ON PIN2=OFF	PIN1=OFF PIN2=OFF	PIN1=OFF PIN2=ON	PIN1=ON PIN2=ON	PIN1=OFF PIN2=ON	PIN1=ON PIN2=ON	PIN1= OFF PIN2= OFF	PIN1= OFF PIN2=ON	PIN1=ON PIN2=OFF

The performance of the surfaces is summarized in Tables 3.4 and 3.5, where the SLL levels and main lobe directions at different frequencies are presented. These tables

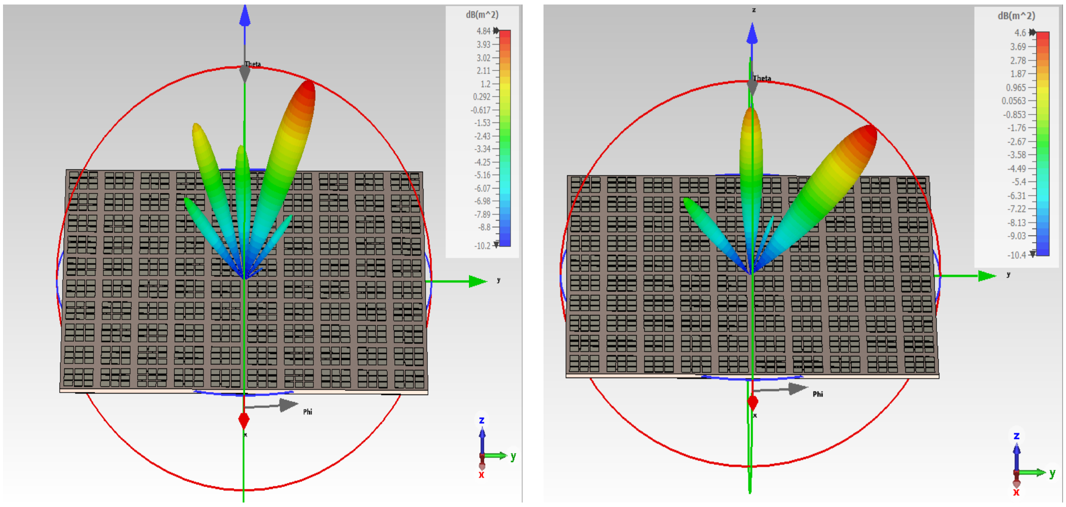

(a) 3D RCS results of the surface that steers the beam to 20 degree

(b) 3D RCS results of the surface that steers the beam to 40 degree

Figure 3.19: 3D RCS result of the surfaces with 2-bit elements

allow for the determination of performance criteria such as bandwidth. When comparing bandwidth, similar performances are observed between the 12-bit and 2-bit unit cells, with the main beam direction error being negligible. This indicates that both configurations are capable of maintaining the beam direction within an acceptable margin. However, the SLL performance of the 2-bit unit cell is notably worse, particularly for surfaces with higher steering angles. The primary reason for this degradation is the higher phase quantization error associated with the 2-bit unit cell.

In Table 3.6, the difference in quantization for a desired steering angle of 30 degrees are shown. The required phase difference between elements is ideally 90 degrees; however, this value cannot be precisely achieved. With 12-bit elements, the phase differences between elements are 94, 89, 89, and 88 degrees. In contrast, with 2-bit elements, these differences are 91, 80, 83, and 106 degrees. This comparison highlights the significantly higher error when using the 2-bit unit cell with the same number of elements. The use of a 2-bit unit cell results in a higher quantization error, which limits the control over the phase distribution, causing higher side lobe levels. These findings of this study explain the bit resolution-performance trade-off in RIS designs, emphasizing an optimal bit resolution for complexity, costs, and performance

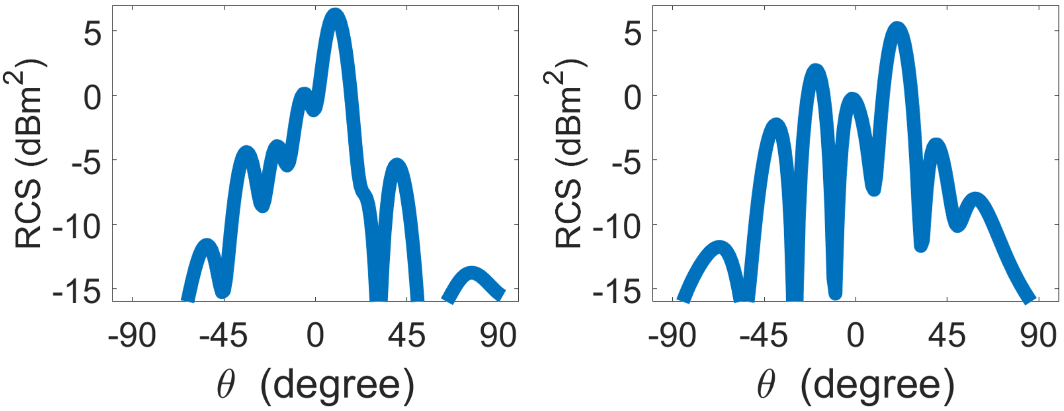

(a) Steering to 10 degree

(b) Steering to 20 degree

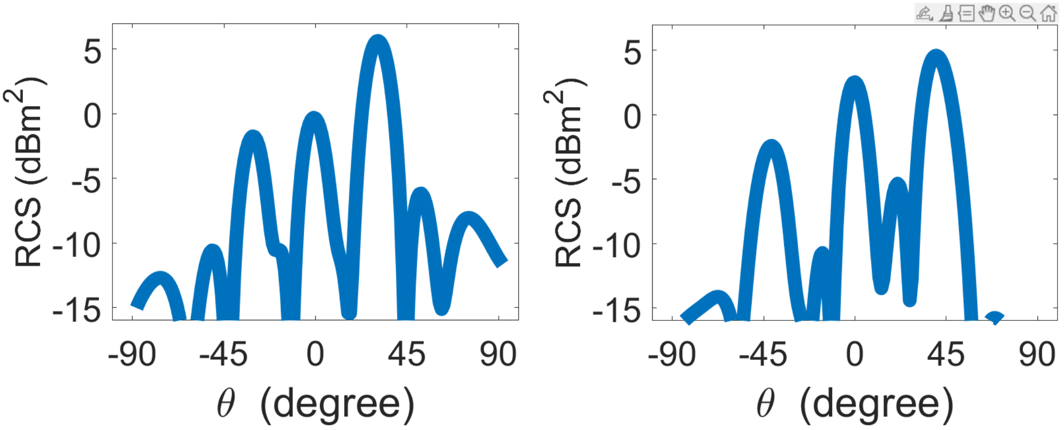

(c) Steering to 30 degree

(d) Steering to 40 degree

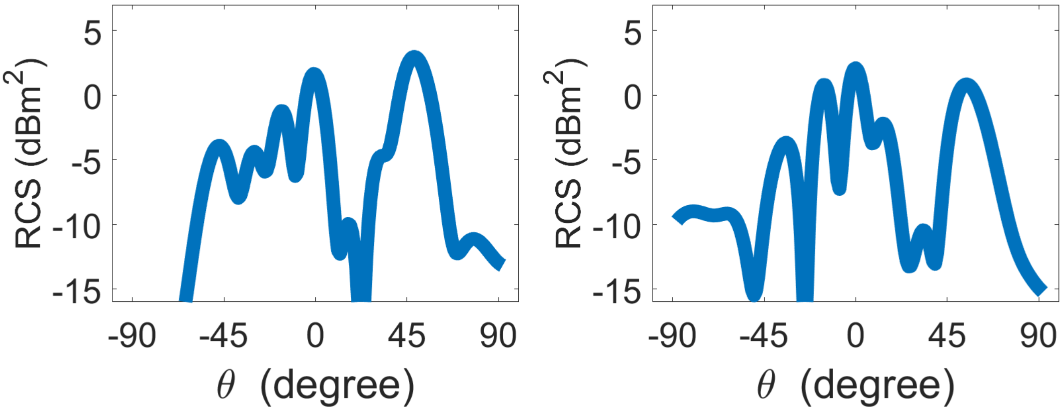

(e) Steering to 50 degree

(f) Steering to 60 degree

Figure 3.20: RCS results of the surfaces designed with 2 bit unit cell

to be chosen.

Table 3.4: Simulation results of the 10×10 surfaces using 2-bit elements

Desired Steering Angle		Frequency (GHz)	Main Beam Direction	SLL (dB)
10°	$f_{min(mainbeam)}$	-9.75	9°	-12
	$f_{min(SLL)}$	-	-	-
	$f_{max(mainbeam)}$	10.15	11°	-1
	$f_{max(SLL)}$	-	-	-
	f_{best}	9.75	9°	-12
		10	11°	-6
20°	$f_{min(mainbeam)}$	9.75	19°	-0.5
	$f_{min(SLL)}$	9.8	20°	-2.3
	$f_{max(mainbeam)}$	10.15	21°	-0.4
	$f_{max(SLL)}$	10.05	20°	-2.4
	f_{best}	9.9	20°	-5.5
		10	20°	-3.5
30°	$f_{min(mainbeam)}$	9.7	30°	-2.5
	$f_{min(SLL)}$	9.7	30°	-2.5
	$f_{max(mainbeam)}$	10.2	30°	-0.7
	$f_{max(SLL}$	10.1	29°	-2.7
	f_{best}	9.8	30°	-5
		10	29°	-3

3.3.2.1 Beam Steering with Larger Surfaces

Previously, 10×10 element RIS structures were designed using 12-bit and 2-bit unit cells and analyzed through simulations. To further investigate performance, a larger RIS will be simulated. In RIS design, the phase response of the unit cells at the edge is expected to deviate more than the unit cells inside the RIS. This is because unit cells at the edge have fewer neighboring elements, resulting in less coupling between the neighboring elements, which affects the surface current and causes the phase response to differ from the Floquet simulations. For larger arrays, the proportion of edge unit

Table 3.5: Simulation results of the 10×10 surfaces using 2-bit elements

Desired Steering Angle		Frequency (GHz)	Main Beam Direction	SLL (dB)
40°	$f_{min(mainbeam)}$	9.6	40°	-0.5
	$f_{min(SLL)}$	9.7	40°	-3
	$f_{max(mainbeam)}$	10.05	40°	-0.5
	$f_{max(SLL)}$	10	32°	-2
	f_{best}	9.8	40°	-5
		10	40°	-2
50°	$f_{min(mainbeam)}$	9.7	51°	-0.2
	$f_{min(SLL)}$	9.75	50°	-3.1
	$f_{max(mainbeam)}$	10.05	50°	-1
	$f_{min(SLL)}$	9.95	32°	-3
	f_{best}	9.9	50°	-5
		10	50°	-1.5
60°	$f_{min(mainbeam)}$	9.75	58°	-1
	$f_{min(SLL)}$	-	-	-
	$f_{max(mainbeam)}$	9.9	56°	-2
	$f_{max(SLL)}$	-	-	-
	f_{best}	9.9	56°	-2
		10	55°	1.1

Table 3.6: Required and realized phases for 30 degree steering

Required Phase	0°	-90°	180°	90°
Realized Phase (12-bit)	3°	-91°	180°	91°
Realized Phase (2-bit)	23°	114°	-166°	-83°

cells is smaller than in smaller arrays. Therefore, this phenomenon is expected to influence the results less in these simulations. Additionally, for larger arrays, the phase error of individual elements becomes less significant. As the array size increases, the need for precision in phase realization decreases, making even 1-bit configurations sufficient for large arrays [29], [30].

The CST model and 3D RCS results of the surface that steers the beam to 20 degrees are shown in Figure 3.21. To design the surface a 2-bit frozen unit cell was used, allowing for performance comparison. The surface consists of 28x20 elements, with dimensions of $14\lambda \times 10\lambda$. In this simulation, the incident field is normal incidence, and the reflected beam is steered to 20 degrees. The first notable observation is that the directivity of the surface increased, which was expected as directivity is proportional to the aperture area. The maximum RCS of the surface is 20.3 dB(m^2), significantly higher than the maximum RCS of the 10×10 surface simulations which is 4.8 dB(m^2). Simulations with the larger surface were also conducted for 30 and 40 degrees, the RCS results of all three simulations are shown in Figure 3.22. In these simulations, the setup remains the same: the incident field is normal incidence, and the reflected beams are steered to 20, 30, and 40 degrees. The normalized RCS results at the ϕ = 0 plane for both 10×10 and 28×20 element RIS are presented in Figure 3.23. As expected, the beam becomes narrower and the SLL levels decrease for larger arrays.

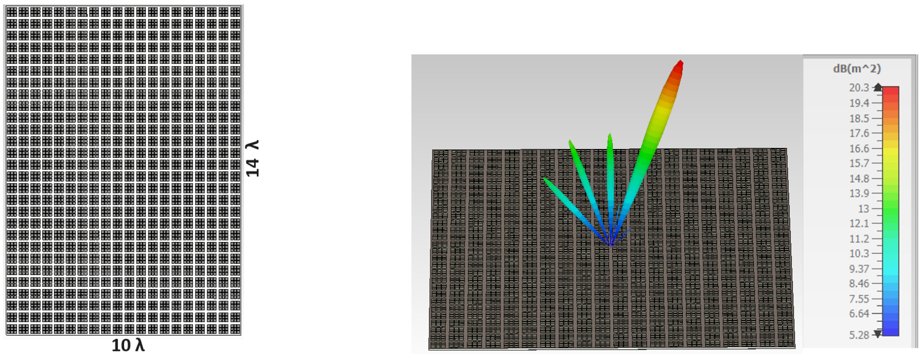

(a) CST model of the larger surface

(b) 3D RCS results of the larger array

Figure 3.21: CST model and 3D simulation result of a 28×20 element surface that steers the beam to 20 degree.

The RCS results of the simulations of the larger surfaces are listed in Table 3.7. As observed in the 20-degree simulations, the directivity increases compared to smaller surfaces due to the larger aperture. Additionally, the directivity of the reflected fields decreases as the steering angle increases, as expected. Finally, the best SLL levels are

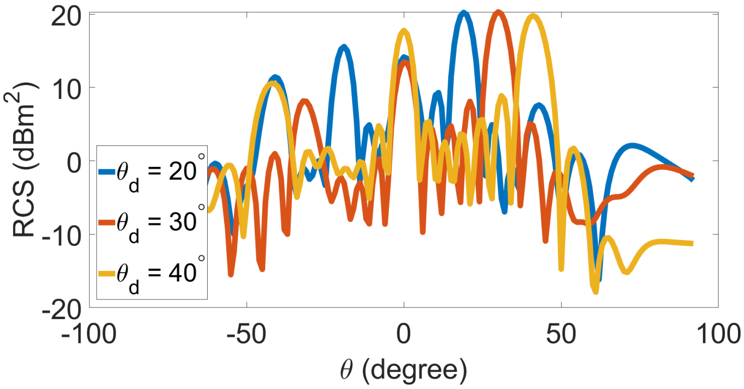

Figure 3.22: The RCS results at ϕ = 0 for 28×20 elements RIS that steers the beam to 20, 30 and 40 degrees.

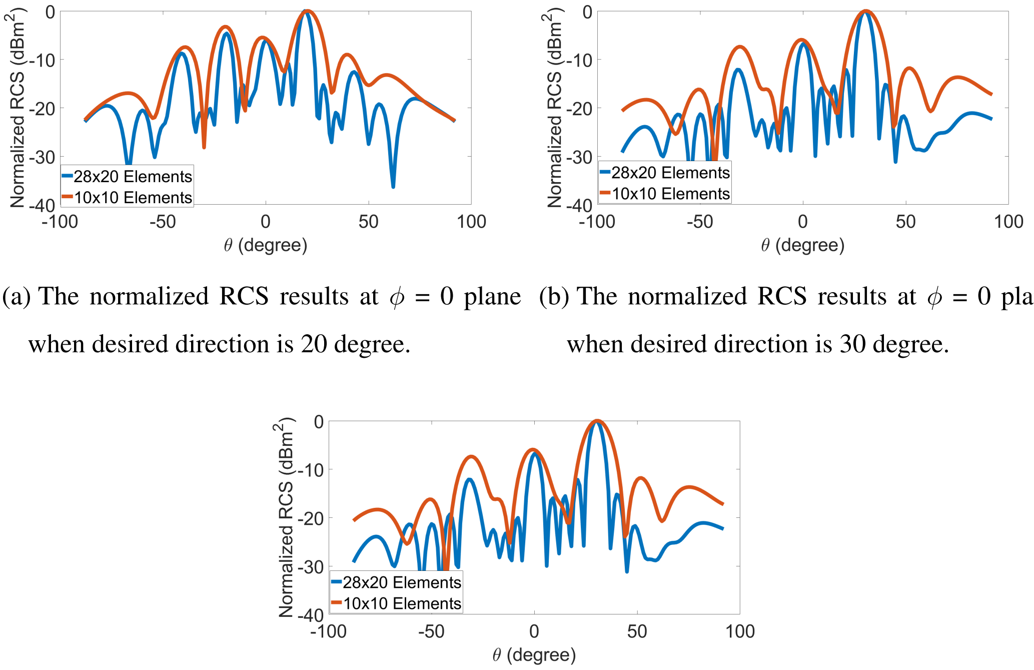

(a) The normalized RCS results at ϕ = 0 plane when desired direction is 20 degree.

(b) The normalized RCS results at ϕ = 0 plane when desired direction is 30 degree.

(c) The normalized RCS results at ϕ = 0 plane when desired direction is 40 degree.

Figure 3.23: The comparison of RCS results of 10×10 and 28×20 elements RIS

improved by 0.5 to 2 dB compared to the 10×10 RIS surfaces. This improvement is attributed to the larger arrays having a smaller proportion of edge unit cells, resulting in fewer elements deviating from their desired phase responses.

Table 3.7: Simulation results of the 28×20 element RIS with 2-bit elements

Desired Steering Angle		Frequency (GHz)	Main Beam Direction	SLL (dB)
20°	$f_{min(mainbeam)}$	9.7	20°	-0.1
	$f_{min(SLL)}$	9.8	20°	-2.9
	$f_{max(mainbeam)}$	10.2	19°	-0.3
	$f_{max(SLL)}$	10.1	19°	-3.2
	f_{best}	9.9	19°	-6
		10	19°	-5.1
30°	$f_{min(mainbeam)}$	9.6	30°	-0.1
	$f_{min(SLL)}$	9.75	30°	-4.2
	$f_{max(mainbeam)}$	10.15	32°	-0.3
	$f_{max(SLL)}$	10.1	32°	-3.9
	f_{best}	9.9	30°	-7
		10	30°	-5.5
40°	$f_{min(mainbeam)}$	9.6	32°	-0.1
	$f_{min(SLL)}$	9.7	32°	-3.3
	$f_{max(mainbeam)}$	10.05	32°	-0.4
	$f_{max(SLL)}$	9.95	32°	-4.5
	f_{best}	9.85	30°	-6.2
		10	30°	-2.3

3.3.3 Performance Analysis for the Error on the Incident Wave

In previous sections, the performance of the surfaces under normal incidence was investigated. However, in real-life applications, the direction of arrival (DoA) cannot be calculated precisely, leading to discrepancies between the actual incidence angle and the calculated one. In this section, the effect of this discrepancy will be investigated. To study this effect, we will use the surface designed to steer the beam to 30 degrees using a 12-bit unit cell. The performance of this surface was previously examined, where the main beam was successfully steered to 30 degrees and the SLL was -7.5

dB.

In the simulation setup, the incidence angle was varied across -10, -5, -2, -1, 0, 1, 2, 5, and 10 degrees to observe the effect of miscalculation of the incidence angle. The obtained RCS patterns are presented in Figure 3.24. Since there are nine different simulations, the results are shown in two separate figures: Figure 3.24a displays the results for positive and 0-degree incidence angles, while Figure 3.24b shows the results for negative and 0-degree incidence angles. The main observation from the results is that the main beam direction shifts with the incidence angle. If the incidence angle is negative, the main beam shifts in the positive direction, i.e. reflected field deviates from the desired angle in the increasing θ direction and if it is positive, the main beam shifts in the negative direction. When the incident wave is normal, there is no spatial delay on the surface. However, when the incidence angle deviates from zero, a progressive phase shift is introduced on the surface due to the spatial delay created by the incident wave. This additional progressive phase shift alters the main beam direction of the reflected beam.

To conclude, the main beam direction changes by approximately the same amount as the change in the incident angle. This effect should be considered when using RIS in real-time applications. When low directivity is sufficient, this effect can be neglected because minor errors in the incident angle calculations will alter the main lobe direction, but the desired direction will still be within the 3 dB bandwidth. However, for high directivity pattern applications, this change in the main lobe direction is critical because the desired direction might not fall within the main lobe due to its narrow width. Therefore, this effect should be especially considered for high directivity applications.

3.3.4 RIS Design for Oblique Incidence

All the examples are for normal incidence in previous sections. After the normal incidence simulations, we will show that the same design principle can be applied when the incident wave is oblique, not normal. As explained in Chapter 3.1, the spatial delay changes at different locations of the surface when the incident wave is coming at an angle. Hence the effect of this must be considered to suitably adjust the surface

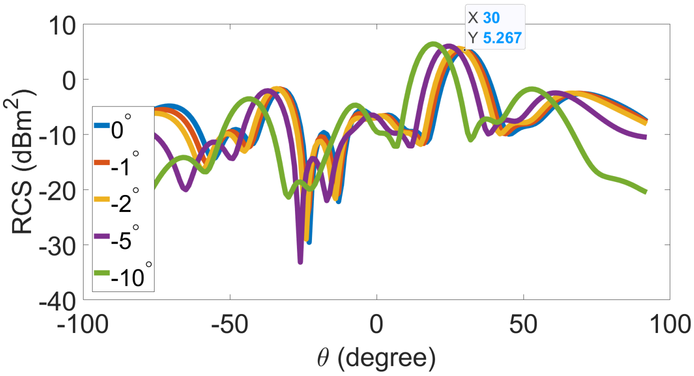

(a) The RCS results when the incident angle is positive or 0.

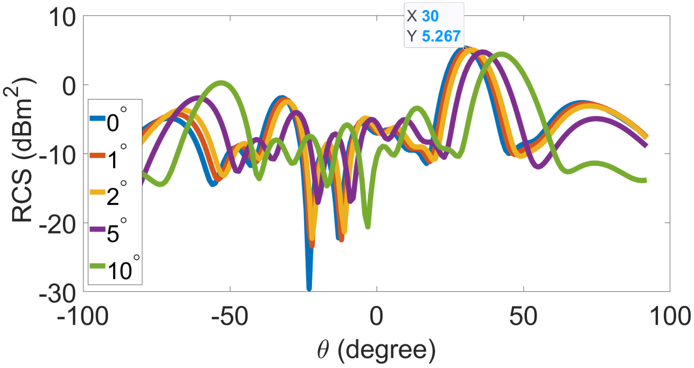

(b) The RCS results when the incident angle is negative or 0.

Figure 3.24: Simulation results for the effect of the error on the incident angle calculations

beam distribution. In this section simulations with oblique incidence scenarios will be conducted to ensure the RIS can effectively work on this condition.

The first example involves an incident angle of 30 degrees, with the goal of steering the beam to 0 degrees. Figure 3.25 shows the required phase of the surface elements. Naturally, the required element phases are the same with the required element phases when steering the beam to 30 degrees under normal incidence. This is due to the principle of reciprocity. Due to reciprocity if a surface can steer a beam to x degrees under normal incidence, it reflects a wave arriving from x degrees to the broadside. Therefore, the same phase distribution that steers the beam to 30 degrees under normal incidence, can also be applied to achieve the desired 0 degree steering in case 30 degree incident wave. Figure 3.26 displays the RCS results of the simulations.

The simulations indicated that the surface can be used to redirect the beam direction in oblique incidence scenarios. The other example is given in Figure 3.27. In this example, the arriving angle is 10 degrees and the desired steering direction is 20 degrees.

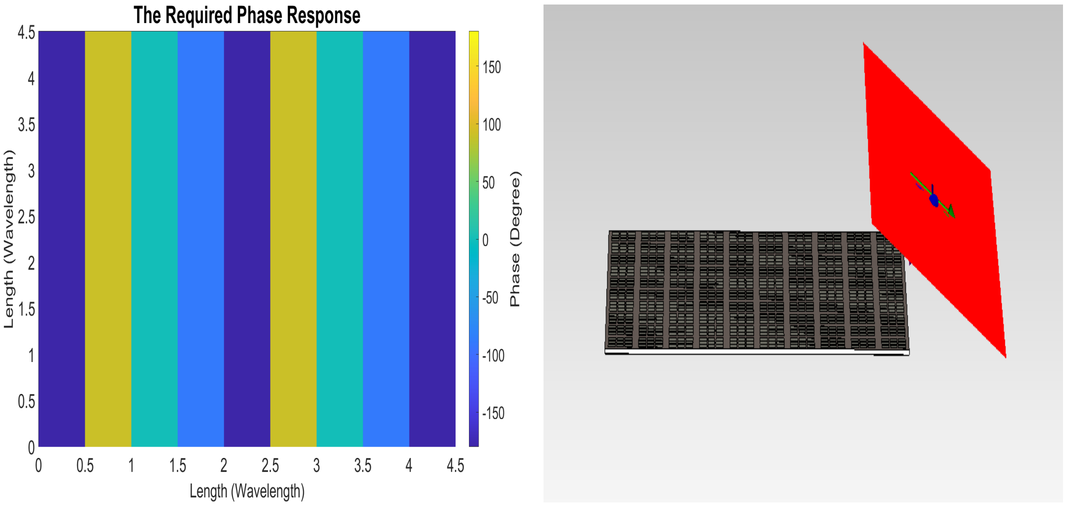

(a) Required phase response for surface elements

(b) 30 degree incident angle

Figure 3.25: Surface that steers the beam to 0 degree when incident angle is 30 degree

After showing that the surface designed with passive unit cells can work under not just the normal incidence but also in oblique incidence, in the next section the surface with active elements will be simulated.

3.4 RIS simulations with PIN Diode

In previous sections, passive unit cells with 2 and 12 bits are used for simulations. For more realistic results simulations of RIS with the PIN diodes will be performed. In Figure 3.28, a 10x10 RIS surface with a 2-bit active unit cell is simulated. The CST model of the surface is shown in the figure. There are 2 PIN diodes defined for each element of the surface, so that there are 200 PIN diodes in total for this simulation. The desired beam steering angle is 30 degrees for normal incidence illumination. The beam is accurately steered to the desired direction. The comparison between the RCS

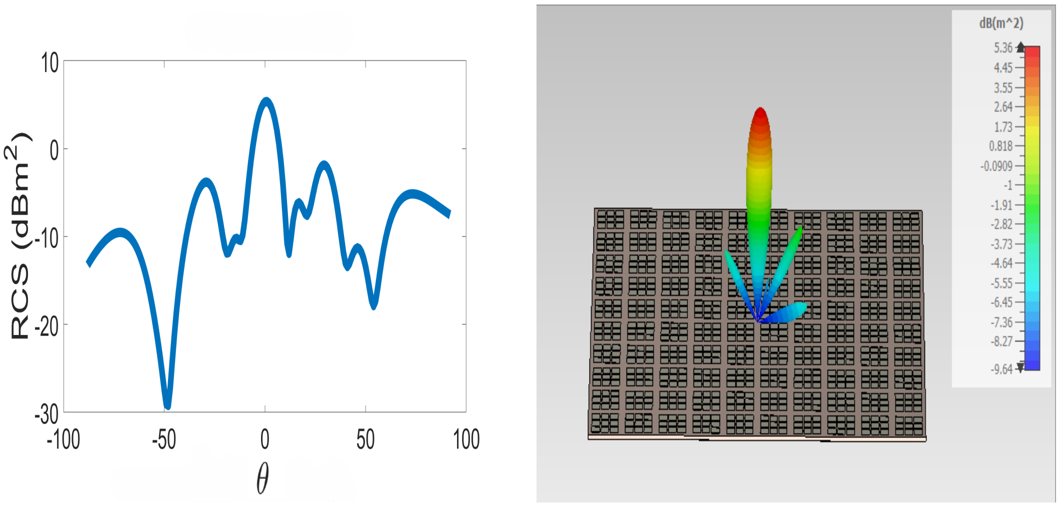

(a) RCS result of the simulation at Phi=0° plane (b) 3D RCS result

Figure 3.26: RCS results of the surface with oblique incidence. Incident angle is 30° and desired reflection direction is 0°

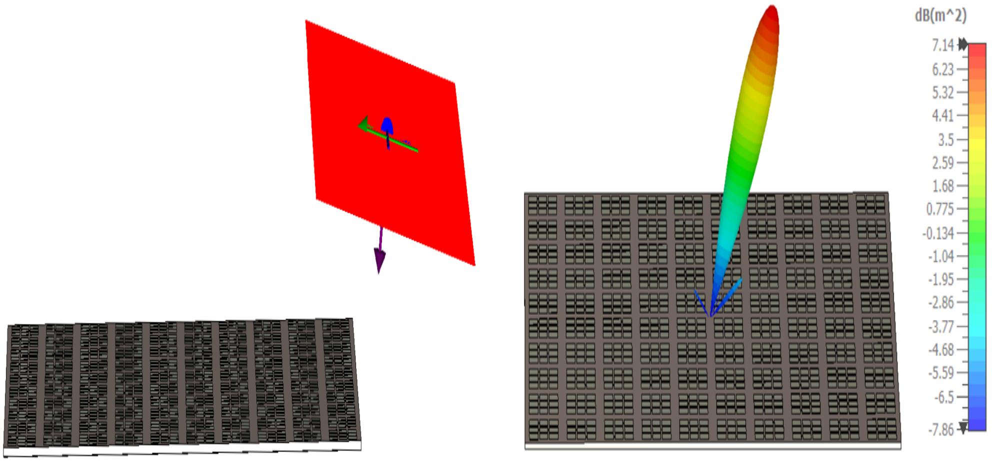

(a) 10 degree incident angle (b) 3D RCS result of the simulation

Figure 3.27: Simulation result of the surface when the incident angle is 10° and the desired steering direction is 20°

results of the frozen RIS and the RIS with PIN diodes is also provided in the figure. The patterns are very similar to each other. The SLL for the active surface is -4.8 dB, compared to -5 dB for the passive surface. This slight degradation in SLL is expected due to the influence of the PIN diodes on the phase response, but it remains minimal, indicating the robustness of the unit cell design.

In the following sections, RIS structures with 1-bit unit cells are examined, with a focus on demonstrating the beam steering capabilities of these surfaces. After these simulations, the next step involves simulating the active surface with integrated bias lines. For these simulations, a 1-bit unit cell will be used because 2-bit or higher configurations would require a two-layered structure, which adds significant complexity to production. These simulations are important to understand the effect of the bias line on the surface performance.

3.4.1 Surface of 1-bit Unit Cell with PIN Diode

In this section, simulations of the RIS with a 1-bit active unit cell are presented. First, RIS with PIN diodes, but without bias lines, are simulated. The simulations are conducted with a 6×6 element RIS surface. Although this particular simulation does not include bias lines, the subsequent simulations will incorporate integrated bias lines. Due to the narrow gap between elements, a 6×6 RIS surface is the largest configuration that can be used without requiring a multilayer setup. To maintain consistency, this simulation was also conducted with a 6×6 element RIS. Given that a 6×6 configuration may be too small for some applications, multiple 6×6 surfaces can be combined to increase the overall surface area.

Surfaces designed using 1-bit elements result in a symmetrical phase distribution for normal incidence beam steering due to the limited precision in quantization. This symmetrical distribution leads to a symmetrical pattern. To address this issue, optimization algorithms, which will be explained in Chapter 3.5, can be employed. The analyzed surface is given in Figure 3.29a and 3D RCS pattern is given in Figure 3.29b. The comparison with the passive RIS are also provided in the figure. As expected, the patterns are very similar. The pattern exhibits symmetrical lobes at 30 and -30 degrees.

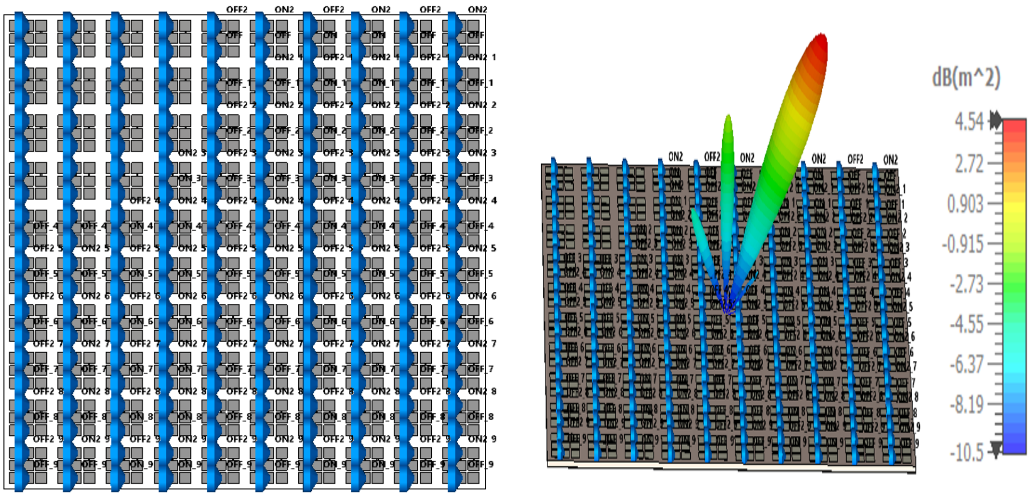

(a) Surface with 2-bit active elements (b) 3D RCS results of the active surface

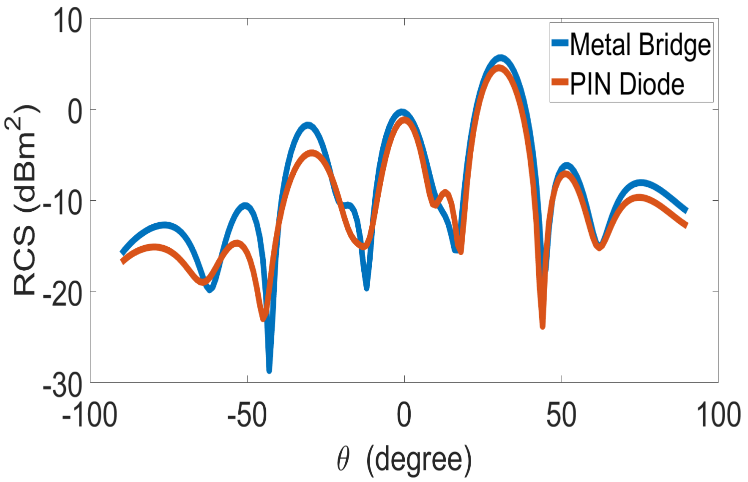

(c) The RCS results of active and frozen surfaces with 2-bit elements

Figure 3.28: Surface with 2-bit active elements and its RCS results

3.4.1.1 1-bit Surface with Bias Line

After validating the 1-bit active RIS, simulations with integrated bias lines were conducted. The bias lines are essential for changing the states of the PIN diodes. To avoid using a multilayer design, the bias lines must be placed on the surface, which may affect performance. Therefore, simulations with integrated bias lines were performed. The RIS with a bias line, a close-up of the RIS model with a bias line, and the RCS results of the simulations are shown in Figure 3.30. The 2 bias lines are placed for ev-

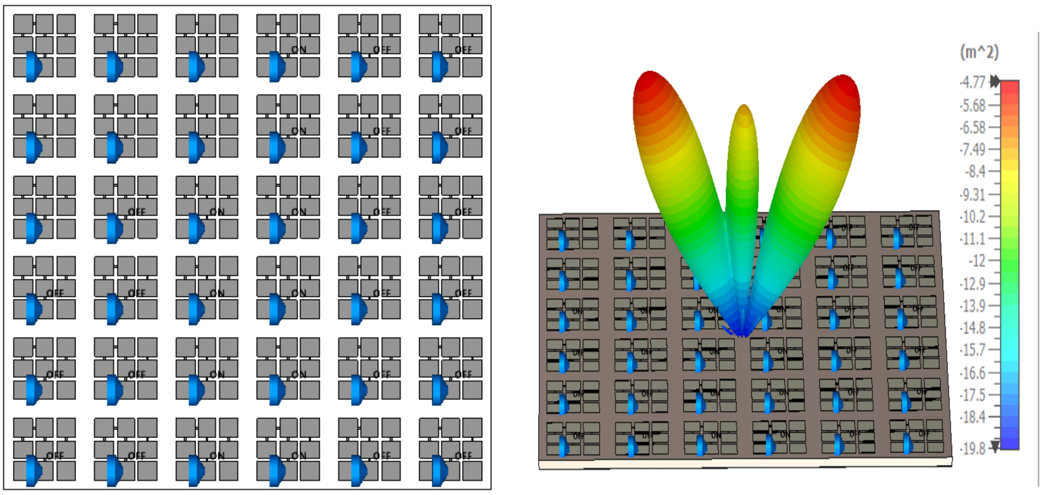

(a) Surface with 1-bit active elements

(b) 3D RCS results of the active surface

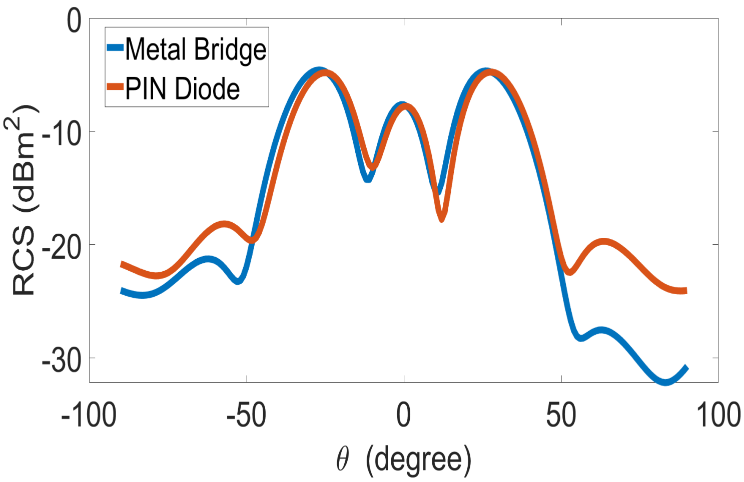

(c) The simulation results of active and frozen surfaces with 1-bit elements

Figure 3.29: Surface with 1-bit active elements and its simulation results

ery PIN diode one is for grounding and the other is for bias voltage. Two simulations are conducted using this 6×6 RIS: one steering the beam to 30 degrees and the other to 10 degrees. In the 10-degree steering case, the pattern is symmetrical as expected and the second SLL is very low due to the smaller steering angle. The 30-degree steering case exhibits a pattern very similar to the case without bias lines. To further investigate the effect of the bias lines, the RCS results of the active surfaces with and without bias lines are shown in Figure 3.31. The patterns are very similar, indicating that the effect of the bias lines is minimal. The bias lines have a very narrow width of

0.25 mm and are perpendicular to the E-field of the incident wave, which minimizes their impact on the surface's performance.

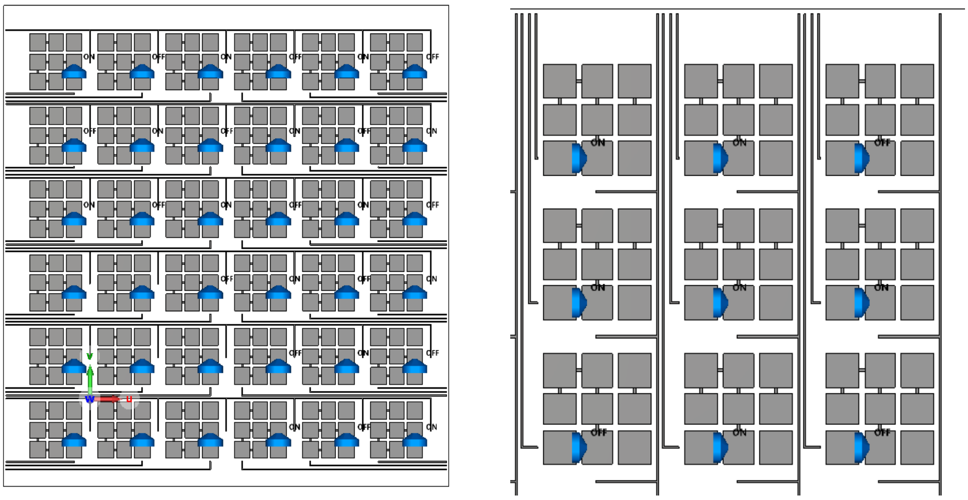

(a) Surface with 1-bit active elements with integrated bias lines

(b) Close-up of a surface with 1-bit active elements and integrated bias line

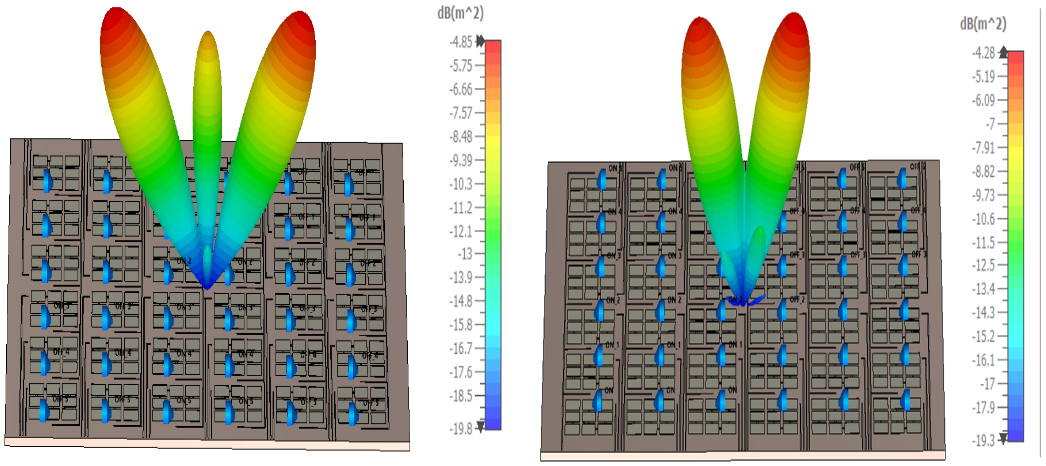

(c) 3D RCS results of the active surface that steers the beam to 30 degree

(d) 3D RCS results of the active surface that steers the beam to 10 degree

Figure 3.30: Surface with 1-bit active elements with a bias line and its RCS results

There are space limitations for bias line implementation due to the small spacing between the elements. Specifically, a maximum of three bias lines can fit between elements, which constrains the RIS size to 6×6. One solution to produce larger active RIS designs is to use a layered structure. However, this approach increases the cost

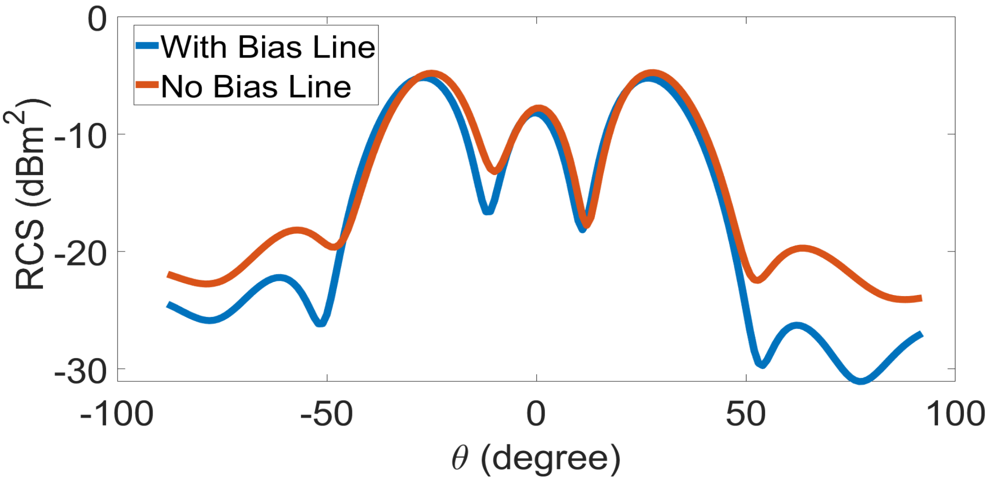

Figure 3.31: RCS results at ϕ = 0 plane of the surfaces with and without integrated bias lines when desired direction is 30 degree

and complexity of production. Another solution is to integrate multiple 6×6 element RIS units, which addresses the size limitations of RIS with bias lines.

For the RIS examples designed in this thesis work, an alternative solution is column-by-column biasing, where all elements in a column share the same state. This approach overcomes the space restrictions, simplifies the design, and reduces costs. However, it also introduces some limitations on the control of the phase distribution because phase manipulation is only possible along one axis. In conclusion, the trade-off for the biasing strategy requires careful consideration. The choice between a layered structure, using multiple 6×6 RIS units, and column-by-column biasing depends on application requirements, cost, and desired RIS capabilities.

In Figure 3.32a, a column-biased RIS configuration is illustrated. This example features a 10x10 element surface, with each column incorporating two bias lines: one for grounding and the other for biasing. The RCS results for this RIS configuration are presented in Figure 3.32c. The simulation demonstrates that the beam is successfully steered to 30 degrees using this column-biased approach.

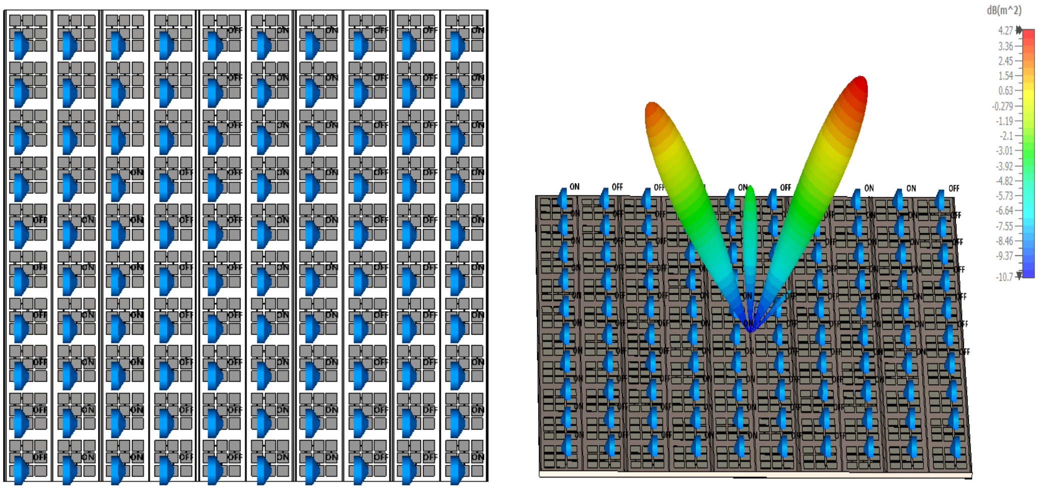

(a) Surface with a 1-bit active unit cell and a bias line

(b) 3D RCS results of the active surface

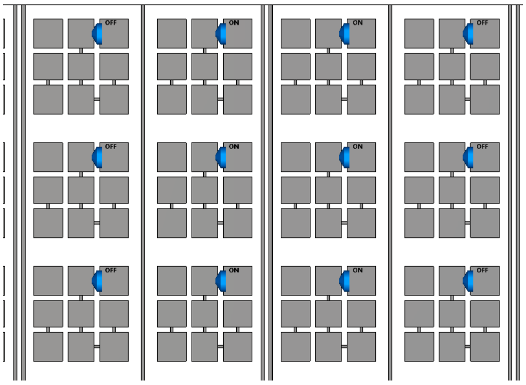

(c) Close up of the surface with a 1-bit active unit cell and a bias line

Figure 3.32: Surface with a 1-bit active unit cell and a bias line and its RCS results

3.5 Array Synthesis

For 1-bit beam steering, the classical technique of adjusting the phase of the elements, as discussed in earlier sections, results in a decrease in the capabilities of the RIS. This method involves calculating the required continuous phase distribution and discretizing the resultant phase values. However, this approach negatively impacts the performance of the RIS, particularly its SLL for beam steering applications.

To overcome this challenge, optimization tools can be employed to determine more optimal discrete phase distributions, thereby enhancing the performance of RIS with 1-bit elements [50], [51]. Rather than simply discretizing the continuous phase values, optimization algorithms can systematically explore different combinations of discrete phases to identify the configurations that best meet the desired performance criteria. These optimization tools can evaluate various phase configurations to minimize side lobe levels, maximize beamforming accuracy, and achieve other specific design goals. By utilizing this approach, the limitations associated with 1-bit beam steering can be mitigated, allowing the RIS to maintain high performance even with reduced bit resolution. For the optimization algorithm, we chose the genetic algorithm (GA). GA optimizers are robust, stochastic search methods modeled on the concepts of natural selection and evolution [52]. In the literature, it is shown that GAs are suitable for optimizing a broad class of electromagnetic problems, such as the reduction of array side lobes, the design of shaped-beam antenna arrays, and beam scattering applications [48], [52], [53].The genetic algorithm operates by iteratively evolving a population of candidate solutions towards an optimal configuration. This process involves selection, crossover, and mutation operations that mimic biological evolution. By using GA, we can effectively search the solution space for the best discrete phase distributions that meet our performance criteria for 1-bit RIS designs.

The genetic algorithm function in MATLAB is utilized, and the flow chart of the GA process is illustrated in Figure 3.33. In our application, the population size is set to 50. The initial population is the phase distribution of the surface where all the elements are set to 0 degree phase. In the analysis step, the array factor is calculated for each population member. Based on this array factor, the fitness values are evaluated according to performance criteria such as SLL, main lobe direction, and directivity. These fitness values represent how effectively each population member satisfies the specified criteria. The significance of these aspects will be discussed in detail in this section. The algorithm then proceeds to check if the stop criteria have been met. These criteria, defined by the user, are typically based on specific requirements such as achieving a certain SLL value, main lobe direction, or a combination of both.

One of the most important aspects of the genetic algorithm is the stop criteria, which determine whether the algorithm should continue or terminate. When establishing these criteria, it is essential to set the maximum runtime and adjust the maximum

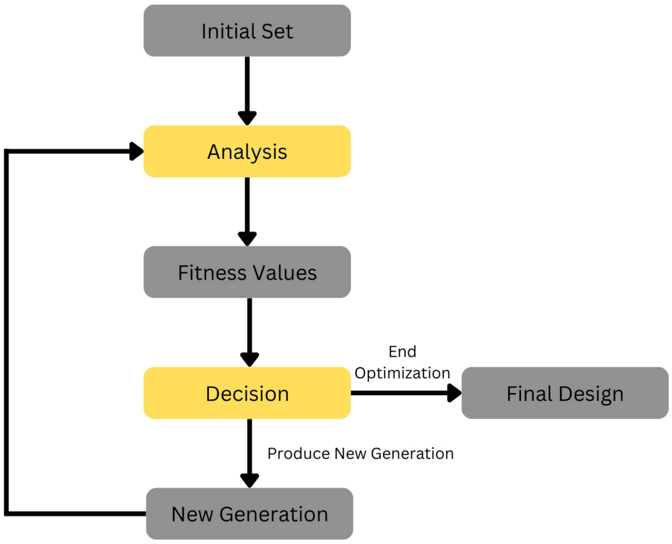

Figure 3.33: The flowchart of the genetic algorithm [54]

generation number to prevent the algorithm from running indefinitely. After defining these general limits, specific performance criteria, such as SLL and main lobe direction, should be established. These performance criteria guide the algorithm in optimizing the phase distribution. To convert these desired criteria into a form that a computer can process, a cost function must be defined. The cost function takes SLL, main lobe direction, and other results from the array factor calculations as inputs and outputs a fitness value. The fitness value indicates how closely a population member achieves the required performance.

To illustrate the GA in practice, an example is provided. In Figure 3.34, the initial phase distribution for a 1-bit 6×6 surface designed to steer the beam to 30 degrees is shown. The corresponding array factor for this distribution is also shown. As indicated, the SLL is initially at 0 dB due to the 1-bit discretization. To enhance performance, GA was employed to reduce the SLL. The cost function for the GA incorporates two critical performance metrics: the main lobe direction and the SLL. Various methods can be used to compute the cost function, including geometric average, arithmetic average, polynomial functions, among others. In our application, the cost function as shown in Equation 3.8 is formulated by summing the weighted inputs, where each input is multiplied by a weight reflecting its importance. In the equation w_1 and w_2 represent the weights for the SLL value and the main lobe direction, respectively. θ and $\theta_{desired}$denote the calculated and desired main lobe directions in degree, while SLL and $SLL_{desired}$ correspond to the calculated and desired linear SLL values. If minimizing the SLL is more important, its corresponding weight should be increased, thereby amplifying its influence on the fitness value. This linear cost function method is sufficient for our application for more advanced requirements non-linear approaches can be used.

$$FitnessValue = w_1 * |\theta_{desired} - \theta| + w_2 * max((SLL_{desired} - SLL), 0) \tag{3.8}$$

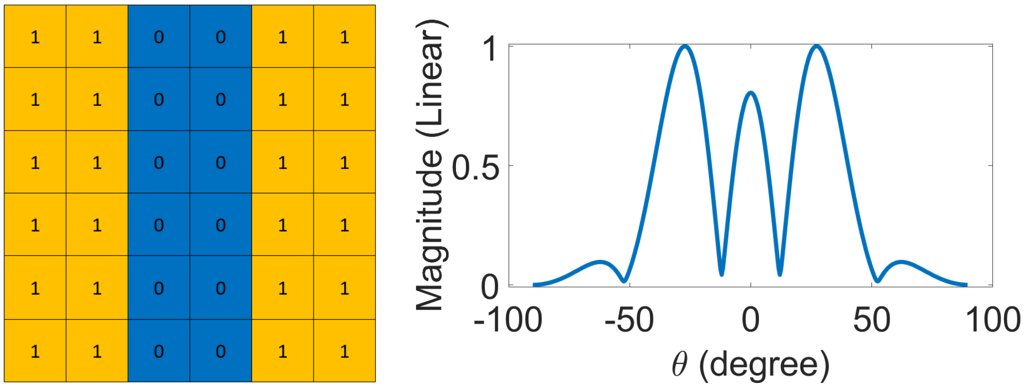

1	1	0	0	1	1
1	1	0	0	1	1
1	1	0	0	1	1
1	1	0	0	1	1
1	1	0	0	1	1
1	1	0	0	1	1

(a) Phase distribution to steer the beam to 30 degree

(b) Array factor of the phase distribution

Figure 3.34: Phase distribution and the array factor of non-optimized phase distribution

In Figure 3.35 the final phase distribution of the surface after the optimization and the resultant array factor are shown. The phase distribution of the surface is not symmetrical anymore therefore the lobe at symmetrical -30 degree is not as high as the previous distribution. In this design the highest side lobe is the one at the -30 degree therefore defeating the symmetry results in a better SLL performance. GA provide us to defeat this symmetry by preserving the main lobe direction at 30 degree. The SLL for non optimized surface is 0 dB i.e. at -30 degree the array factor is the same with the array factor at 30 degree. After the optimization the SLL is reduced up to 25 %.

This is a conceptual illustration demonstrating that optimization algorithms can enhance the performance of RIS. The phase distribution of a 1-bit RIS can be optimized more effectively using advanced techniques from the literature, and for larger RIS surfaces, even better results can be achieved [55], [56].

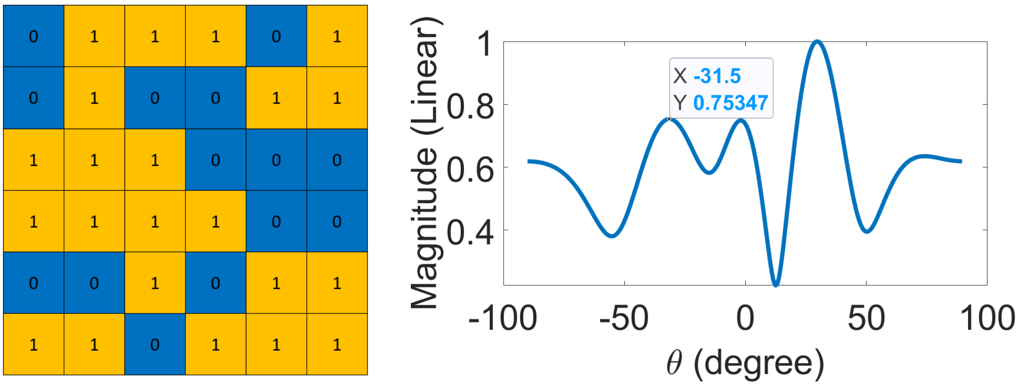

0	1	1	1	0	1
0	1	0	0	1	1
1	1	1	0	0	0
1	1	1	1	0	0
0	0	1	0	1	1
1	1	0	1	1	1

(a) Phase distribution to steer the beam to 30 degree

(b) Array factor of the phase distribution

Figure 3.35: Phase distribution and the array factor of optimized surface

3.6 Production and Measurement

After completing the simulations, three different passive RIS examples were manufactured to validate the design. One surface was designed to steer the beam to 30 degrees, demonstrating the beam-steering capability of the proposed RIS. Another surface was designed to absorb the incident wave, validating the RIS's absorption properties. Both of these surfaces comprised 7×7 unit cells. The third surface was designed to steer the beam to 20 degrees and utilized 2-bit unit cells. The manufacturing process was conducted at ASELSAN's facilities, utilizing Laser Direct Imaging (LDI) technology. The manufactured surfaces are shown in Figure 3.36. The surface on the right is designed to steer the beam to 30 degrees, while the surface on the left is designed to absorb the incident wave. The surface at the bottom is designed to steer the beam to 20 degrees using 2-bit frozen elements.

In the Microwave and Antenna Laboratory of the Department of Electrical and Electronic Engineering at Middle East Technical University, a setup was installed as shown in Figure 3.37 to measure the characteristics of the fabricated prototypes. The setup comprises two horn antennas capable of operating in the X-band. The first antenna remains stationary in front of the surfaces, while the second antenna is movable around the surface along an arc track. A protractor is utilized to measure the angle between the surface and the second antenna. Both horn antennas are connected to a network analyzer, facilitating the measurement of the S_{21} at various angle.

Using this setup, we measure the S_{21} parameter of three prototypes and a metal sheet that has the same dimensions with the surfaces to compare the results. First, we measured the 30 degree steering surface. The S_{21} results of the surface is shown in the figure 3.38a. The normalized simulation results were also given in the figure to compare the simulated and the measured results. As shown in the figure, the beam is successfully steered to 30 degrees using the surface, and the SLL is below -7.5 dB.

In Figure 3.38b S_{21} results of the surface at different frequencies are presented. These frequencies include the minimum (9.73 GHz), the maximum (10.50 GHz), and the operating frequency (10 GHz). At 10 GHz, the SLL is -7.5 dB, while at 9.73 GHz and 10.5 GHz, the SLLs are -4.5 dB and -5.2 dB, respectively. Therefore, the measured bandwidth is larger than predicted in the simulations. The predicted bandwidth was 3.5$\%$, whereas the measured bandwidth is 7.7$\%$.

Then, we measure the designed absorber and the metal sheet using this setup. The S_{21} results of both are presented in Figure 3.39a. The figure shows that absorbing surface absorbs the incident wave up to 24 dB. The maximum amount of absorption is at broadside but significant absorption is also observed at near angles. To confirm that the surface absorbs the wave rather than steering it to different angles, we used a plot that demonstrates the beam is not steered. Secondly, the difference between S_{21} values of the surface and the metal sheet at different frequencies for monostatic scenario is given in Figure 3.39b. If we use 3 dB difference between PEC and the prototype as a threshold for absorption, the surface can absorb the incident wave over a bandwidth of 2.5 $\%$ with a maximum absorption of 54 dB.

Finally, the frozen RIS that using 2-bit element is measured. In Figure 3.40b S_{21} results of the surface at different frequencies are presented. These frequencies include the minimum (9.8 GHz), the maximum (10.07 GHz), and the frequency at which the

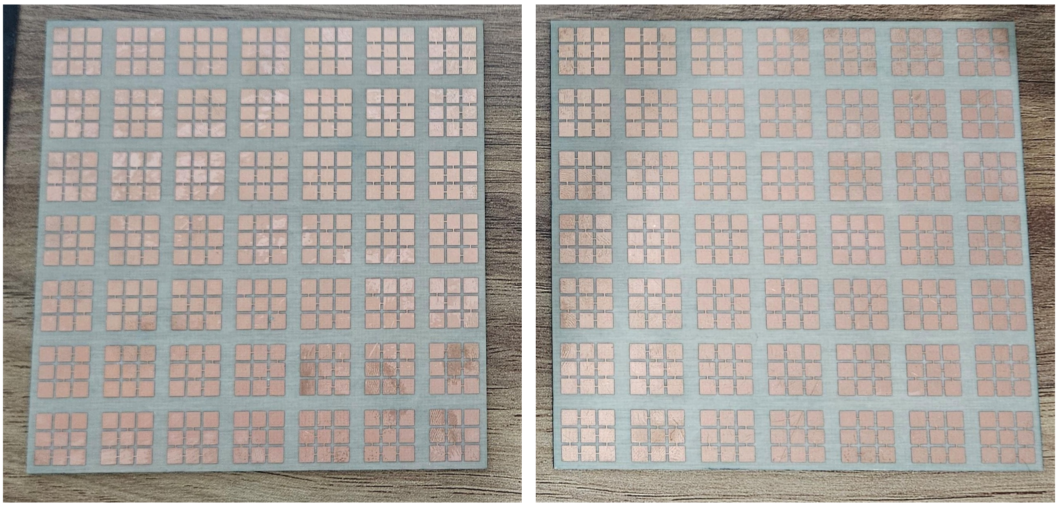

(a) A frozen RIS that absorbs the incident wave

(b) A frozen RIS that steers the incident wave to 30 degree

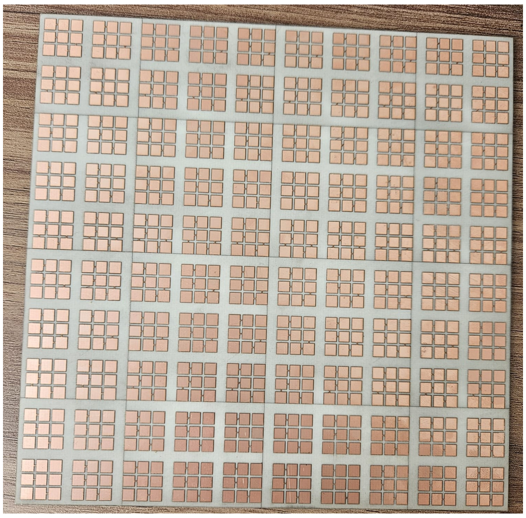

(c) A frozen 10x10 element RIS that steers the incident wave to 20 degree using 2-bit element

Figure 3.36: 3 Frozen RIS that manufactured in ASELSAN facilities

surface exhibits the best performance (9.9 GHz). At 9.9 GHz, the SLL is -5.9 dB, while at 9.8 GHz and 10.07 GHz, the SLLs are -6.8 dB and -3.2 dB, respectively. After the minimum frequency, the main lobe direction shifts to 15 degrees, and beyond the maximum frequency, the SLL decreases further to -2.7 dB. The S_{21} results of the surface are shown in Figure 3.40a, alongside the normalized simulation results for

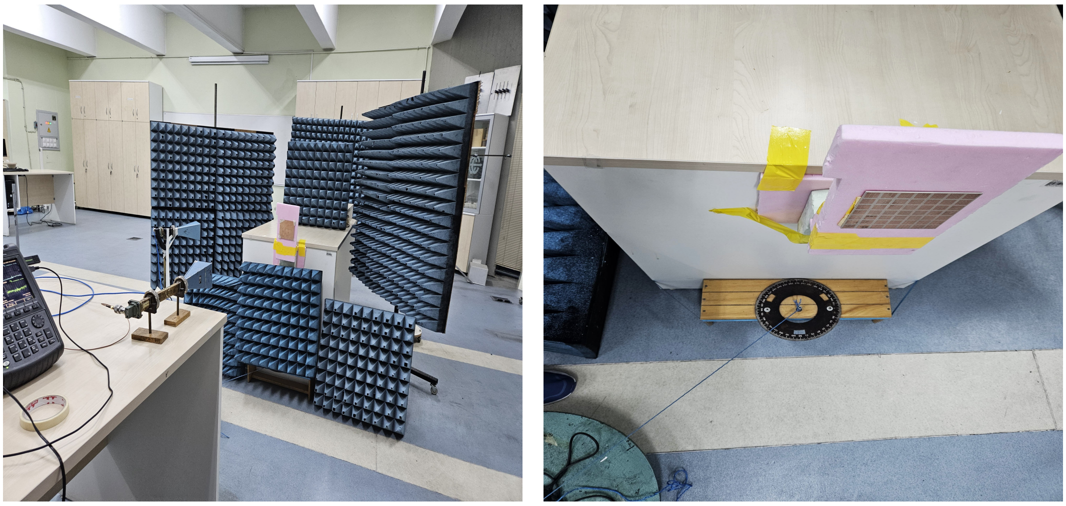

(a) Measurement setup

(b) Protractor

Figure 3.37: The measurement setup and protractor

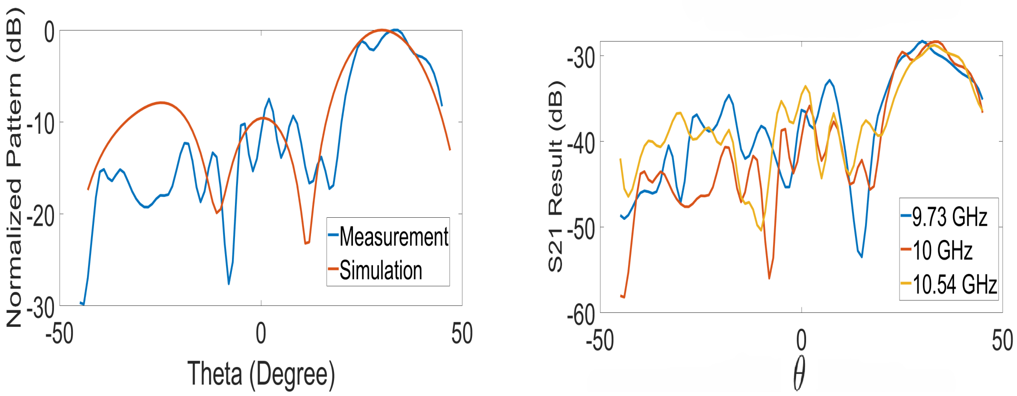

(a) Measurement and simulation result comparison of the frozen RIS that steers the beam to 30 degrees

(b) S_{21} plot at different frequencies of the frozen RIS that steers the beam to 30 degrees

Figure 3.38: Measurement results for the frozen RIS that steers the beam to 30 degrees

comparison. Although differences between the measured and simulated results are expected due to the lack of precision in the simulation setup, both indicate the main lobe at 20 degrees.

The signal enhancement of the steering surfaces was also measured using the setup.

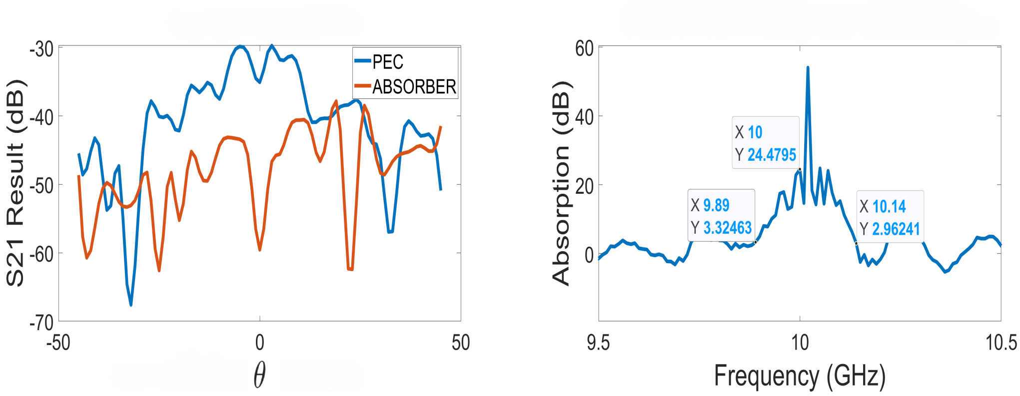

(a) S_{21} results for absorbing surface and a metal sheet with the same dimension

(b) Absorption at different frequencies

Figure 3.39: Measurement results for the absorbing surface

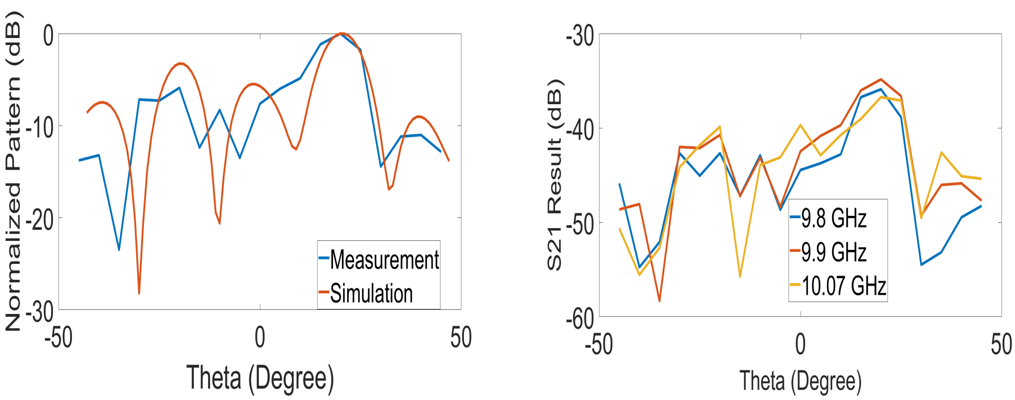

(a) Measurement and simulation result comparison of the frozen RIS that steers the beam to 20 degrees

(b) S_{21} plot at different frequencies of the frozen RIS that steers the beam to 20 degrees

Figure 3.40: Measurement results for the frozen RIS that steers the beam to 20 degrees

To calculate the S_{21} values, comparisons were made between the frozen RIS surfaces and PEC sheets of the same dimensions. The difference between these S_{21} values is referred to as signal enhancement. The results are shown in Table 3.8. The calculations indicate that the 30-degree surface enhances the signal by 16.9 dB, while the 20-degree surface provides a 13.8 dB enhancement. The superior performance of the 30-degree surface is expected, as it was designed using 12-bit elements.

Table 3.8: Signal Enhancement of the Beam Steering Surfaces

	S_{21} (PEC)	S_{21} (RIS)	Signal Enhancement
20° Steering Surface	-48.4 dB	-34.6 dB	13.8 dB
30° Steering Surface	-46.2 dB	-29.3 dB	16.9 dB

A second setup was installed to measure the manufactured prototypes. In this setup, a platform was used to place the prototypes, and a pole connected to the platform was used to place the horn antenna that illuminates the RIS surface in normal direction. Small horn with a large HPBW is preferred to have uniform illumination on our surface. The setup is shown in Figure 3.41. In this setup, the antenna was positioned at a height of 25 cm from the prototypes. The surface was measured similarly to reflectarray antennas. Given that the surface dimensions are $3.5\lambda \times 3.5\lambda$ and the antenna is placed at a distance of 8.3λ, the effect of the spatial delay on the surface is expected to be minimal. The prototypes were measured in the Anechoic Chamber of the Department of Electrical and Electronic Engineering at Middle East Technical University, with measurement results presented in Figure 3.42.

The measurement results for the beam steering prototype indicate that the main lobe deviates by 3-4 degrees from the desired 30-degree direction. This deviation is attributed to the antenna placement, which was done using bands, leading to potential variation in the incident angle. As discussed in Chapter 3.3.3, any deviation in the incident angle can alter the main lobe direction. The difference between the PEC and the absorber prototype is also shown in the figure. The results indicate that the prototype absorbs the incident wave up to 14 dB.

Figure 3.41: 2nd measurement setup and simulation result

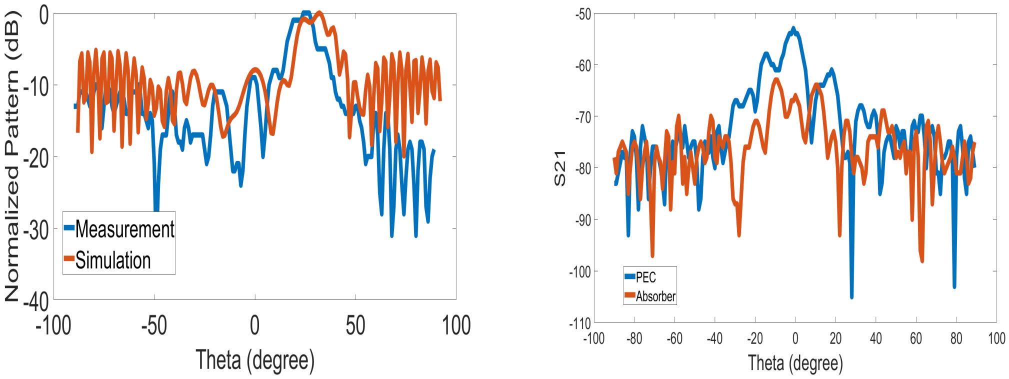

(a) The pattern measurement of the beam steering prototype

(b) The pattern measurement of the absorber prototype and a same size PEC surface

Figure 3.42: Measurement results of the second measurement setup

CHAPTER 4

CONCLUSION

RIS is a groundbreaking concept planned for use in 6G networks. RIS can manipulate the reflected EM wave by changing its electrical properties in real time. This feature allows it to change the reflection direction, focus the beam in the nearfield, and absorb the incoming wave. These properties would be highly beneficial for 6G applications, the main advantages are coverage extension, improving channel rank condition, and interference suppression.

A RIS consists of unit cells that determine the main aspects of its features. The proposed unit cell in this study is a 12-bit highly functional unit cell. The main advantage of this unit cell is its extensive range of phase, meaning it can realize most phases between -180 and 180 degrees. The high number of bits could be a problem since it increases the complexity and cost of the RIS; fortunately, the proposed unit cell can overcome this issue with a bit reduction technique introduced in this thesis. Other advantages of the unit cell are its lightweight and simple design. Additionally, some variations of the unit cell possess absorbing properties. This is a novel feature, as a RIS with the capability to absorb an incoming wave is not found in the literature. Generally, scattering of the incident wave is used to reduce the RCS of the reflected wave.

After introducing the unit cell, we showed that a multi functional RIS design can be achieved using the proposed unit cell. To design a multi functional RIS, it is crucial to be able to adjust the phase distribution of the surface in detail. Since the 12-bit unit cell has a very high phase resolution, it has a precise control over the phase distribution and it was shown that a RIS can be effectively designed using a 12-bit unit cell. The degradation of performance when using bit reduction techniques was also analyzed in this study. It was shown that while there is some degradation in performance, a RIS that operates robustly can still be designed using lower-bit variations of the unit cell. Active RIS simulations were also made to demonstrate that the RIS designed with the unit cell functions effectively when using the PIN diode. For the active RIS design, we tested the performance under different scenarios. Initially, we examined the effect of using PIN diodes instead of metal bridges, followed by an examination of the impact of bias lines. It is shown that bias lines do not introduce significant effect on the pattern.

In this study, the challenge of placing the bias lines is also addressed. Due to the narrow spacing between the unit cells, only 1-bit configurations up to a 6x6 size can be fabricated using a single layer. We propose three solutions to this issue: the first is to employ a multi-layer structure, the second involves using multiple 6x6 element surfaces, and the third is to implement column-by-column biasing. Given the complexity of multi-layer fabrication, we focused on row-by-row biasing and demonstrated that it functions effectively, with some degradation in capabilities. In summary, we have shown that a multi functional RIS can be realized using the designed unit cell. Additionally, to mitigate the limitations of the 1-bit active structure, we proposed the use of a genetic algorithm to adjust the state of the elements, demonstrating that this method improves the performance of the RIS.

Several of the designed RIS structures were fabricated and measured. The measurements confirmed that the fabricated RIS could steer the beam to 20 and 30 degrees as intended, thereby validating the design. Additionally, an absorbing surface was also manufactured and tested, demonstrating its ability to absorb the incoming wave within a 2.5% bandwidth.

In the future, a RIS incorporating PIN diodes will be fabricated. This prototype will be tested to ensure its effectiveness in beam steering and signal manipulation, validating its suitability for real-world applications.

REFERENCES

[1]E. Basar, M. Di Renzo, J. De Rosny, M. Debbah, M.-S. Alouini, and R. Zhang, "Wireless communications through reconfigurable intelligent surfaces", *IEEE Access*, vol. 7, pp. 116 753–116 773, 2019. DOI: `10.1109/ACCESS.2019.2935192`.

[2]Q. Wu, S. Zhang, B. Zheng, C. You, and R. Zhang, "Intelligent reflecting surface-aided wireless communications: A tutorial", *IEEE Transactions on Communications*, vol. 69, no. 5, pp. 3313–3351, 2021. DOI: `10.1109/TCOMM.2021.3051897`.

[3]Y. Liu, X. Liu, X. Mu, *et al.*, "Reconfigurable intelligent surfaces: Principles and opportunities", *IEEE Communications Surveys Tutorials*, vol. 23, no. 3, pp. 1546–1577, 2021. DOI: `10.1109/COMST.2021.3077737`.

[4]T Dhruvakumar and A. Chaturvedi, "Intelligent reflecting surface assisted millimeter wave communication for achievable rate and coverage enhancement", *Vehicular Communications*, vol. 33, p. 100 431, 2022, ISSN: 2214-2096. DOI: `https://doi.org/10.1016/j.vehcom.2021.100431`. [Online]. Available: `https://www.sciencedirect.com/science/article/pii/S2214209621001005`.

[5]Y. Zhao and X. Lv, "Network coexistence analysis of ris-assisted wireless communications", *IEEE Access*, vol. 10, pp. 63 442–63 454, 2022. DOI: `10.1109/ACCESS.2022.3183139`.

[6]D. Pozar, S. Targonski, and H. Syrigos, "Design of millimeter wave microstrip reflectarrays", *IEEE Transactions on Antennas and Propagation*, vol. 45, no. 2, pp. 287–296, 1997. DOI: `10.1109/8.560348`.

[7]E. Carrasco, J. A. Encinar, and Y Rahmat-Samii, "Reflectarray antennas: A review", in *Forum for Electromagnetic Research Methods and Application Technologies (FERMAT)*, vol. 16, 2016.

[8]J. Huang and J. A. Encinar, *Reflectarray antennas*. IEEE, 2007.

[9]D. R. Loopez and J. L. Roca, Ph.D. dissertation, Universitat Politecnica de Catalunya, 2014.

[10]E. Brown, "Rf-mems switches for reconfigurable integrated circuits", *IEEE Transactions on Microwave Theory and Techniques*, vol. 46, no. 11, pp. 1868–1880, 1998. DOI: `10.1109/22.734501`.

[11]R. Mishra, S. Pattnaik, and N. Das, "Tuning of microstrip antenna on ferrite substrate", *IEEE Transactions on Antennas and Propagation*, vol. 41, no. 2, pp. 230–233, 1993. DOI: `10.1109/8.214616`.

[12]D. Pozar and V. Sanchez, "Magnetic tuning of a microstrip antenna on a ferrite substrate", *Electronics Letters*, vol. 24, no. 12, p. 729, 1988. DOI: `10.1049/el:19880491`.

[13]S. Dash, C. Psomas, I. Krikidis, I. F. Akyildiz, and A. Pitsillides, "Active control of thz waves in wireless environments using graphene-based ris", *IEEE Transactions on Antennas and Propagation*, vol. 70, no. 10, pp. 8785–8797, 2022. DOI: `10.1109/TAP.2022.3142272`.

[14]Y. Qin, X. Y. Z. Xiong, W. E. I. Sha, and L. J. Jiang, "Electrically tunable polarizer based on graphene-loaded plasmonic cross antenna", *Journal of Physics: Condensed Matter*, vol. 30, no. 14, p. 144 007, 2018. DOI: `10.1088/1361-648X/aab227`. [Online]. Available: `https://dx.doi.org/10.1088/1361-648X/aab227`.

[15]N. Martin, P. Laurent, C. Person, P. Gelin, and F. Huret, "Patch antenna adjustable in frequency using liquid crystal", in *33rd European Microwave Conference Proceedings (IEEE Cat. No.03EX723C)*, vol. 2, 2003, 699–702 vol.2. DOI: `10.1109/EUMC.2003.177573`.

[16]N. Ehteshami and V. Sathi, "New optically controlled frequency-agile microstrip antenna", *Journal of Electronic Materials*, vol. 42, no. 1, 162–167, Oct. 2012. DOI: `10.1007/s11664-012-2273-5`.

[17]P. Nayeri, F. Yang, and A. Z. Elsherbeni, *Reflectarray antennas: Theory, designs, and applications*. John Wiley Sons, Inc., 2018.

[18]P. Yang, Y. Xiao, M. Xiao, and S. Li, "6g wireless communications: Vision and potential techniques", *IEEE Network*, vol. 33, no. 4, pp. 70–75, 2019. DOI: `10.1109/MNET.2019.1800418`.

[19]D. Dardari and N. Decarli, “Holographic communication using intelligent surfaces”, *IEEE Communications Magazine*, vol. 59, no. 6, pp. 35–41, 2021. DOI: `10.1109/MCOM.001.2001156`.

[20]A. Araghi, M. Khalily, M. Safaei, *et al.*, “Reconfigurable intelligent surface (ris) in the sub-6 ghz band: Design, implementation, and real-world demonstration”, *IEEE Access*, vol. 10, pp. 2646–2655, 2022. DOI: `10.1109/ACCESS.2022.3140278`.

[21]J.-B. Gros, L. Santamaria, V. Popov, *et al.*, “Design of reconfigurable intelligent surfaces at mmwave with application to 5g/6g”, in *2023 17th European Conference on Antennas and Propagation (EuCAP)*, 2023, pp. 1–4. DOI: `10.23919/EuCAP57121.2023.10133769`.

[22]R. Wang, Y. Yang, B. Makki, and A. Shamim, “A wideband reconfigurable intelligent surface for 5g millimeter-wave applications”, *IEEE Transactions on Antennas and Propagation*, vol. 72, no. 3, pp. 2399–2410, 2024. DOI: `10.1109/TAP.2024.3352828`.

[23]J. Rains, J. ur Rehman Kazim, A. Tukmanov, *et al.*, “High-resolution programmable scattering for wireless coverage enhancement: An indoor field trial campaign”, *IEEE Transactions on Antennas and Propagation*, vol. 71, no. 1, pp. 518–530, 2023. DOI: `10.1109/TAP.2022.3216555`.

[24]A. Pitilakis, O. Tsilipakos, F. Liu, *et al.*, “A multi-functional reconfigurable metasurface: Electromagnetic design accounting for fabrication aspects”, *IEEE Transactions on Antennas and Propagation*, vol. 69, no. 3, pp. 1440–1454, 2021. DOI: `10.1109/TAP.2020.3016479`.

[25]P. Mei, Y. Cai, K. Zhao, *et al.*, “On the study of reconfigurable intelligent surfaces in the near-field region”, *IEEE Transactions on Antennas and Propagation*, vol. 70, no. 10, pp. 8718–8728, 2022. DOI: `10.1109/TAP.2022.3147533`.

[26]E. Björnson, L. Sanguinetti, H. Wymeersch, J. Hoydis, and T. L. Marzetta, “Massive mimo is a reality—what is next?: Five promising research directions for antenna arrays”, *Digital Signal Processing*, vol. 94, pp. 3–20, 2019, Special Issue on Source Localization in Massive MIMO, ISSN: 1051-2004. DOI: `https://doi.org/10.1016/j.dsp.2019.06.007`. [Online]. Available: `https://www.sciencedirect.com/science/article/pii/S1051200419300776`.

[27]L. Shao, W. Zhu, M. Y. Leonov, and I. D. Rukhlenko, “Dielectric 2-bit coding metasurface for electromagnetic wave manipulation”, *Journal of Applied Physics*, vol. 125, no. 20, p. 203 101, May 2019, ISSN: 0021-8979. DOI: `10.1063/1.5094561`. eprint: `https://pubs.aip.org/aip/jap/article-pdf/doi/10.1063/1.5094561/19786407/203101\_1\_online.pdf`. [Online]. Available: `https://doi.org/10.1063/1.5094561`.

[28]H. Zhang, B. Di, L. Song, and Z. Han, “Reconfigurable intelligent surfaces assisted communications with limited phase shifts: How many phase shifts are enough?”, *IEEE Transactions on Vehicular Technology*, vol. 69, no. 4, pp. 4498–4502, 2020. DOI: `10.1109/TVT.2020.2973073`.

[29]B. Di, H. Zhang, L. Song, Y. Li, Z. Han, and H. V. Poor, “Hybrid beamforming for reconfigurable intelligent surface based multi-user communications: Achievable rates with limited discrete phase shifts”, *IEEE Journal on Selected Areas in Communications*, vol. 38, no. 8, pp. 1809–1822, 2020. DOI: `10.1109/JSAC.2020.3000813`.

[30]Q. Wu and R. Zhang, “Beamforming optimization for wireless network aided by intelligent reflecting surface with discrete phase shifts”, *IEEE Transactions on Communications*, vol. 68, no. 3, pp. 1838–1851, 2020. DOI: `10.1109/TCOMM.2019.2958916`.

[31]S. Dey and M. A. Shukoor, “Implementation of 3-bit reconfigurable intelligent surface (ris) for sub-6 ghz range based on modified square loop fss and tunable varactors”, in *2022 IEEE Microwaves, Antennas, and Propagation Conference (MAPCON)*, 2022, pp. 973–977. DOI: `10.1109/MAPCON56011.2022.10047303`.

[32]X. Pei, H. Yin, L. Tan, *et al.*, “Ris-aided wireless communications: Prototyping, adaptive beamforming, and indoor/outdoor field trials”, *IEEE Transactions on Communications*, vol. 69, no. 12, pp. 8627–8640, 2021. DOI: `10.1109/TCOMM.2021.3116151`.

[33]B. J. Xiang, X. Dai, and K.-M. Luk, “A wideband low-cost reconfigurable reflectarray antenna with 1-bit resolution”, *IEEE Transactions on Antennas and Propagation*, vol. 70, no. 9, pp. 7439–7447, 2022. DOI: `10.1109/TAP.2022.3176868`.

[34]J. A. Hodge, T. G. Spence, and A. I. Zaghloul, “A reconfigurable intelligent surface using a 2-bit programmable metasurface for communications”, in *2021 IEEE International Symposium on Antennas and Propagation and USNC-URSI Radio Science Meeting (APS/URSI)*, 2021, pp. 97–98. DOI: `10.1109/APS/URSI47566.2021.9703874`.

[35]D. Rodrigo, J. Romeu, B. A. Cetiner, and L. Jofre, “Pixel reconfigurable antennas: Towards low-complexity full reconfiguration”, in *2016 10th European Conference on Antennas and Propagation (EuCAP)*, 2016, pp. 1–5. DOI: `10.1109/EuCAP.2016.7481208`.

[36]Dec. 2016. [Online]. Available: `https://www.digikey.com/en/articles/how-and-why-to-use-pin-diodes-for-rf-switching`.

[37]R. J. Chitra and V. Nagarajan, “Frequency reconfigurable antenna using pin diodes”, *2014 Twentieth National Conference on Communications (NCC)*, Feb. 2014. DOI: `10.1109/ncc.2014.6811318`. [Online]. Available: `http://dx.doi.org/10.1109/ncc.2014.6811318`.

[38]S. Gharbieh, R. D. Errico, and A. Clemente, “Reconfigurable intelligent surface design using PIN diodes via rotation technique -Proof of concept”, in *EuCAP 2023 - 17th European Conference on Antennas and Propagation*, Florence, Italy, Mar. 2023. [Online]. Available: `https://cea.hal.science/cea-04006363`.

[39]R. Liu, J. Dou, P. Li, J. Wu, and Y. Cui, “Simulation and field trial results of reconfigurable intelligent surfaces in 5g networks”, *IEEE Access*, vol. 10, 122786–122795, 2022. DOI: `10.1109/access.2022.3223447`. [Online]. Available: `http://dx.doi.org/10.1109/access.2022.3223447`.

[40]R. E. Collin, *Antennas and Radiowave Propagation*. McGraw-Hill Companies, Jan. 1985. [Online]. Available: `http://books.google.ie/books?id=pgJTAAAAMAAJ&q=collin+antenna&dq=collin+antenna&hl=&cd=2&source=gbs_api`.

[41]C. A. Balanis, *Antenna Theory*. John Wiley Sons, 2016. [Online]. Available: `http://books.google.ie/books?id=iFEBCgAAQBAJ&printsec=frontcover&dq=balanis+antenna&hl=&cd=3&source=gbs_api`.

[42]Y. Albagory and F. Alraddady, “Optimum extrapolation techniques for two-dimensional antenna array tapered beamforming”, *Electronics*, vol. 11, no. 13, p. 1995, 2022.

DOI: `10.3390/electronics11131995`. [Online]. Available: `http://dx.doi.org/10.3390/electronics11131995`.

[43]OpenStax, *4.2 the law of reflection*. [Online]. Available: `https://pressbooks.bccampus.ca/introductorygeneralphysics2phys1207opticsfirst/chapter/25-2-the-law-of-reflection/`.

[44]M. Salah, I. H. Abdelaziem, and A. Pitsillides, "Phy0 network: Metasurface as phy-beam router, is it possible? challenges and open problems", *ITU Journal on Future and Evolving Technologies*, vol. 4, pp. 116–135, Mar. 2023. DOI: `10.52953/DFFJ2779`.

[45]A. Verma and O. Meena, "A review of metamaterial absorber and its absorption techniques", in *2023 IEEE International Students' Conference on Electrical, Electronics and Computer Science (SCEECS)*, 2023, pp. 1–6. DOI: `10.1109/SCEECS57921.2023.10062996`.

[46]F. Costa, A. Monorchio, and G. Manara, "Analysis and design of ultra thin electromagnetic absorbers comprising resistively loaded high impedance surfaces", *IEEE Transactions on Antennas and Propagation*, vol. 58, no. 5, pp. 1551–1558, 2010. DOI: `10.1109/TAP.2010.2044329`.

[47]W. Chen, C. A. Balanis, and C. R. Birtcher, "Checkerboard ebg surfaces for wideband radar cross section reduction", *IEEE Transactions on Antennas and Propagation*, vol. 63, no. 6, pp. 2636–2645, 2015. DOI: `10.1109/TAP.2015.2414440`.

[48]X. F. YASIR Saifullah YANG Guomin, "A four-leaf clover-shaped coding metasurface for ultra-wideband diffusion-like scattering", *Journal of Radars*, vol. 10, no. R21061, p. 382, 2021, ISSN: 2095-283X. DOI: `10.12000/JR21061`. [Online]. Available: `https://radars.ac.cn/en/article/doi/10.12000/JR21061`.

[49]F. Wang and A. L. Swindlehurst, *Applications of absorptive reconfigurable intelligent surfaces in interference mitigation and physical layer security*, 2023. arXiv: `2302.01508 [cs.IT]`.

[50]T. Valera, S. B. Venkatakrishnan, A. Madanayake, and J. L. Volakis, "Reconfigurable intelligent surfaces for adaptive nulling and beam steering using 1-bit topology", in *2023 United States National Committee of URSI National Radio*

Science Meeting (USNC-URSI NRSM), 2023, pp. 254–255. DOI: `10.23919/USNC-URSINRSM57470.2023.10043160`.

[51]A. Sheikholeslami and Z. Atlasbaf, "Novel phase distributions for large electronically beam-scanning reflectarrays", *Scientific Reports*, vol. 11, no. 1, Nov. 2021. DOI: `10.1038/s41598-021-00883-6`. [Online]. Available: `https://www.nature.com/articles/s41598-021-00883-6#citeas`.

[52]J. Johnson and V. Rahmat-Samii, "Genetic algorithms in engineering electromagnetics", *IEEE Antennas and Propagation Magazine*, vol. 39, no. 4, pp. 7–21, 1997. DOI: `10.1109/74.632992`.

[53]M. Srinivas and L. Patnaik, "Genetic algorithms: A survey", *Computer*, vol. 27, no. 6, pp. 17–26, 1994. DOI: `10.1109/2.294849`.

[54]G. Karaova, "Design, fabrication, and measurement of efficient beam-shaping reflectors for 5g mm-wave applications", M.S. thesis, Middle East Technical University, 2021.

[55]B. Goswami and D. Mandal, "A genetic algorithm for the level control of nulls and side lobes in linear antenna arrays", *Journal of King Saud University - Computer and Information Sciences*, vol. 25, no. 2, pp. 117–126, 2013, ISSN: 1319-1578. DOI: `https://doi.org/10.1016/j.jksuci.2012.06.001`. [Online]. Available: `https://www.sciencedirect.com/science/article/pii/S1319157812000328`.

[56]F. Soltankarimi, J. Nourinia, and C. Ghobadi, "Side lobe level optimization in phased array antennas using genetic algorithm", in *Eighth IEEE International Symposium on Spread Spectrum Techniques and Applications - Programme and Book of Abstracts (IEEE Cat. No.04TH8738)*, 2004, pp. 389–394. DOI: `10.1109/ISSSTA.2004.1371728`.